Physical Aspects of Radiation-Induced Processes on SiO_2, γ-Al_2O_3, Zeolites, and Clays

J. K. Thomas†

Department of Chemistry and Biochemistry, 251 Nieuwland Science Hall, University of Notre Dame, Notre Dame, Indiana 46556

Received April 1, 2004

Contents

1. Introduction 1684
2. Initial Thoughts and Concepts 1685
3. Experimental Techniques 1685
3.1. Spectroscopy 1685
3.2. Surface Area–Pore Size (BET) 1686
3.3. Sample Preparation 1686
3.4. Data Analysis 1686
4. Silica SiO_2 1687
4.1. Structures of Solid Supports 1687
4.2. Nature of the Surface Indicated by Photophysical Processes 1687
4.3. Fluorescence Spectroscopy of Pyrene and Its Derivatives 1687
4.4. Silanol Groupings 1687
4.5. Surface Studies with 1-Aminopyrene and 1-Pyrenecarboxylic Acid 1687
4.6. Heterogeneity of the SiO_2 Surface 1688
4.7. Charge Transfer Sites 1689
4.8. Quantum Yield of Fluorescence and Intersystem Crossing (Triplet) 1689
4.9. Quenching of Arene Excited States on SiO_2 1689
4.9.1. Quenching by Oxygen, Type a 1690
4.9.2. Quenching by Collision 1690
4.9.3. Quenching of Triplet States by O_2 1691
4.9.4. Formation of Singlet Oxygen 1692
4.10. Quenching Reactions on SiO_2 with Both Reactants Adsorbed 1692
4.10.1. Diffusion on a SiO_2 Surface, Type b 1692
4.10.2. 1-Pyrenebutyric Acid (PBA), Immobilized at the Surface 1692
4.10.3. Quenching by CCl_4 1693
4.10.4. Quenching of Excited Pyrene by *N*,*N*′-Dimethylaniline 1693
4.10.5. Quenching of Excited Pyrene by $C(NO_2)_4$ (TNM), Type c 1693
4.10.6. Reactions of Ions on SiO_2 Surfaces 1694
4.11. Trapped Electrons and Their Ensuing Reactions 1694
4.11.1. Photoionization with Light 1694
4.11.2. Nature of Trapped Electrons in SiO_2 1695
4.11.3. Ionization and Excitons on Radiolysis of SiO_2 1696
4.11.4. Radiolysis of SiO_2 1696
4.11.5. Electron Abstraction from SiO_2 by Photoexcitation 1696
4.12. Reactions at the SiO_2–Liquid Solvent Interface 1697
4.12.1. Surface Solvent Immobilization 1697
4.12.2. Reactions in Pores Containing Solvents, Category 1 1698
4.12.3. Oxygen Quenching 1698
4.12.4. Reactions at the Solid–Liquid Interface, Category 2 1698
4.12.5. Reactions with Surface-Adsorbed Quenchers, Category 3 1699
4.12.6. SiO_2–Polar Liquid Interface 1700
4.13. Interaction of SiO_2 Surfaces with Surfactants 1700
4.14. Ultrathin Polymer Coatings on SiO_2 Surfaces 1700
4.15. Geometry-Dependent Reactions on SiO_2 1700
4.16. SiO_2 as an Anchor for Other Oxides 1701
4.17. Summary 1701
5. γ-Alumina 1701
5.1. Nature of the Surface 1702
5.2. Charge Transfer Sites 1703
5.3. Spectroscopy of Probe Molecules on a γ-Al_2O_3 Surface 1703
5.3.1. Charge Transfer Sites and Mulliken Theory 1703
5.3.2. Aminopyrene as a Surface Probe 1703
5.3.3. Pyrenecarboxaldehyde as a Surface Probe 1704
5.3.4. Pyrene 1705
5.3.5. Summary of Different Sites on Activated Al_2O_3 1705
5.4. Quenching Reactions of Excited Arenes on γ-Al_2O_3 1705
5.4.1. Oxygen Quenching at the Solid–Gas Surfaces 1706
5.4.2. Quenching of Excited Pyrene by Co-adsorbed CH_3NO_2 and Nitrobenzene 1707
5.5. Surface Trapping of Electrons 1707
5.5.1. Spectroscopy of Trapped Electrons e_t^- 1708
5.5.2. Kinetics of e_t^- Decay 1708
5.6. Hydrogen Atoms Formed in Radiolysis 1709
5.7. Summary of Radiolysis of γ-Al_2O_3 1709
5.8. Final Products of Excitation of Arenes on γ-Al_2O_3 1709
5.8.1. Initial Formation of Radical Cations 1709
5.8.2. Reactions of Radical Cations 1709
5.9. Summary 1711
6. Zeolites 1711
6.1. Structure 1711
6.2. Adsorption and Adsorpton Sites 1712
6.2.1. Metal Ions 1712

† Telephone (574) 631-7589; fax (574) 631-6652; e-mail Thomas.3@nd.edu.

10.1021/cr020378a CCC: $53.50
Published on Web 04/26/2005

6.2.2. Neutral Organic Molecules 1712
6.3. Sample Preparation 1712
6.4. Nature of Absorption Sites 1713
6.5. Nature of Zeolite Supercage Surface 1713
6.6. Surface Properties 1713
6.7. Diffusion 1714
6.8. Mobility in the Supercage 1715
6.9. Quenching of Arene Fluorescence by Mobile Reactants 1716
6.10. Lifetime Measurements 1716
6.10.1. O_2 Quenching 1716
6.10.2. Dimethylaniline 1717
6.10.3. Immobile Quenchers, Cu^{2+}, Tl^{+}, etc. 1717
6.10.4. Diffusion and Rapid Quenching 1717
6.10.5. Rapid Reactions in Supercages 1718
6.11. Electron Transfer in, from, and to Zeolites 1719
6.12. Radiolytic Events in Zeolites 1719
6.12.1. Radiolysis 1720
6.12.2. Reactions of Alkali Metal Trapped Electrons 1721
6.12.3. Reactions of e^{-} with Metal Cations 1721
6.12.4. Trapping of e^{-} by Water Clusters 1722
6.13. Cation Formation 1722
6.13.1. Electron Extraction from Zeolites 1722
6.14. Pore Restriction of Reactions 1723
6.15. Aromatic Ketones in Zeolites 1724
6.15.1. Effects of Acidic Centers 1724
6.15.2. Photooxidation of Alkenes in Zeolites 1724
6.15.3. Asymmetric Photoreactions within Zeolites 1724
6.16. Channel Zeolites 1725
6.17. Directed Energy Transfer 1725
6.18. Further Selected Examples 1725
6.19. Luminescence of Inorganic Molecules in Zeolites 1725
6.20. Summary 1727
7. Photochemistry on Clay Systems 1727
7.1. Structures of Clay 1727
7.2. Colloidal Clay 1728
7.3. Surface Configuration of Adsorbed Molecules 1728
7.4. Degree of Dispersity of Colloidal Clay 1729
7.5. Pillared Clay 1729
7.6. Dry Clays 1729
7.7. Summary 1730
8. Symbols 1731
9. Acknowledgment 1731
10. References 1731

John Kerry Thomas was born in Wales in 1934. He attended the University of Manchester in England from 1951 to 1957, when he obtained a B.Sc. degree in 1954 and a Ph.D. in 1957. His graduate work on the photo- and X-ray degradation of polymers was supervised by Dr. J. H. Baxendale, a notable kineticist. From 1957 to 1958 he was a postdoctoral fellow at the National Research Council in Ottawa, Canada. He returned to Harwell, England, as a Scientific Officer in 1958, where he carried out work on radiation-induced surface graft polymerization. In 1960 he joined the Argonne National Laboratory in Illinois, where he remained until 1970. It was there that he developed the short-pulsed nanosecond laser and pulse radiolysis techniques, which are so popular in physical chemistry today. With these techniques he studied the fundamental chemical processes induced by radiation. In 1970 he went to the University of Notre Dame as a professor of chemistry. In 1969 he was awarded an honorary Doctor of Science by the University of Manchester; in 1974 he was given the research award of the Radiation Research Society; and he was a Gäst Professor at the Hahn Meitner Institute in Berlin in 1975. He was appointed Julius A. Nieuwland C.S.C. Professor of Chemistry in 1984. He has been the recipient of the Award in Colloid or Surface Chemistry sponsored by the Procter and Gamble Co. in 1993. He is the author of over three hundred research papers and review articles and an ACS Monograph 181, "*Chemistry of Excitation at Interfaces*". This text describes in some detail Dr. Thomas's application of pulsed photochemical methods to investigate reactions at interfaces as well as the nature of the interfaces themselves. Dr. Thomas has established many of the original concepts used in this fast growing field of reactions in organized or constrained media with its many applications to storage of energy, biokinetics, and catalysis. He is a member of the American Chemical Society, a Fellow of the Royal Society of Chemistry, the Photobiology Society, and the Society for Radiation Research, where has been a member of the council. He has served on the Editorial Board of the *Journal for Radiation Research* and presently serves on the Editorial Board of *Chemical Physics Letters*, *The Journal of Colloid and Interface Science*, and *The Journal of Physical Chemistry*. He has been a past Chairman of the Gordon Conference in Radiation Chemistry and of the Gordon Conference on Micelles and Macromolecular Catalysis. In 2005 he was installed a Fellow of the Inter American Photochemical Society. He annually gives many invited lectures both in the United States and abroad.

1. Introduction

There is a wealth of information on many aspects of the photophysics, photochemistry, and radiation chemistry of many molecular systems in solution, where events are now described from femtoseconds to ambient time, or stable products. For the most part the observed radiation-induced chemistry is determined by the properties of the system and is inviolate. However, the chemistry may be directed into areas of great utility via organized assemblies.

The aim of photochemists for over three decades[1−5] has been to mimic nature and design chemical systems that direct the photochemistry to useful ends. Numerous examples of exciting new concepts in chemistry have been developed, and this has contributed to the successful design of solar harvesting devices.[6] Further work is now underway in this arena of research. These studies of small particle or colloid photochemistry are now masquerading under the banner of nanochemistry. In early designs, advantage was taken of various micellar systems to promote the photochemistry of hydrophobic molecules in aqueous media. The interface of the microparticles was also used as a mode of separating charged products. Today the established field of colloid chemistry plays host to photochemistry, synthesis of nanoparticles, etc.[7] It was soon realized that the energetic chemistry produced on photolysis of organic systems led to damaging side effects on the compo-

nents of the system. This wasted much of the energy and minimized the chemistry produced by the light. To counteract these difficulties advantage has been taken of small inorganic colloids or porous inorganic systems. This review dwells on various aspects of several porous and small particle systems at high surface area such as SiO_2, Al_2O_3, zeolites, and clays that act as hosts. Some photochemical systems view the hosts as inert, whereas others are reactive with the porous system itself. Many of the systems, in particular, zeolites, contain centers of marked thermal catalysis, and these can be used to direct the photochemistry.

The chemical and physical concepts of photochemistry on solid inorganic surfaces are quite different from those utilized in other microheterogeneous systems, for example, micelles. The inorganic host systems are rigid, and organic molecules are adsorbed on their surfaces. Also, the hosts are normally in powdered form, and as they are opaque to the transmission of light, new optical methods are required. However, many concepts of the earlier work remain, for example, that of compartmentalization where back reaction is avoided as products are located in different porous areas of the host. For the most part, any adsorbed molecules are held rigidly to the solid surfaces, with minimal diffusion along the surfaces. In earlier studies, the wealth of classical work in micelle and colloid chemistry was a boon to the photochemists working in these systems. Classical studies in SiO_2 (Al_2O_3, clays, and zeolites), for example, surface area studies, degree of adsorption, or structure of the material, are again available and helpful to the photochemist and radiation chemist.

The overlap between photochemistry in micellar systems and that in high surface area inorganic systems is considerable. Probably the most important theme is that of the production of chemistry in confined spaces and at active centers, and the effect of these regions of space, in directing the outcome of the chemistry. The other edge to this approach is the commentary that the photochemistry makes on the host surface itself. In this aspect the photochemistry adds additional information to what is already known of the surface by conventional methods. In photochemistry, quanta of wavelength >266 nm (<5 eV) are used.

Due to its mode of energy loss (Compton scatter) and high energy quanta E > 300 kV, the utility of the radiolytic method is to uniquely produce ionization of the substrate, that is, SiO_2, γ-Al_2O_3, zeolite, or clay, thus producing positive holes, h^+, and electrons. The interaction of these species with solutes hosted on the surface produces radical ions. This avoids the complication of photochemistry, where excited singlet and triplet states and radicals are produced along with any radical ions.

2. Initial Thoughts and Concepts

This review covers the influence of the surfaces, SiO_2, γ-Al_2O_3, zeolites, and clays, on selected physical and chemical events on these surfaces. The studies reviewed either give new information of the microdetails of the surface or illustrate the effect of the surfaces on radiation-induced ionic reactions. For conciseness, much photo-organic chemistry mainly dealing with product analysis is not included. The importance of this latter work (which deals with geometric effects of zeolites on various photo-organic reactions) cannot be overstated, and attention is drawn to these studies where appropriate.

The components of the photo- or radiolytic system adsorb to the surfaces via surface OH groups, at various acidic sites, and at charge transfer (CT) sites. The radiation-induced chemistry at these sites is quite different from that obtained in conventional solvents. The two initial systems, SiO_2 and γ-Al_2O_3, adsorb molecules via surface OH groups, but following heat treatment γ-Al_2O_3 can also possess acidic sites. Various combinations of SiO_2 and γ-Al_2O_3 lead to zeolites and clay systems. These systems are crystalline and possess small pore channels or layers, which, unlike SiO_2 and γ-Al_2O_3, can constrict the motion of molecules adsorbed into them and, hence, modify certain reactions. It is pertinent to note that SiO_2 is amorphous, whereas the other systems are crystalline.

As the "normal" (solvent) behavior of the photosystem is well established, deviations from this behavior, when the system is adsorbed on a surface, can be used to survey the actual surface. A comparison of photodata on a surface with those obtained via conventional means can often enhance the picture of the surface. For example, both methods can identify surface-adsorbed sites, but the photomethods can also provide details of the distribution of these sites on the surface.

It is sometimes stated that "the molecule dissolves in the surface". This is not a good concept of the molecules adsorbed to the surface. One simple illustration is that a molecule dissolved in a solvent reorganizes the solvent in its vicinity. This certainly does not occur with a molecule adsorbed on a surface.

3. Experimental Techniques

All experimental techniques discussed in this review are published in detail elsewhere; only a brief outline of the methods is given to help the reader. Major experimental differences between work in opaque scattering solids and that in transparent systems are that (a) reflectance[8] or diffuse transmittance[9] spectroscopy has to be used, (b) the nature of the solid surface has to be known or ascertained from measurements of the surface area and surface coverage by the reactants; and (c) heterogeneous kinetics often provides a better description of the time-dependent data.

3.1. Spectroscopy

In solids, fluorescence or emission spectroscopy is very similar to that used in liquids for both pulsed excitation and steady state excitation. A front surface configuration is used.[10] However, absorption spectroscopy in solids uses diffuse reflectance or transmittance techniques, where the difference in the reflectance spectrum of the solid with and without added probe represents that of the sample. Reflec-

tance spectra are depicted with the Kubelka−Munk function

$$F(R) = (1 - R)^2/2R \quad (1)$$

which is used most often for describing the reflectance of scattering, opaque materials.[8,11−13] Spectra are measured using solid samples, including powders or pressed disks of the powders.

The diffuse reflectance laser flash photolysis data are often reported as $1 - R$, given by eq 2:

$$1 - R_t = (I_0 - I_t)/I_0 \quad (2)$$

I_0 is the initial reflected light before laser excitation, and I_t is the reflectance of the sample at time (t) following laser excitation. Wilkinson et al.[8,11,12] have used this function for time-resolved absorbance data and found $1 - R_t$ to be linear with the amount of transient present in powdered samples when $1 - R_t$ is <0.1. In diffuse transmittance, the simple Beer's law expression is used.

3.2. Surface Area–Pore Size (BET)

The surface area and pore sizes of the samples as powders are measured by the BET[14−16] method and are sometimes supplied by the manufacturer. In the laboratory a surface area analyzer such as a micrometric model ASAP 2400 can also be used with N_2 gas at 77 K. Such methods can be used to measure the adsorption of other gases and vapors, O_2, CCl_4, nitromethane, etc., and give an effective surface area occupied for these molecules.

3.3. Sample Preparation

Guest molecules, such as pyrene or anthracene, are adsorbed to the surfaces as powders or disks, from cyclohexane or hexane solutions. Ionic materials, for example, methylviologen, are adsorbed to surfaces from polar solvents, for example, water. Standard pretreatment conditions include drying silica and Si/Al catalysts at 150 °C in air for 18−24 h, drying zeolites at 500 °C for 3 h, and drying clays and γ-alumina at various temperatures. This is followed by cooling in a desiccator. Often disks of the material (0.1 mm thick) are prepared by pressing the powders at high pressures (up to 4 ton/in.^{2}) on a Carver press. A solution of the molecule to be adsorbed at the desired concentration in dry cyclohexane is added to the dry or preheated samples. Gentle stirring for 2 h is sufficient to reach maximum adsorption on the high surface area powder disk. The supernatant is checked spectroscopically before and after the 2 h period, the difference giving the adsorption of the material to the surface. Typically, a molecule such as pyrene is added to the 60 Å silica from cyclohexane to give a final surface concentration of 0.45 μmol/g. The solvent is removed by pumping under vacuum at 100 °C.

The residual water content of the powdered silica is estimated spectroscopically or gravimetrically using pressed disks. The surface OH stretching bands and the bands from the surface-adsorbed water are measured before and after the self-supporting disks are doped with a known amount of water. For example, the residual water content estimated from the infrared studies for SiO_2 heated at $T_a = 150$ °C sample is <1.0 μmol/g, and no detectable water is seen on a 600 °C sample that is heated for 24 h in air.

3.4. Data Analysis

Three kinetic models[18] are used to mathematically simulate the decay profiles of excited states of guest molecules on the surface. The first, which is normally applied to the majority of emission decays, *is the single-exponential* function given in eq 3. This is most commonly used to stimulate the decay of species by a single species, which experiences one environment.

$$I_t = I_0 \, e^{-kt} \quad (3)$$

This can be expanded to a *biexponential* function, given below in eq 4, where the decay profile is defined by two species, which are independent of each other, for example, a probe molecule that is partitioned between two different environments. This model has been used for solid−liquid interfaces where the species being studied is partitioned between the liquid and the surface.

$$I_t = I_0[A \exp(-k_1 t) + (1 - A) \exp(-k_2 t)] \quad (4)$$

k_1 and k_2 refer to the reaction rate constants of the species at two different sites of reaction, and A is the fraction of the species that reacts via site 1. The double-exponential fit is used to distinguish reactions in the pore volume compared to reactions in the bulk volume between the particles. This is estimated from the density of the powder and that of the fused material. For different pore sizes of 150, 60, and 40 Å, the ratios of pore volume to interparticle space are 44:56, 42:58, and 55:45, respectively. This means that A in eq 4 is 0.44, 0.42, and 0.55 and corresponds to reaction in the pore volume.

Finally, a *Gaussian distribution* in the natural logarithm of observed rate constants can be used to handle heterogeneous media where a species is expected to have a distribution of environments. The heterogeneous interaction of a system with an adsorbate can be approximated by a Gaussian distribution,[19] whereas the distribution in rate constants can be characterized through a mean rate constant, $\bar{k}$, and a distribution parameter, γ. The distribution in the first-order decay rates can be written as in eq 5. Integration over the distribution, $\exp(-x^2)$, yields eq 6; this is solved for and used to simulate the experimental decay profiles.[20]

$$k = \bar{k} \exp(\gamma x) \quad (5)$$

$$\frac{I(t)}{I(0)} = \frac{\int_{-\infty}^{\infty} \exp(-x^2) \exp[-\bar{k}t \exp(\gamma x)] \, dx}{\int_{-\infty}^{\infty} \exp(-x^2) \, dx} \quad (6)$$

Other approaches[21−24] have considered the fractal nature of the solid surface; however, these treatments do not give rate constants as in the treatment given

above, but assign an appropriate fractal dimension to the surface.

4. Silica SiO_2

4.1. Structures of Solid Supports

The silica used is of two common forms, an aerosil or fumed silica, which consists of small ($r \sim 100-1000$ Å), nonporous particles and has a surface area of $500-50\ m^2\ g^{-1}$, or a silica gel, which has large ($r > 5\ \mu m$) porous particles, with surface areas in the $300\ m^2\ g^{-1}$ range. The latter high surface area silica gel has an amorphous structure, with average pore radii of the silica gels as small as 20 Å and as large as 150 Å. Figure 1 pictorially represents the formation

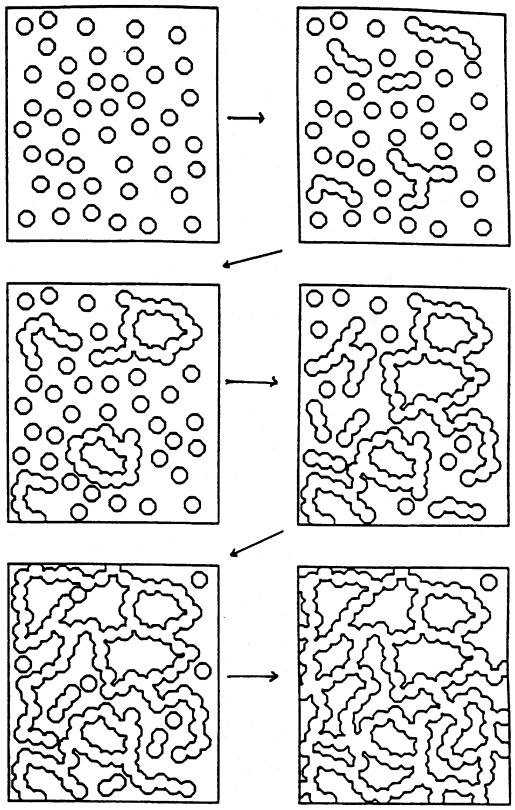

Figure 1. Pictorial representation of the formation of porous silica from small SiO_2 particles.

of these systems from precipitated silicates. The surfaces of both types of silica contain silanol OH groups, which can be 5 OH/nm^{-2} for SiO_2 heated to 120 °C and 1 OH group/nm^2 for silica heated to 500–600 °C. Heating silica removes H_2O, and at very high temperatures (>600 °C) this leads to the formation of siloxane bridges, the OH/nm^{-2} dropping to unity.[17] It has been established that high surface area SiO_2 can catalyze several different types of organic reactions, and some of the more recent studies are given in refs 25–31. The influence of SiO_2 on thermal reactions is quite marked, and similar effects are expected on photochemical reactions.

4.2. Nature of the Surface Indicated by Photophysical Processes

The photophysics of an arene adsorbed at the SiO_2 on the $SiO_2-C_6H_{12}$ interface is characteristic of that in a polar and rigid environment.[32–34] The rigidity of the surface environment is indicated by the much slower *cis–trans* isomerization of dyes on the SiO_2 surface compared to solution.[34] This will also become apparent later on when reactions on the surface are considered.

4.3. Fluorescence Spectroscopy of Pyrene and Its Derivatives

Pyrene is a versatile molecule for surveying environments. In polar solvents the 370 nm peak (I) is much larger than that of the third peak at 390 nm (peak III). The opposite is true in nonpolar media. The peak ratio III/I can be used to estimate the polarity of the pyrene microenvironment at the silica surface.[35] Such studies show that the probe experiences a polar environment that remains polar even in contact with bulk C_6H_{12}. At low loading (up to 10^{-6} mol/g) only pyrene monomer fluorescence is observed. Increasing the loading to $>10^{-6}$ mol/g leads to pyrene excimer emission.[36–40] An activation spectrum, using emission of the spectrally absorbing species giving rise to the excimer, shows that a ground state complex of pyrene leads to the excimer, although there is some indication of a kinetic formation of the excimer via ground and excited state pyrene.[37–40]

The above studies illustrated the polar nature of the SiO_2 surface, a consequence of the adsorption of the arene probes to the surface silanol groups.

4.4. Silanol Groupings

Further studies of the surface with aminopyrene and pyrenecarboxylic acid[41–43] show that different SiO_2 preparations contain various amounts of vicinal and geminal OH groups.

4.5. Surface Studies with 1-Aminopyrene and 1-Pyrenecarboxylic Acid

Both 1-aminopyrene (1-AP) and 1-pyrenecarboxylic acid (PCA) possess two chromophores, which interact in the excited state, the extent of the interaction depending on the medium. The lone pair of the amine chromophore of 1-AP acts as an internal switch, which operates the 1-AP's photophysics. The photophysical behavior of 1-AP is dominated by protonation, which blocks the lone pair (Figure 2). The

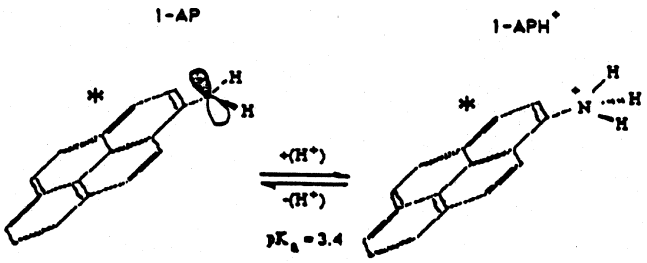

Figure 2. Diagram of protonation of aminopyrene.

protonation of the amino group leads to a complex 1-APH^+ with photophysical properties similar to those of pyrene. The free 1-AP system exhibits quite different photophysics relative to that of pyrene. In other studies,[43] the photophysical properties of PCA

have been correlated to its acid/base properties, and again fluorescence that depends on the medium is observed. Using this behavior, 1-AP and PCA have been used to distinguish the relative populations of geminal and vicinal silanol functionality at the silica gel surface and give quantitative measurements of these two species on the surface.

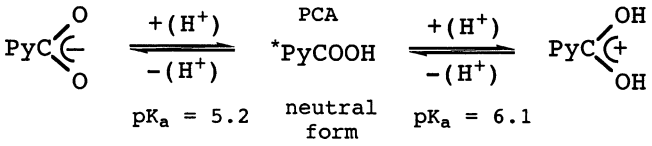

Figure 3 shows the fluorescence spectra of 1-AP adsorbed on Matheson, Coleman, Bell (MCB) and

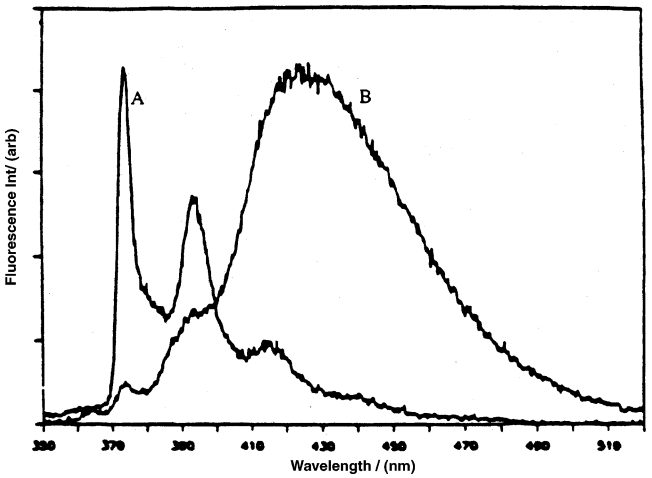

Figure 3. Fluorescence spectra of 1.9×10^{-7} mol/g 1-AP on (A) MCB and on (B) FS-662 silica gel, in deoxygenated cyclohexane, $\lambda_{ex} = 337$ nm. Reprinted with permission from ref 42. Copyright 1994 American Chemical Society.

Fischer Scientific (FS-662) silica gels in cyclohexane. It is seen that the fluorescence spectrum of 1-AP adsorbed on MCB is quite typical of 1-APH$^+$ curve A, whereas the fluorescence spectrum of 1-AP on FS-662 1-AP is curve B, typical of 1-AP itself. The excited 1-APH*, 1-APH$^+$*, decays with an inherent unimolecular lifetime of 135 $\pm$ 2 ns, whereas the 1-AP* decays with an inherent unimolecular lifetime of 4.9 $\pm$ 0.1 ns. Here the photophysical behavior of the 1-AP indicates that the adsorption sites for 1-AP are different on the two silica samples at the given probe loadings.

Moderate heat treatment of the MCB silica gel at 450 °C for 24 h, that is, below the sintering temperature, alters the surface such that the fluorescence spectrum of 1-AP adsorbed on this surface shows the character of both 1-AP and 1-APH$^+$. Heating MCB silica at 650 °C yielded a 1-AP spectrum identical to that of 1-AP adsorbed on FS-662. Conversely, treatment of the FS-662 silica gel with concentrated nitric acid for several hours, followed by washing with water until the wash maintained a neutral pH, alters the surface so that the fluorescence spectrum of 1-AP adsorbed on this surface resembles that obtained from the MCB silica surface. The thermal[44] and chemical[45−47] treatments of the silica gels alter the degree of clustering of the silanol functionality present on the silica surface, that is, the relative degree of geminal and vicinal silanol sites. Other studies with aniline/SiO_2 show[45] that the geminal silanol configuration gives rise to an adsorption site which yields a protonated form of aniline. A similar correlation would account for the observed photophysical behavior of 1-AP on the silica gel surfaces, that is, a protonated form at geminal sites (MCB silica), and the native form on vicinal sites (FS-662 silica).

PCA has been used[43] to probe the microacidity of the silanol functionality. The scheme shown earlier was established for the solution photophysics of PCA, and the observed fluorescence decay rate constant was found to be diagnostic for the determination of the apparent pH of the microenvironment. MCB-bound PCA demonstrated a neutral form, or a singly protonated carboxylic acid group fluorescence, whereas FS-662-bound PCA demonstrated a mixed anionic/neutral fluorescence. The observed fluorescence decay rate constants are 1.9×10^8 and 3.8×10^7 s^{-1} and correspond to apparent pH values of 1.6 and 4.1 for the microenvironments of the geminal and nongeminal silanols, respectively.

These data agree well with SiNMR data by Maciel.[48] It is unfortunate that the homogeneity of the silanol groups on the SiO_2 surface is unknown, as this situation controls the mobility and distribution of adsorbed molecules.

4.6. Heterogeneity of the SiO_2 Surface

The aminopyrene and pyrene carboxylic acid data show that several types of surface OH groups exist on SiO_2 and that organic molecules do not adsorb uniformly on this surface. Further evidence is provided by pyrene studies in which pyrene excimers form statically at low surface loadings, 10^{-6} mol g^{-1}, that is, well below a stage at which a uniform probe loading would indicate a significant probability that two pyrene molecules are adsorbed in sufficiently close proximity to give static excimers. Also, the decays of excited singlet states are not single exponential,[20−25,37−40,49,50] again indicating a nonuniform adsorption of the arenes on the SiO^{2-} surface.

Surface nonhomogeneity also appears when a fluorescing molecule and a quencher are co-adsorbed on SiO_2.[51] In the pyrene−ferrocene system, at ferrocene loadings of $<10^{-6}$ mol g^{-1}, an immediate drop in the yield of excited pyrene was observed at the end of the 0.2 ns laser excitation pulse, which is followed by a slow (10^{-7} s) quenching of the fluorescence. Similar data were seen with the perylene quenching of pyrene fluorescence. Heating the surface to 450 °C for 24 h, which reduces the silanol content, removed the initial rapid quenching, and more homogeneous kinetics were observed. The heating produces H_2O by reaction of adjacent silanol groups, and it is assumed that regions rich in silanol groups will react first. Hence, the surface should become more homogeneous as viewed by the adsorbed molecule.

These studies suggest that the SiO_2 surface is heterogeneous with respect to silanol groups, giving rise to a heterogeneous adsorption of organic molecules. This may be corrected by co-adsorption of polar additives such as alcohols. The polar additives

create an adsorbed surface layer, replace the arene from the silanol groups, and relocate them in a "uniform" less polar environment. This gives rise to simple fluorescence decays typical of the solution phase.

4.7. Charge Transfer Sites

The photophysics fluorescence spectra and lifetime together with quantum yields of pyrene, perylene, coronene, and several other polyaromatic adsorbates on silica gel and related oxide surfaces indicate the presence of charge transfer (CT) sites on the SiO_2 surface.[11,12,22−25,52−55] It is noted that the fluorescence and triplet quantum yields for the arenes are markedly lower on silica gel compared to those in simple solution.[55] This is related to the adsorption of the molecules on SiO_2 sites where CT complexes are formed.[55] The silica−arene CT complex is identified by its spectral absorption and emission, which is red-shifted with respect to pyrene, and by its shorter lifetime of 20 ns compared to that of >100 ns for pyrene. As the emission of the CT state is reduced by the addition of polar co-adsorbates such as nitromethane. it is suggested that the co-adsorbates adsorb strongly at the active CT surface sites and replace pyrene, which then adsorbs at nonactive sites. It was concluded that a low concentration ($<5 \times 10^{-8}$ mol g^{-1}) of CT sites is present on the surfaces of SiO_2. At a pyrene loading of 0.45 μmol g^{-1} of SiO_2, ~10% of the pyrene is adsorbed at these sites. The interaction of pyrene at these sites quenches the normal pyrene emission and gives rise to a short-lived CT emission. The absorption spectrum of the CT emission is red-shifted with regard to pyrene, and the emission shows a maximum at 420 nm. The exact nature of the CT sites is not known. Use of purified silica gel and doped silica rule out common impurities such as iron and aluminum, and it is suggested that the CT sites are native defects on the SiO_2 surface. Future studies are needed to address the characteristics of these CT sites. All of these studies, via the nature of the photochemistry, draw attention to the heterogeneous nature of the SiO_2 surface and the varied sites for adsorption of guest molecules.

4.8. Quantum Yield of Fluorescence and Intersystem Crossing (Triplet)

The quantum yields of fluorescence and intersystem crossing for several arenes on SiO_2 and in solution are shown in Tables 1 and 2. Due to adsorption at CT sites, the quantum yields on SiO_2 are lower than those in solution for both fluorescence and intersystem crossing.[56] The fluorescence yields on SiO_2 can be increased to those observed in solution by co-adsorption of carbon tetrachloride (CCl_4), nitromethane (CH_3NO_2), and tetranitromethane [$C(NO_2)_4$], molecules that normally quench the fluorescence.[55] A decrease in the fluorescence yield is observed for all probes except 9-methylanthracene, which in solution exhibits a fluorescence quantum yield near unity. Techniques used for sample preparation can also have a marked effect on the surface photophysics as seen by the 30% decrease in the fluorescence and triplet quantum yields for adsorbates on large pore silicas following thermal treatment and by the removal of residual water.[55]

Table 1. Fluorescence Quantum Yields for Fluorophores in Solution and on Porous Silica Gel[a,b]

	solution			SiO:solid	
adsorbate	ϕ_F (ref 55)	ϕ_F	τ_{ns}	ϕ_F	τ_{ns}
anthracene	0.30		5	0.20	5
bromopyrene	0.05	0.02	3	0.03	2.8
chrysene	0.17	0.18	45	0.20	19
coronene	0.30		185	0.22	165
diphenylanthracene	0.98	0.92[c]	10	0.91	11.7
fluoranthene	0.24−0.30		53	0.17	45
9-methylanthracene	0.33−0.37		10	0.43	11.4
naphthalene	0.2−0.28	0.23	100	0.28	36
perlyene	0.94−0.98	0.90	6	0.85	5.1
pyrenecarboxaldehyde				0.42	5.6
pyrene	0.65−0.72	0.66	360	0.51	175
pyrenebutyric acid				0.56	159
covalently bound pyrene				0.58	196

[a] Data taken from ref 55. [b] Adsorbates were at 0.45−0.02 μmol/g on 60 Å silica gel (T_a = 150 °C, air) adsorbed from cyclohexane. All fluorophore-doped silica samples were dried under vacuum at 298 K for 2−3 h and then dried at 373 K under vacuum for 15 min to remove residual water adsorbed during the preparation of the samples. The quantum yield of fluorescence (ϕ_F) for pyrene was determined by 29 different sample preparations at the same pyrene loading with a mean of 0.51 and a CV of 5.5%. A difference from 0.51 of ±0.03 is a statistically significant difference at 95% confidence. Determinations for other fluorophores were made on at least two separate sample preparations. The typical difference between the two values was <7% of the average of the measurements. [c] This value was collected using both oxygen and TNM as quenchers. The covalently bound pyrene preparation is discussed under Experimental Techniques. The error for two separate preparations is <±0.04 for the quantum yield and <±4% for the lifetime determination.

Table 2. Triplet Quantum Yields of Several Arenes in Solution and Porous Silica Gel[a,b]

	ϕ_F		
	solution (reference)	SiO_2 solid (present work)	solution (present work)
bromopyrene	0.95	0.91	
coronene	0.56	0.07	0.53 (EtOH)
diphenylanthracene	0.02	0.04	
9-methylanthracene	0.62	0.36	0.59 (EtOH)
pyrene	0.35	0.22	0.35 (CH)

[a] Data take from ref 55. [b] Solution reference results are for ethanol or cyclohexane.[57−61] The solution for 9-methylanthracene using the method of ref 57 is in ethanol. Davisil 60 Å (T_a = 150 °C) was used for the SiO_2 solid. ϕ_T is the quantum yield of the triplet.

4.9. Quenching of Arene Excited States on SiO_2

Due to the heterogeneous nature of the surface, the fluorescence decays of arene probes adsorbed on SiO_2 are not single exponential. However, the data are fitted reasonably well by a double exponential,[54] whereas a Gaussian distribution in the logarithm of the decay rate constant gives excellent results and is more realistic.[20] In this review, most of the kinetics on heterogeneous surfaces are treated via the Gaussian distribution.[20,55,56]

Excited states of molecules adsorbed on SiO_2 surfaces may be quenched in many ways: (a) quench-

ing by bombardment of the excited state by a molecule in the gas or liquid phase above the surface; (b) quenching by surface-adsorbed molecules, which diffuse on the surface; and (c) quenching by adsorbed molecules. Quenching molecules that are located very close to the excited states give rise to static quenching. Examples of this type were indicated earlier.

4.9.1. Quenching by Oxygen, Type a

The rate constant for O_2 quenching of the singlet state of pyrene adsorbed on amorphous silica gel depends on the pore size of the silica and on the method and temperature used to remove adsorbed water and surface silanol groups.[20−55,56] Typical quenching data are shown in Figure 4, where the

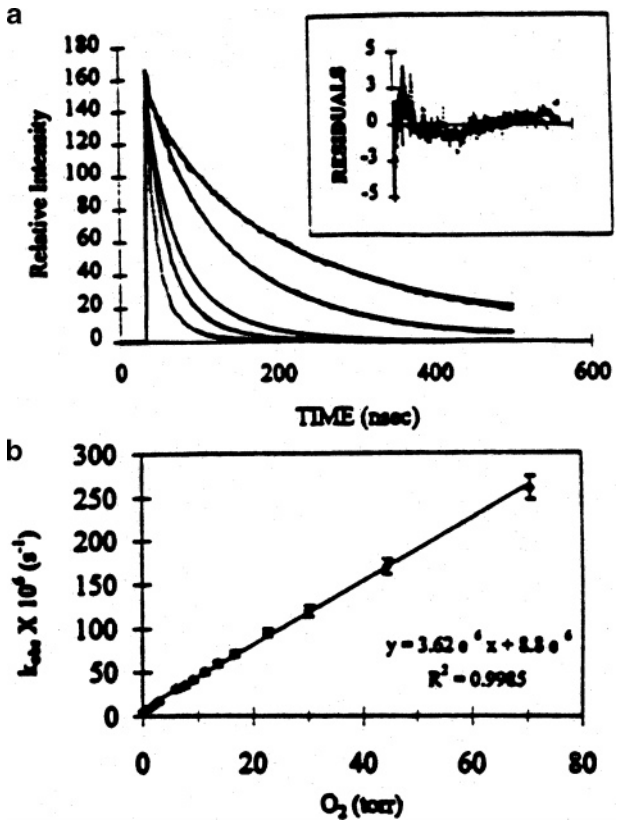

Figure 4. (a) Decay profiles of the pyrene singlet excited state at 400 nm after laser excitation at 337 nm shown with increasing concentrations of added oxygen. Pyrene at 0.5 μmol/g on 60 Å silica pretreated at 150 °C in air was used. From top to bottom decay traces represent oxygen pressures of 0, 0.71, 6.2, 11.7, and 34.5 Torr. The solid lines are the Gaussian fit to the actual data. (Inset) Residual plot for the difference between the actual data and the Gaussian fit. Reprinted with permission from ref 56. Copyright 1999 American Chemical Society. (b) Decay rate constants of the pyrene singlet excited state at 400 nm plotted against increasing oxygen concentration. The solid line is the best-fit line to the actual data. The slope of 3.62 $\times$ 10^6 is in $Torr^{-1}$ s^{-1} as discussed in the text. The 6% error bars were determined from triplicate measurements of the same oxygen pressures using different measurements of the same sample. Reprinted with permission from ref 56. Copyright 1999 American Chemical Society.

quenching rate constant k_q varies linearly with O_2 pressure. There are two possible mechanisms for O_2 quenching of excited pyrene on an SiO_2 surface: quenching by direct collision as in the Eley−Rideal (ER) mechanism and quenching by surface-adsorbed O_2 as in the Langmuir−Hinshelwood (LH) mechanism. Temperature studies distinguish between these two mechanisms, and both mechanisms were found to be operative: the ER mechanism dominates at temperatures >30 °C, and the LH mechanism dominates at lower temperatures, T < 10 °C. Studies on several other surfaces also add insight into the surface processes that are involved. The product of the O_2 quenching of the singlet excited state is the triplet state, and quenching of the singlet state leads to an increase in the triplet yield for both pyrene and coronene. However, it is found that the efficiency of the O_2-induced intersystem crossing is much smaller on the SiO_2 surface compared to that in solution. The pyrene triplet excited state is also quenched by O_2, but unlike the singlet excited state, the quenching mechanism is predominantly ER, or direct collision of O_2 with the excited triplet state on the surface. Typical O_2 quenching rate constants are shown in Table 3. The excited states of coronene, naphthalene,

Table 3. Dynamic Quenching Rate Constants for the Pyrene Singlet Excited State by Oxygen on Various Surfaces at Room Temperature[a,b]

surface	SA (m^2/g)	k_q ($Torr^{-1}$ s^{-1}) $\times$ 10^6	k_q (dm^3 mol^{-1} s^{-1}) $\times$ 10^{10}
M40	680	3.5	6.4
d60	480	3.6	6.49
D150	325	6.6	12.2
Cabosil	325	2.8	5.08
60 Å derivatized	480	8.4	15.4
150 Å derivatized	325	8.3	15.3
SiAl	460	8.5	15.5
Laponite	(310)	1.0	1.83
NaCl[c]	10	4.8	8.6

[a] Data taken from ref 56. [b] M40 is 40 Å Merck, D60 is 60 Å Davisil, D150 is 150 Å Davisil, Cabosil is HS-5 nonporous, SiAl is silica alumina (13% Al_2O_3). All surfaces were pretreated at 150 °C before use, and 0.45 μmol/g pyrene was added from cyclohexane. [c] For NaCl, 0.1 μmol/g pyrene was used.

and pyrenebutyric acid show similar rapid rates of quenching by O_2. A surface such as NaCl that does not adsorb O_2 shows no LH contribution to the quenching.

4.9.2. Quenching by Collision

The k_q from the ER mechanism may be compared to the corresponding rate constant in the gas phase. In the gas phase the O_2 quenching rate constant of singlet excited pyrene by O_2 is reported as 1.9 $\times$ 10^{11} L mol^{-1} s^{-1} at 115 °C and as 2.48 $\times$ 10^{11} L mol^{-1} s^{-1} at 170 °C, whereas that calculated via collision theory is 3.06 $\times$ 10^{11} L mol^{-1} s^{-1}. At 115 °C the rate of quenching is 63% of the calculated rate. The activation energy is small, and to a first approximation the $T^{1/2}$ dependence of k on T is used to calculate k_q at room temperature. In the gas phase reaction k_q is calculated as 1.66 $\times$ 10^{11} M^{-1} s^{-1} at 298 K. On silica surfaces, the measured k_q for O_2 quenching is the sum of the ER and LH mechanisms. The contributions of both the ER and LH mechanisms to the k_q can be calculated, as indicated above, and are given in Table 4, where the rate of the ER process on the

Table 4. Predicted and Measured O_2 Quenching from Collision Encounter at Room Temperature and the Percent of the Gas Phase Rate Constant[a,b]

surface (T_a, °C)	measured rate ($dm^3\ mol^{-1}\ s^{-1}$) $\times\ 10^{10}$	calcd rate ($dm^3\ mol\ s^{-1}$ $\times\ 10^{10}$	%ER	%LH	% of gas phase
NaCl	8.3	8.34	100	0	49
60 Å (150)	6.5	4.65	72	28	27
60 Å (650)	9.5	5.76	61	39	34
Py−SiO_2 (60Å)	15.8	10.7	68	32	63
150 Å (150)	11.2	8.10	72	28	48

[a] Data taken from ref 78. [b] Calculated rates from back extrapolation using the slope and intercept data from plots of $T^{1/2}$ versus temperature. Rates were calculated at 22 °C using the best-fit lines. %ER and %LH are the percentages of Eley−Rideal and Langmuir−Hinshelwood quenching mechanisms for the measured rate, which operates at room temperature as predicted by the temperature data: 0.45 μmol/g pyrene on silica surfaces, 0.1 μmol/g pyrene on sodium chloride.

surface can be compared to that in the gas phase. The surface rate constant is always smaller than that in the gas phase, due to surface shielding of the probe from O_2. Probes adsorbed on the surface must rely on direct collisional encounters, surface diffusion of O_2, and the probe. As the diffusion of pyrene on the SiO_2 surface is negligible, the rate is mainly dependent on the diffusion of O_2.

Table 4 shows that the quenching for probes on the surface is reduced compared to the gas phase by the immobilization of pyrene on the surface and by blocking of the O_2 approach to pyrene on the surface, which can be as much as 50%. The O_2 quenching rate constant in the gas phase, k_g, compared to that on the surface, k_s, may be written as

$$k_s = \frac{1}{2}\left(\frac{(D_{O_2} + D_p)_s}{(D_{O_2} + D_p)_g}\right)k_g \qquad (7)$$

where the D refers to diffusion constants of the reactants in the gas phase and solid phase. In the solid−gas phase reactions, $D_{O_2} \gg D_p$ as pyrene is immobilized at the surface, while O_2 is in the gas phase, and the above equation becomes

$$k_s = \frac{1}{2}\left(\frac{1}{1 + (D_p/D_{O_2})_g}\right)k_g \qquad (9)$$

As the diffusion constant varies as the inverse square root of the molecular weight, giving (D_p/D_{O_2}) as 0.3, and then

$$k_s = 0.5\left(\frac{1}{1.3}\right)k_g \qquad (9)$$

or that k_s/k_g is very close to 0.4.

The data in Table 4 show that ER quenching of pyrene on the SiO_2 surface is less compared to that in the gas phase. Surfaces with low surface curvature, such as NaCl and 150 Å silica, give k_s/k_g of 0.49 and 0.48, respectively, in close agreement with the above picture, whereas the 60 Å silica gives lower values of 0.27−0.34. This reflects on the further surface shielding of pyrene from O_2. The pyrene-derivatized silica acts to place pyrene in a more open position, where it is more accessible to O_2, thereby increasing the k_s/k_g ratio.

4.9.3. Quenching of Triplet States by O_2

Several studies have shown that O_2 quenching of the excited singlet state in solution is efficient and leads to an increase in the triplet yield[62−66] via intersystem crossing. Similar events are also observed for O_2 quenching carried out on SiO_2 surfaces.[55,56] The O_2 singlet excited state quenching mechanism for pyrene on SiO_2 is complex and has been shown to be temperature-dependent. At concentrations of added O_2 below 1 Torr at 298 K, the quantum yields of the pyrene and coronene triplet states increase,[56] and the maximum increase for the pyrene triplet is 20% at ~1 Torr of O_2. Additional O_2 decreases the triplet intensity due to quenching of the triplet excited state. Steady state measurements show that the singlet excited state is quenched by 40% with 1 Torr of added O_2, to give the triplet state. The sum of the quantum yields for pyrene by fluorescence (0.51) and triplet (0.22) is 0.73 for the sample in the absence of O_2. In the presence of O_2, additional triplet is obtained possibly via the mechanism given in the following scheme.

$$P^* \xrightarrow{k_1} P + h\nu$$

$$P^* \xrightarrow{k_2} P^T$$

$$P^* + O_2 \xrightarrow{k_3} P^T + {}^1\Delta O_2$$

$$(Q_T) = 0.73\left[\frac{k_2 + k_3(O_2)}{k_1 + k_2 + k_3(O_2)}\right] \qquad (10)$$

The pyrene triplet is quenched by O_2 with a dynamic quenching rate constant of $1.5 \times 10^5\ Torr^{-1}\ s^{-1}$, ($3 \times 10^9\ L\ mol^{-1}\ s^{-1}$) at 298 K on the 60 Å ($T_a = 150$ °C) silica gel surface. This is >20-fold less than the singlet quenching rate constant of $3.6 \times 10^6\ Torr^{-1}\ s^{-1}$.[56] Although the dynamic quenching rate constant of the triplet is unchanged upon activation of the silica at 600 °C (Table 4), the singlet quenching rate constant on this surface increases by a factor of 1.5 when the activation temperature is increased from 150 to 650 °C. This shows that the surface structure has a less significant impact on the triplet quenching rate than on that of singlet excited state.

Although decreasing the sample temperature increases the concentration of O_2 adsorbed on the surface, it does not increase the dynamic quenching rate constant of the pyrene triplet. At 240 K, the dynamic quenching rate constant is $3.3 \times 10^9\ L\ mol^{-1}\ s^{-1}$, which is within 10% of the value at room temperature. These data suggest that the triplet quenching mechanism results from collisional encounters on the surface, the rate of which only vary as $T^{1/2}$.

The rate of quenching of the pyrene triplet (P^T) state decreases at O_2 pressures >0.5 Torr, which is quite unlike the behavior of the singlet excited state, which continues to rise with increasing O_2.

An explanation for the above behavior is provided by the formation of a complex, C, between P^T and O_2.

$$P^T + O_2 \underset{k_2}{\overset{k_1}{\rightleftharpoons}} C \xrightarrow{k_3} P + {}^1\Delta O_2 \qquad (11)$$

At low pressures the rate constant of process 3 is greater than that of process 1 or 2. Hence, the rate of the reaction may be taken as that of 1. At high pressure, k_1, k_2, and k_3 are comparable and the rate of the reaction is <1. Formation of complexes between excited states of aromatics and O_2 has been used previously to explain O_2 quenching of the arene excited states.[65,66] A similar situation has been suggested for the gas phase quenching of the triplet of triplet benzene and O_2.[67] It is also reported[68] that the efficiency of O_2 quenching of triplet benzophenone on SiO_2 decreases with increasing O_2 content. This study suggests a change in the O_2 quenching mechanism, that is, a change from a Knudsen regime of quenching to a LH mechanism. At this point it is not possible to precisely pinpoint the actual mechanism of O_2 quenching of triplet states of organic molecules adsorbed on SiO_2.

4.9.4. Formation of Singlet Oxygen

As quenching of singlet excited states by O_2 gives rise to excited triplets via intersystem crossing, the subsequent quenching of excited triplet states gives rise to singlet molecular oxygen ($^1\Delta_gO_2$).[69] Direct time-resolved methods were used to study singlet molecular oxygen ($^1\Delta_gO_2$) emission [$^3\Sigma_g$ $O_2(\nu = 0) \leftarrow {}^1\Delta_gO_2$ ($\nu = 0$); 1270 nm] in heterogeneous silica gel/cyclohexane systems,[70,71] where the $^1\Delta_gO_2$ is created through a photosensitization process on silica gel surfaces. The experimental results show that the lifetimes $^1\Delta_gO_2$ in both porous and compressed fumed silica/gel cyclohexane systems are significantly less than that in liquid cyclohexane. This is due mainly to quenching by adsorbed water and silanol groups on the silica gel surface. Monoamines co-adsorbed on the silica gel surface do not quench $^1\Delta_gO_2$, whereas diamines such as DABCO or piperazine maintain their quenching activity, but the quenching kinetics are not of the Stern−Volmer type. It is noted that the $^1\Delta_gO_2$ lifetime increases when the porous silica gel/cyclohexane system is loaded with monoamine, whereas co-adsorption of piperazine increases the quenching of $^1\Delta_gO_2$ by DABCO. These data suggest that at least two situations can occur for the diamine adsorption on the porous silica gel surface. At low levels of monoamine and diamine adsorption, all nitrogen lone pairs are bound to the silica gel surface (i.e., "double" adsorption for diamines), which leads to a low efficiency for quenching of $^1\Delta_gO_2$. Increased loading of diamine, or co-adsorption of other nonreactive diamines, leads to saturation of the double-adsorption sites, giving rise to adsorption at sites where only one nitrogen of the diamine is attached to the silica gel surface, leaving the other free. Increased $^1\Delta_gO_2$ quenching is observed under these conditions.

4.10. Quenching Reactions on SiO_2 with Both Reactants Adsorbed

4.10.1. Diffusion on a SiO_2 Surface, Type b

The process of surface diffusion on silica and that of bombardment of the surface by a gas phase quencher are both shown in the O_2 quenching studies. Several studies have also been carried out that emphasize the photoinduced reaction solely between two adsorbed species. Here, some estimate of the rate of lateral diffusion on the surface and the rate of movement of reactants from one SiO_2 granule to another is obtained. Diffusion, granule to granule, was estimated to occur within minutes, whereas the surface diffusion on a particle occurred in sub-micro- to milliseconds,[72] that is, within the lifetime of arene excited states. To simplify matters, it is important to limit the diffusion of one of the reactants on the surface.

4.10.2. 1-Pyrenebutyric Acid (PBA), Immobilized at the Surface

PBA, via the interaction of the COOH and silanol groups, binds strongly with the SiO_2 surface. Hence, the quenching of the PBA excited state by ferrocene measures the movement of this quencher on SiO_2. Quenching of excited PBA, the pyrene triplet, and the pyrene radical cation, which binds strongly to the surface, by ferrocene indicates that pyrene, and its analogue PBA, are immobilized on the surface for the duration of the quenching process (milliseconds). These data show that quenching occurs by movement of ferrocene. On dry SiO_2 two basic modes of kinetics are observed, an initial static or rapid reaction, together with a subsequent slower homogeneous kinetics. The initial rapid decay is similar to that already discussed using ferrocene as a quencher. The slower and more homogeneous decays give rate data shown in Table 5. The measured rate constants can be expressed in a three-dimensional form of moles per grams or as a two-dimensional surface concentration of moles per meter squared. These rates are at least 10-fold less than those observed in simple solvents and reflect the slower diffusion of the reactants on the SiO_2 surface. Triplet energy transfer

Table 5. Summary of Energy Transfer Rate Constants Obtained from the Pyrene/Ferrocene Systems[a]

nonheated surface	$k_{(obs)}$ (s^{-1})	k_q ($g\ mol^{-1}\ s^{-1}$)	k_q ($m^2\ mol^{-1}\ s^{-1}$)
^{1}pyrene*	4.83×10^6	3.49×10^{11}	1.67×10^{14}
^{3}pyrene	1540	1.61×10^{11}	7.73×10^{12}
pyrene$^+$	3871	2.12×10^9	1.02×10^{12}
surface heated to 450 °C for 24 h			
^{1}pyrene*	4.86×10^6	1.69×10^{11}	7.82×10^{13}

Observed Diffusion Coefficients of Various Adsorbates on Porous Silica Surfaces

system	k ($m^2\ mol^{-1}\ s^{-1}$)	ref
naphthacene (tetracene)/silica gel	1.39×10^{10}	73
acridine/silica gel	8.00×10^{11}	74
2-bromonaphthalene/silica gel	2.40×10^{13}	75
nitropropionic acid/silica gel	2.40×10^{14}	42
naphthalene/silica gel	7.50×10^{13}	76

[a] Data taken from ref 51.

between benzophenone and naphthalene on SiO_2 has been shown to occur via a rapid or static process followed by a slower dynamic one,[76] as in the ferrocene/pyrene system. Other studies[77] measuring the rate of H atom abstraction from diphenylmethane and benzohydral by the benzophenone triplet give rates similar to that of the ferrocene system, that is, 10^{12} m^2 mol^{-1} s^{-1}, or some 10-fold less than those observed in solution.

4.10.3. Quenching by CCl_4

CCl_4 provides a quencher that may quench by bombardment from the gas phase or via surface adsorption.[78] However, temperature studies indicate that quenching occurs by CCl_4 adsorbed on the surface and not by bombardment from the gas phase.[78] The dynamic quenching rate constant of the pyrene singlet excited state increases after high-temperature pretreatment of the silica and results from an increase in the rate of diffusion of CCl_4 on the surface after the high-temperature removal of surface silanol groups.

The dynamic quenching rate constant of the singlet excited state also increases with the pore size. The highest rate constant is observed on a 150 Å silica gel surface, which has been pretreated at 600 °C. A large pore size or smaller surface area and a dehydroxylated surface both contribute to the increased dynamic rate constant, resulting from increased movement of CCl_4 over the surface.

As carbon tetrachloride does not adsorb strongly on the porous silica gel surface, evacuation of the CCl_4-SiO_2 sample readily removes CCl_4 from the gas phase with surface desorption occurring only after several minutes of evacuation.[78,79] Again, the desorption time depends on the pore size and surface silanol group concentration. Similar data have been also obtained for O_2 but only at low temperatures, as the desorption at room temperature[56] is too rapid.

In the CCl_4-pyrene$-SiO_2$ system, photoproducts are generated on the silica surface after extended UV irradiation of the sample, and the product composition is dependent on the reaction conditions. Typically, chloropyrene, dichloropyrene, and other polychlorinated species are among the products formed.

The overall picture is that co-adsorbed CCl_4 only quenches the pyrene fluorescence via surface diffusion of CCl_4, and the rate of this diffusion can be increased by decreasing the surface silanol group concentration. The photoinduced reaction is electron transfer to give the pyrene cation and electron attachment to CCl_4. Subsequent reaction gives rise to chlorinated products of pyrene via the reactions

$$\mathrm{Py} \xrightarrow{h\nu} {}^1\mathrm{Py}, {}^3\mathrm{Py} \xrightarrow{\mathrm{CCl_4}} \mathrm{Py}^{\bullet+} + \mathrm{Cl}^{\bullet} + \mathrm{CCl_3}^{-}$$

$$\text{or } \mathrm{CCl_3}^{\bullet} + \mathrm{Cl}^{-}$$

$$\mathrm{Py}^{\bullet+} + \mathrm{Cl}^{\bullet} \rightarrow \mathrm{PyCl} + \mathrm{H}^{+}$$

$$\xrightarrow{\mathrm{CCl_3}^{\bullet}} \mathrm{PyCCl_3} + \mathrm{H}^{+}$$

4.10.4. Quenching of Excited Pyrene by *N,N′*-Dimethylaniline

Photoinduced CT reactions between adsorbed pyrene and *N,N′*-dimethylaniline (DMA) in porous silica gel have been also examined by fluorescence quenching and transient absorption techniques.[80] The quenching on silica surfaces is diffusion-controlled and gives rise to exciplex formation. The resulting LH type of surface reaction is described quantitatively using a two-dimensional kinetic model. Surface diffusion of DMA is thermally activated and related to the hydrogen-bonding interaction between DMA and the surface hydroxyl groups. The spectral properties of exciplex emission such as the position of the maximum and the quantum yield can be used to characterize the surface environment. Deactivation of the exciplex on silica surfaces via charge recombination is understood in terms of photoassisted electron transfer theory. The low yield of ionic products from dissociation of the contact ion pairs of the exciplex $Py^{\bullet-}/DMA^{\bullet+}$ is attributed to the lack of solvation of the ions by the surface and the low mobilities of ionic species on the surface. Co-adsorption of alcohols facilitates the charge separation. Similar studies[81] have investigated the quenching of the anthracene radical cation on SiO_2 by several amines and azulene. The kinetics are well described either by the Gaussian model or by a fractal approach. The electron transfer from the amine to the anthracene cation is explained on the basis of slow diffusion of the reactants on the surface or by a Marcus inverted region.

4.10.5. Quenching of Excited Pyrene by $C(NO_2)_4$ (TNM), Type c

Quencher molecules that adsorb strongly to the silica gel surface exhibited limited quenching of excited states of co-adsorbed donors, and quenching tends to be predominantly static. Several quenchers including nitromethane, tetranitromethane, and methylviologen[79] behave in this way. The strong adsorption of TNM controls the quenching characteristics of several adsorbed donors, such as the singlet and triplet excited states of pyrene. The mechanism of quenching is determined partially by the adsorption of the co-adsorbed electron acceptors and partially by the surface structure of the porous silica gel support material. Removing the high density of surface silanol groups changes the adsorption characteristics, reduces the adsorption efficiency of both pyrene and TNM, and thus affects the photophysics and photochemistry between co-adsorbed donor and acceptors. With such quenchers the singlet quenching mechanism changes from predominantly static to dynamic as the silanol surface concentration is reduced. TNM movement on the surface is manifested by a decreased rate of quenching when the studies are carried out at lower temperatures.

The pyrene triplet excited state is quenched by TNM at lower adsorbed TNM concentrations than are required for singlet quenching, and the dynamic quenching mechanism of the triplet increases significantly using dehydroxylated silica gel. Spectral studies show that excited state quenching occurs by electron transfer on the surface with the formation of the pyrene radical cation. Nitropyrene is formed along with nitroform, indicating the reaction mechanism involves charge transfer with pyrene radical

cation formation by a similar mechanism as occurs in acetonitrile. A possible mechanism is

$$^3\text{Py}^* \text{ or } ^1\text{Py}^* + \text{TNM} \rightarrow \text{Py}^{\bullet+} + \text{NO}_2 + \text{C(NO}_2)_3^-$$

$$\text{Py}^{\bullet+} + \text{NO}_2 \rightarrow \text{PyNO}_2 + \text{H}^+$$

4.10.6. Reactions of Ions on SiO_2 Surfaces

Many radical cations, for example, pyrene radical cation, the radical cations of distyrylbenzenes,[82−85] etc., are formed on SiO_2 and γ-Al_2O_3 via two photon processes.[85] The cation decays are always nonlinear. An initial fast decay is observed, which decreases with time to give a small net permanent (days) yield of radical cation. With styrylbenzenes, the reaction is completely reversible in minutes and the kinetics are described by the relationship[85]

$$\frac{-\text{d}(c)}{\text{d}} = kt^{-n} \qquad (12)$$

where (c) is the concentration of radical cation, t is time, n is <1.0, and k is a constant. The general kinetic behaviors in the two systems are similar, and the decay of the radical cation is via neutralization by the negative component, that is, the electron. The ion pair is considered to be geminate in nature, and the neutralization occurs by diffusion of the reactant pair[82] or via electron tunneling.[85]

4.11. Trapped Electrons and Their Ensuing Reactions

4.11.1. Photoionization with Light

Spectral studies give valuable information on trapped electrons photogenerated via electron transfer of aromatic compounds on the surface of silica. Figure 5a shows a diffuse reflectance spectrum of a degassed pyrene/silica gel (T_a = 130 °C) irradiated at −196 °C, with light of 320−330 nm wavelength. The absorption bands with λ_{max} at 450, 550, 660, and 725 nm are identified as $Py^{\bullet+}$ for the 450 nm band, and the pyrene dimer radical cations ($Py^+{}_2^{\bullet}$) account for the 550, 660, and 725 nm bands. The coincidence of these bands with those reported in liquids[64] and on other solids[86,87] lends confidence to the assignments. The results indicate that the photoinduced electron transfer on the surface of silica, that is, two photon, occurs via

$$\text{Py/surface} \xrightarrow{2h\nu,\ -196\ ^\circ\text{C}} \text{Py}^{\bullet+} + e_t^-/\text{surface}$$

The symbol e_t^-/surface denotes localized electrons trapped on the surface of silica. In photoionization, it is difficult to discern the e_t^- from other species by UV−vis and EPR spectra. The e_t^- may differ from free electrons or solvated electrons in liquids by being less mobile and more localized. On the other hand, it also differs from the F-center, where the electron is trapped in an anion vacancy and localized. The electrons on silica exhibit a very broad absorption band in the range of 440−690 nm,[88] whereas, for comparison, the localized electrons in the propane

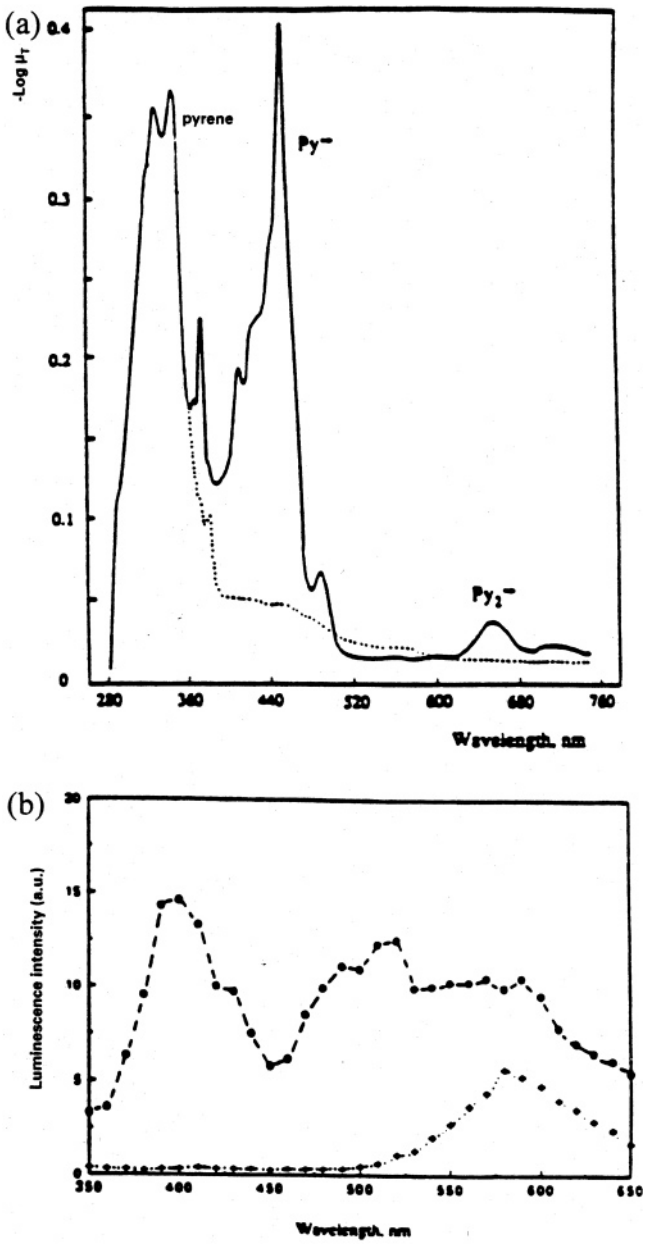

Figure 5. (a) Steady state diffuse reflectance spectra of a pyrene/silica gel (T_a = 130 °C) sample irradiated at −196 °C: (—) measured at ≈ −160 °C; (···) measured after warming up to room temperature. The Py loading concentration was 1.0 × 10^{-6} mol/g; λ_{ex} = 320−350 nm. (b) Thermoluminescence spectrum of a photoirradiated Py/silica gel sample: (- - -) recorded with a fast scanning mode, 10 nm/s; (···) emission at −196 °C after photo-irradiation. The Py loading was 2.0 × 10^{-6} mol/g. The sample was pre-irradiated at −196 °C with a photointensity of 5 × 10^{-6} einstein/cm^2. Reprinted with permission from ref 200. Copyright 1995 Elsevier.

glass (−85 °C) exhibit an absorption in the range of 1000−2000 nm.[89] However, such spectra were not readily observed in the present studies, indicating that the e_t^- in silica takes a different form. The presence of e_t^- is clearly revealed by its ensuing reactions.

Together with the strong spectral absorption and EPR signals, a Py/silica sample, photoirradiation at −196 °C, exhibits weak emission at 590 nm (Figure 5b, dotted line).[84] As the sample temperature is

increased, the intensities of both absorption (Figure 5a) and EPR (data not shown) signals decrease and thermoluminescence appears (Figure 5b, dashed line). Spectral data of pyrene in the literature suggest that[90−92] the thermoluminescence bands are Py fluorescence (360−400 nm), pyrene excimer (480 nm), and phosphorescence of the lowest-lying pyrene triplet state (590 nm). The thermoluminescence, accompanied by the disappearance of $Py^{\bullet+}$, indicates that the luminescence originates from the reaction of trapped electrons with $Py^{\bullet+}$. This suggests that, at −196 °C, the photogenerated electrons are temporarily trapped on the silica gel surface. The weak emisson at −196 °C indicates that even at this low temperature, some e_t^- slowly react with $Py^{\bullet+}$, leading to the formation of the triplet state (^3Py)

$$e_t^-/\text{surface} + Py^{\bullet+} \rightarrow {}^3Py/\text{surface}$$

The triplet, $^3Py^*$, decays either via emitting phosphorescence or via triplet−triplet annihilation, the latter producing excited singlet states ($^1Py^*$) and subsequently the excimer (Py_2^*), which results in the corresponding emission

$${}^3Py^*/\text{surface} \rightarrow {}^1Py/ + h\nu_{pH}$$

$${}^3Py^*/\text{surface} + {}^3Py^*/\text{surface} \rightarrow {}^1Py^*/\text{surface} + {}^1Py/\text{surface}$$

$${}^1Py^*/\text{surface} \rightarrow {}^1Py/\text{surface} + h\nu_{fl}$$

$${}^1Py^*/\text{surface} + {}^1Py/\text{surface} \rightarrow {}^1Py_2/\text{surface} + h\nu_{ex,fl}$$

These data mirror literature reports, where thermal luminescence is observed on recombination of aromatic hydrocarbon radical anions with stable cations, for example, tetramethyl-*p*-phenylenediamine cation. In a similar fashion, triplet−triplet annihilation of excited acridine on silica and alumina surfaces was also observed by Oelkrug.[82]

4.11.2. Nature of Trapped Electrons in SiO_2

Electron trapping in amorphous silica is attributed to pre-existing defects, such as peroxy radicals and E′ centers.

$$e^- + SiO_2 \rightarrow e_t^- \text{ (long lived)}$$

Trapping of excess electrons at deep energy levels in the band gap explains the stability of e_t^- in bulk silica and is illustrated in electron charging measurements.[93] The presence of silanol groups on silica surfaces introduces new electron trapping sites.

$$e^- + (\equiv SiOH)_n \rightarrow e_t^- (\lambda_{max} = 600 \text{ nm}, \tau_{1/2} \approx 50 \text{ ns})$$

These trapping sites have been identified in recent studies utilizing pulsed radiolysis to generate e_t^-;[9,94] the absorption spectrum of these e_t^- is shown in Figure 6a exhibiting a broad λ_{max} at ∼600 nm. The short lifetime precludes the observation of these species in steady state experiments, but pulse radiolysis proves to be an ideal method of producing e^- on SiO_2 for subsequent study.

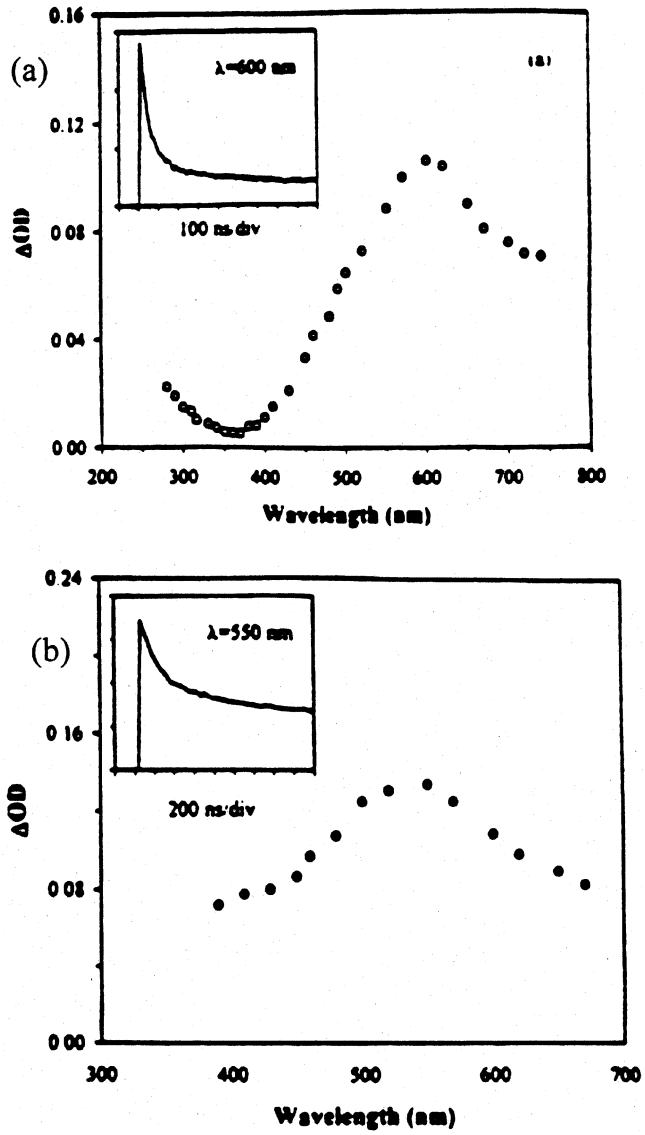

Figure 6. (a) Transient absorption spectrum of trapped electrons on the silica gel D60 surface (T_a = 140 °C), taken at the end of the pulse (∼7 ns). (Inset) Time-resolved decay race monitored at 600 nm. (b) Transient absorption spectrum of surface-trapped holes in blank D60 (T_a = 600 °C). (Inset) Decay trace monitored at 550 nm. Reprinted with permission from ref 9. Copyright 1997 American Chemical Society.

Both of the above electron trapping modes give rise to efficient two photon (λ < 355 nm) photoionization of aromatic adsorbates such as pyrene on silica surfaces. The subsequent slow ion recombination (milliseconds and seconds) in both photolysis and radiolysis experiments suggests that the fast decay of e_t^-, which is independent of the counter radical cation, is due to the transformation into deeper traps in the bulk. The low yield of pyrene radical anions on silica surfaces activated at 150 and 600 °C also indicates that most of the excess electrons are trapped by silica and are not scavenged well by pyrene. On the contrary, the presence of strong electron acceptors such as $CHCl_3$, Cd^{2+}, and MV^{2+} gives rise to efficient scavenging of conduction band

electrons before the formation and localization of e_t^- and excitons. It can be said that the electron affinity of silica is higher than that of biphenyl or pyrene but lower than that of $CHCl_3$ or MV^{2+}. Meanwhile, CT reactions of organic adsorbates with positive holes left in the SiO_2 network give rise to the increased production of radical cations. In radiolysis, hydrogen production from the O−H bond breakage via exciton localization readily occurs in SiO_2. The H atoms are subsequently scavenged by molecules adsorbed on the surface. The efficiency of these scavenging reactions drops asthe size of the primary silica particles increases. This is due, at least partly, to the shielding of H atoms in the bulk SiO_2 from interaction with adsorbed species.

4.11.3. Ionization and Excitons on Radiolysis of SiO_2

When a fully hydroxylated SiO_2 surface is modified by pretreatment at high temperatures as a result of dehydroxylation, fewer H atoms are produced in radiolysis, and more electron−hole pairs are subject to scavenging. This leads to an increased transfer of energy to the radical ion channel and to increased ionic chemistry on silica surfaces. This is shown by radiolytic observation of acidic centers formed on high-temperature-activated silica surfaces and reactions initiated by a cationic mechanism. Approximately 50% of the excitation energy produces hydrogen gas in γ-irradiated silica gel that has been previously dried at 600 °C. This corresponds to a $G(H_2)$ of 1.5, where $G(H_2)$ is the number of hydrogen gas molecules produced per 100 eV of absorbed energy. This corresponds to a $G(H)$ of 3.0. The hydroxyl content of this surface is only 10 times higher than that in bulk quartz, where the hydrogen yield is as low as $G(H) \sim 10^{-2}$.

4.11.4. Radiolysis of SiO_2

Energy transfer processes following irradiation of high surface area silicas may be summarized as follows:

(a) Irradiation produces unrelaxed electron−hole pairs in the amorphous SiO_2 particles.

(b) Splitting of the electron−hole pairs by charge-trapping centers and the charge-scavenging molecules adsorbed on the surface competes with the formation of excitons.

(c) The transfer to and localization of the excitons at surface hydroxyls leads to H atom production.

(d) The variation of the surface chemistry originates from the modulation of the surface hydroxyl content, which is present as an impurity within the band gap. In silicas of small particle size such as silica gels, the surface hydroxyls withdraw the energy via exciton trapping and direct the chemistry of adsorbates into free radical processes.

(e) Dehydroxylation of the surface alters the mode of energy transfer from "free radical" to "ionic" in nature.

The radiolysis or high-energy excitation of SiO_2 is quite different from that of other similar structures, namely, γ-Al_2O_3 and zeolites. The particle-based structure of silica is different from the γ-Al_2O_3 and zeolite frameworks; in the latter the structure is completely exposed to external ions and small molecules. Following high-energy excitation of the zeolite framework the ions act as intrinsic electron-trapping sites, leading to very efficient charge separation. Hence, ionic processes are mainly observed in zeolites and will be discussed subsequently.

Pulse radiolysis has also been used[95−98] to investigate electron transfer from small SiO_2 particles to an aqueous phase surrounding the particles. Essentially, a concentrated colloid of SiO_2 (50% wt SiO_2) is irradiated with fast electrons. The energy of the fast electron is lost to both SiO_2 and the aqueous phase. The studies show that electrons produced on the small SiO_2 particles are ejected into the aqueous phase. Apparently electrons generated directly in the aqueous phase remain in this phase. Positive holes are also generated in the SiO_2 phase. However, these species remain with the SiO_2 particles and do not enter the aqueous phase.

These results may be compared to similar systems where the electrons are generated by two-photon ionization $\lambda_{ex} = 337$ nm at the SiO_2/aqueous interface.[98] The source of the electrons is pyrene attached to the SiO_2 surface via the derivative pyrene butyl trimethylammonium bromide. In this system the radical cation of pyrene is observed at the interface, but no sign is seen of the hydrated electron in the aqueous phase. These data are similar to other photoionization data discussed later. The indication is that in these systems the electron is ejected directly into the SiO_2, where it remains, or reacts rapidly at the surface.

4.11.5. Electron Abstraction from SiO_2 by Photoexcitation

Photoexcitation of many oxidizing species on SiO_2 leads to electron extraction from SiO_2, leading to the formation of the radical anion of the species. A prime example is methylviologen, MV^{2+}. The adsorption of an electron-deficient aromatic cation, the MV^{2+} ion, on silica, exhibits a Langmuir form. The adsorption is strong and chemical analysis of the supernatant shows that >95% of the MV^{2+} ions adsorb on silica gel surfaces within the loading range of $(1-5) \times 10^{-6}$ mol g^{-1}. More than 95% of Cl^- (concomitant anion of MV^{2+}) remain in the solution. The diffuse reflectance spectrum of MV^{2+}/silica gel samples exhibits a spectral absorption with a 10 nm shift with respect to the MV^{2+} absorption band in water. This shift is ascribed to ionic interaction between MV^{2+} and the negative surface sites.

$$MV^{2+} + \text{surface}^{-\delta} \rightarrow (MV^{2+} - \text{surface}^{-\delta})$$

The negative surface sites on silica gel are due to surface texture and are well documented.[17] The nature of the surface complexes may be charge transfer and similar to the ion-pair complexes between MV^{2+} and anions in polar solution.[99−101]

Photoirradiation of a MV^{2+}/silica gel ($T_a = 50$ °C; $\lambda_{ex} = 300$ nm) sample produces a blue color, corresponding to spectral absorptions at 405 and 610 nm.[102,103] According to the literature,[99,101] the bands at 405 and 610 nm are identified as reduced methylviologen, $MV^{\bullet+}$. Time-resolved diffuse reflectance

spectroscopy shows that the formation of $M^{\bullet+}$ is a rapid process and within the resolution time of the detection system, ~100 ns.

Photoinduced charge transfer in the MV^{2+}/silica gel sample is consistent with the fact that the excited MV^{2+} is a very strong oxidant. Early work showed that chloride ions, methanol, and cellulose could be oxidized by excited MV^{2+}.[104,105] A similar mechanism is proposed for MV^{2+} on a silica surface as shown below.

$$MV^{2+} + \text{surface} \rightarrow (MV^{2+})/\text{surface}$$

$$(MV^{2+})^*/\text{surface} \xrightarrow{h\nu} MV^{\bullet+} + h^+/\text{surface}$$

Here h^+/surface denotes the positive charge or its derivatives on the surface.[105] Photoirradiation of $MV^{2+}(Cl^-)_2$ in aqueous solution produces short-lived radical pairs, $MV^{+\bullet}$ and $Cl_2^{\bullet-}$.[101,104] Similarly, MV^{2+} ions are photoreduced by Cl^- ions on silica gel surfaces.[103] It is pertinent to inquire whether there are differences between solution and surface chemistry and how surface sites participate in photoreactions.

The surface-bound $MV^{\bullet+}$ species is stable for several hours in the absence of O_2. Introduction of O_2 or air into the sample removes the blue color and produces the corresponding spectral absorption bands and EPR signal ($O_2^{\bullet-}$) due to reaction of $MV^{\bullet+}$ with O_2:

$$MV^{\bullet+}/\text{surface} + O_2 \rightarrow MV^{2+} + O_2^{\bullet-}/\text{surface}$$

Under oxidative conditions the steady state and time-resolved optical and EPR studies of $M^{\bullet+}$/surface with O_2 [105,106] show the formation of superoxide anion ($O_2^{\bullet-}$) with a reaction rate constant of 2.5×10^5 M^{-1} s^{-1}.

Introduction of CCl_4 vapor into a $MV^{\bullet+}/SiO_2$ sample also results in the disappearance of the characteristic blue color. Following extraction with water, chloride ions (Cl^-) are identified as a reaction product. This shows that the reaction of $M^{\bullet+}$ with CCl_4 is electron transfer in nature and that the reaction may be described in two steps: photogeneration of $MV^{\bullet+}$ and subsequent reaction with CCl_4.[102,106]

$$MV^{\bullet+}/\text{surface} + CCl_4 \rightarrow MV^{2+}/\text{surface} + Cl^- + \text{product}$$

Increasing the vapor pressure of CCl_4 and $MV^{\bullet+}/SiO_2$ samples leads to a more rapid decay of $MV^{\bullet+}$. The decay rates are fitted well by a Gaussian distribution model, with an average rate constant $\bar{k}$ of the reaction between $MV^{\bullet+}$ and CCl_4 of 1.2×10^4 M^{-1} s^{-1}. Studies also show that the reaction of $MV^{\bullet+}$ with CCl_4 is via surface migration rather than by bombardment of the bulk gas phase (CCl_4) to the surface. Utilizing surface models of reaction,[107,108] a two-dimensional rate constant can be calculated as $1.1 \times 10^7 (\text{mol/m}^{-2})^{-1}$ s^{-1} (1.2×10^4 $m^{-1}s^{-1}$).

The reaction rate constants of $MV^{\bullet+}$ with other volatile chloroalkanes adsorbed on SiO_2 are summarized in **Table 6**. The data show that on increasing the degree of chloro substitution in the polychloroalkane, the reaction rate constant increases due to an increase in the electron affinity of these molecules.

Table 6. Reaction Rate Constants of $MV^{\bullet+}/SiO_2$ with Polychloroalkanes on Silica Gel at Room Temperature[a,b]

chloroalkane	rate constant[c] M^{-1} s^{-1}	rate constant[c] $(\text{mol/m}^2)^{-1}$ s^{-1}
carbon tetrachloride	1.2×10^4	1.1×10^7
chloroform	3.5×10^3	2.9×10^6
dichloromethane	1.5×10^3	1.3×10^6
1,2-dichloroethane	1.1×10^3	1.1×10^6
molecular oxygen	2.5×10^5	

[a] Data taken from ref 102. [b] For comparison, the rate constant with O_2 is also presented. The MV^{2+} loading is (3−5) × 10 mol/g. [c] See text.

4.12. Reactions at the SiO_2–Liquid Solvent Interface

Early work in this area, photochemistry at a SiO_2/C_6H_{12} interface, using emission studies has already been quoted.[26] Further studies[109] with transient absorption spectroscopy have been used to observe SiO_2 at several solid SiO_2−liquid interface and to illustrate that different types of conditions can be prearranged for the reactants: (1) where both reactants are in liquid contained in the SiO_2 pore; (2) where one reactant is adsorbed to the SiO_2 surface, with the other in the liquid; (3) where both reactants are at the interface and where the surface captures one of the products of the photoreaction in the liquid; and (4) where pore size in the nanometer range plays a major role in the outcome of the photochemistry.

In category 1 the rate constants decrease with decreasing pore size. In category 2 the rate of approach of the liquid-borne reactants to the surface is controlling and can be defined by simple diffusion theory. The rate of surface capture of cations produced in the liquid phase is significantly less efficient than that of neutral species studied in category 2. Locating both reactants at the SiO_2 surface leads to efficient reaction, but rapid product backreaction leads to low yields of final products compared to the bulk liquid phase. The photochemistry in these unique conditions, which are imposed by surfaces on conventional reactions, are conveniently discussed in terms of what is established in bulk solution.

4.12.1. Surface Solvent Immobilization

Solvent immobilized at a surface is not available to interact with a solute or a probe molecule. Probes such as pyrene are not adsorbed at the silica surface in the presence of polar or aromatic solvents, such as methanol and benzene. The immobilization of some of the solvent, due to surface adsorption, leads to an observed increase in probe concentration in the solvent. For many solvents the monolayer concentrations lie in the millimoles per gram level and correspond to a very small amount of solvent, ~1% of the total volume of solvent routinely used in sample preparation. This has little effect on routine experiments, as the amount of surface-bound solvent

compared to that of the bulk is negligible. However, the effect can be amplified if a solution is saturated with dry silica, leaving a minimal amount of supernatant. The absorption spectra of the probe in the solution before and after addition of silica gel are obtained, thus, allowing direct observation of the change in concentration, which leads to the amount of adsorbed or immobilized solvent. With all solvents the probe concentration in the solvent increases, leading to a concentration change on the order of 10%, and depends on the solvent. The amount of solvent adsorbed in systems with 40 Å pore silica is in the range of 4.1×10^{-3} to 5.7×10^{4} mol g^{-1}.

It is clear that solvents do adsorb strongly on the SiO_2 surface; the strength of the interaction of solvent with the silica gel will determine the equilibrium and so define the nature of the viscous boundary as proposed in other studies.[110] This interface boundary plays a significant role for many reactions at the silica gel−liquid interface, but has a minimal effect on reactions in the free bulk solvent.

4.12.2. Reactions in Pores Containing Solvents, Category 1

Systems in which neither reactant is adsorbed to the surface should exhibit chemistry comparable to that in homogeneous solutions. The quenching reaction takes place in two different environments—in the solvent between particles and also in the solvent in the pores of the particle.

The data show that the quenching rate constant k_q in the pore liquid decreases with decreasing pore size. Studies using phthalic anhydride as a quencher indicate that there is a 25% decrease in the rates of the reaction found for the systems with small pores compared to that found in homogeneous solution. Similar behavior is seen for the O_2 quenching. The decrease in rate is due to hindered diffusion and/or fractal effects within the porous network. A simple explanation can be provided for the fractal nature of the medium. At a typical quencher concentration of 10^{-3} M, the average separation of the quencher molecules is 60 Å and is comparable to the pore dimension of 40−150 Å. This situation tends to "dimensionally" decrease the quencher molecules effectively available to the excited probe molecule. This situation tends to lead to a decreased rate constant. The effect becomes more pronounced as the pore size decreases. It is not possible to separate the fractal and viscosity effects, and both are probably operational.

4.12.3. Oxygen Quenching

As with phthalic anhydride, the bimolecular oxygen quenching rate constant decreases in the presence of the pore network, and data for a number of different pore size silica gels and solvents are summarized in Table 7, where reactions take place in the solvent phase and away from the interface. In comparison to bulk solvent, small pores (≤40 Å) cause a 25% decrease in the rates of reactions between neutral species. Both molecules diffuse freely in the pore solvent phase and the observed decrease in the bimolecular rate constant is due to hindered bulk diffusion and/or to fractal effects and, again, is expected to be of more importance as the pore diameter decreases to sizes shorter than the distances traveled by the probe and quencher; this effect decreases the reaction period.

Table 7. Experimentally Determined Biomolecular Rate Constants for Pyrene Fluorescence Quenching by Oxygen in Solution and in Silica Gel Slurries with Different Pore Sizes[a,b]

solvent	$k_{(q)}$ (M^{-1} s^{-1})
benzene	2.40×10^{10}
benzene−150 Å silica gel	2.31×10^{10}
benzene−60 Å silica gel	1.96×10^{10}
benzene−40 Å slica gel	1.73×10^{10}
acetonitrile	3.30×10^{10}
acetonitrile−150 Å silica gel	2.93×10^{10}
acetonitrile−60 Å silica gel	2.62×10^{10}
acetonitrile−40 Å silica gel	2.49×10^{10}
methanol	2.47×10^{10}
methanol−150 Å silica gel	2.0×10^{10}
methanol−60 Å silica gel	1.9×10^{10}
methanol−40 Å silica gel	1.86×10^{10}

[a] Data taken from ref 109. [b] The probe and quencher are located in the liquid phase in all cases (in the case of methanol, 1-pyrenebutyric acid was used as probe).

4.12.4. Reactions at the Solid–Liquid Interface, Category 2

The probe 1-pyrenebutyric acid (PBA) is the probe of choice to study bimolecular reactions between surface-immobilized probes and solvent phase quencher molecules**.** This probe adsorbs strongly to the surface, even in the case of aromatic solvents and polar solvents such as acetonitrile. The strong adsorption is due to the formation of hydrogen bonds between the carboxylic acid group of the probe and the surface silanol groups. It has also been suggested[17] that chemisorption occurs via an esterification type reaction. As the surface area of the pores is much larger than that of the particle exterior surface, then the observed reactions occur predominantly in the particle interior. Several studies of the PBA excited states at the silica surface and its subsequent quenching by O_2 or phthalic anhydride are reported. As seen previously, the bimolecular O_2 quenching rate constant for excited PBA decreases as the pore size is reduced.

The quenching of PBA fluorescence at the solid−liquid interface by phthalic anhydride parallels the O_2 quenching. These results, the quenching of PBA fluorescence at the solid−liquid interface by phthalic anhydride, are summarized in Table 8.

Table 8. Experimentally Determined Biomolecular Rate Constants for 1-Pyrenebutyric Acid Fluorescence Quenching by Phthalic Anhydride in Solution and in Silica Gel Slurries with Different Pore Sizes[a,b]

solvent	$k_{(q)}$ (M^{-1} s^{-1})
acetonitrile	1.57×10^{10}
acetonitrile−150 Å silica gel	7.05×10^{9}
acetonitrile−60 Å silica gel	5.71×10^{9}
acetonitrile−40 Å silica gel	4.98×10^{9}

[a] Data taken from ref 109. [b] The probe and quencher are located in the liquid phase.

O_2 quenching data for the two situations where the reactants are in the solvent phase and where the reactant is at the interface are shown in Table 9. In

Table 9. Comparison of Bimolecular Rate Constants for Oxygen Quenching of Pyrene at Different Locations Relative to the Interface (60 Å Pore Size Silica Gel)[a]

probe	location	solvent	rate constant	$k_b k_s$
PBA	solvent	pure methanol	2.47×10^{10}	
PBA	solvent	methanol−SiO_2	2.16×10^{10}	1.144
pyrene	solvent	pure benzene	2.60×10^{10}	
pyrene	solvent	benzene−SiO_2	2.10×10^{10}	1.23
PBA	solvent	pure benzene	2.30×10^{10}	
PBA	interface	benzene−SiO_2	6.55×10^{9}	3.51
PBA	solvent	pure cyclohexane	2.0×10^{10}	
PBA	interface	cyclohexane−SiO_2	4.69×10^{9}	4.26
pyrene	solvent	pure cyclohexane	2.3×10^{10}	
pyrene	interface	cyclohexane−SiO_2	3.7×10^{9}	6.21

[a] Data taken from ref 109.

the latter situation, the rates are 3.5−6.2 times smaller than those observed in bulk solvent. The reactions are diffusion-controlled and can be explained as follows. In bulk solution the diffusion-controlled rate constant is given by

$$k_b = 4\pi R(D_A + D_B) \quad (13)$$

where R is the interaction distance, given by the sum of the radii of A and B, and D is the diffusion constant. In solution, $D_A \approx D_B$, but if A is immobilized at the interface, then D_A is zero and diffusion is expressed only by D_B. Due to surface adsorption, A is also only exposed to 50% of the available B. Hence, the above equation for k_i, the rate constant at the interface, is reduced to $k_i = 2\pi R(D_B)$. This indicates that $k_i \approx 1/4\ k_B$ is in good agreement with the data in Table 9.

4.12.5. Reactions with Surface-Adsorbed Quenchers, Category 3

To establish the rate at which reactants in the pore liquid collide with the silica wall, a photosystem was designed to measure the time taken for a species excited in the solvent phase within the pore network to encounter the surface. A porous solid having a surface covered with a "reactive" monolayer of quencher is prepared with the probe in the solvent. On arrival of the excited state species at the "quenching" surface, reaction should be rapid, and the lifetime of the excited state in this environment is a measure of the time it takes for a molecule to diffuse to the surface. The following relationship is applied to the one-dimensional diffusion of a reactant to the surface, where x is the mean displacement of the molecules in a specific time interval and with diffusion coefficient D (cm^2/s).

$$x^2 = 2Dt \quad (14)$$

For example, if the probe travels 70 Å in a silica gel of mean pore diameter 150 Å, then from eq 14, with $D = 4 \times 10^{-5}$ cm^2/s, the time to reach the surface is 28 ns. The resulting fluorescence decay data are fitted with the biexponential model described earlier, where one component is assigned to fluorescence occurring in the bulk solvent outside the particles, whereas the other is assigned to fluorescence that occurs in the pore solvent. The fluorescence decay rate for the bulk solvent remains constant, as no quencher is present in the solvent phase, and the species between particles are large compared to pore size. The decay rate in the pore increases as a function of adsorbed quencher. Two different systems were studied, using pyrene as probe. With benzene as solvent, the first quencher, 1-nitropropionic acid, adsorbs at the solid−liquid interface, whereas the second, methylviologen, is used with acetonitrile as solvent.

Studies with 1-nitropropionic acid show that the time for the arrival of the excited state at the interface is shorter than that calculated above. It appears that adsorption of the probe leads to the NO_2 functional group being located away from the surface and into the solvent above the interface. This in turn is expected to shorten the time for movement of the probe from the solvent to the coated surface.

This concept was confirmed by studies with the quencher methylviologen adsorbed at the interface. This molecule is expected to lie flat on the surface and not to project into the solution phase above the interface. The results concur with this concept, where the time for movement to the interface is now closer to the calculated value (Table 10).

Table 10. Calculated and Experimentally Measured Times for Movement of Molecules to the Surface of Porous Silica Gels of Different Pore Sizes[a]

	time of movement to interface (ns)	
	150 Å	60 Å
calcd benzene	28	4.5
NPA−benzene	20	3
calcd acetonitrile	19	3
MV^{2+}−acetonitrile	20	4

[a] Data taken from ref 109.

The chromophore pyrene may be located at the SiO_2−solvent interface by adsorbing PBA on the surface and by using C_6H_{12} as solvent. The pyrene cation is now observed on laser excitation even though the pyrene chromophore is located away from the SiO_2 surface and into the solvent. A careful study of two-photon ionization of pyrene and perylene in SiO_2−benzene systems (where the chromophores are in the liquid phase) shows that a small yield of photoionization is indeed observed. This yield increases as the pore size decreases. Two-photon photoionization occurs in both bulk C_6H_{12} and benzene. However, the ion recombination is so rapid (20 ps) that few ions remain after a nanosecond time period. In the presence of a SiO_2 surface, electrons are captured prior to neutralization, allowing long-lived ions to be observed. When pyrene or perylene is located close to the surface, that is, in narrow pores, the efficiency of electron capture by the surface increases, and the yield of long-lived ions is increased. This illustrates how a surface can act as an electron

capture agent to intercept the ion−neutralization back reaction.

4.12.6. SiO_2–Polar Liquid Interface

The adsorption of pyrene on SiO_2 is very weak in the presence of polar solvents (e.g., CH_3CN, CH_3OH, etc.). The flash photolysis of pyrene in polar solvents produces pyrene radical cations ($Py^{\bullet+}$) and electrons via two-photon excitation. This effect is stronger in a SiO_2−polar solvent system than in the solvent itself. The rate of decay of the pyrene cation decreases with decreasing pore size and is much slower than that in bulk solutions.[109] This suggests that the pyrene cation is captured by the polar SiO_2 surface while the electron remains in the polar solvent, where it forms a solvated electron.

To measure the rate of radical cation attachment to the SiO_2 surface, use is made of its quenching by solutes in solution. In bulk solution the pyrene cation reacts at a diffusion-controlled rate with either ferrocene or I^-.[111] These reactions are markedly decreased if the pyrene cation is at the SiO_2 surface. A competition may then be set up where the cation reacts with the quencher or with the surface. Capture by the surface leads to stabilization of the radical cation, as its rate of reaction with the quenchers or counteranion is decreased. In the presence of ferrocene an initial fast rate of reaction is observed due to the reaction of $Py^{\bullet+}$ and ferrocene in the bulk, and a slower rate is observed due to that of $Py^{\bullet+}$ with ferrocene at the surface. This monitors the component of the $Py^{\bullet+}$ captured by the surface. In the absence of ferrocene the pore $Py^{\bullet+}$ is all captured by the surface. It is important to determine the proportion of $Py^{\bullet+}$ in the pore that reacts with the surface and that which reacts with ferrocene in the bulk solvent.

In an acetonitrile−silica gel system of SiO_2 pore size 150 Å, the measured rate for surface capture is $5.2 \times 10^6\ s^{-1}$. This is slower than the rates measured for diffusion of the singlet excited state to the surface. The excited singlet state requires a time of the order of nanoseconds to reach the surface. The radical cation takes >6 times longer for surface capture to occur.

For the cation to be adsorbed or captured by the surface, the ion has to penetrate the solvent layer adsorbed at the surface and to reorganize its own solvation sphere. Other studies have reported finite and relatively low adsorption rates for ionic molecules[112−115] at surfaces. The adsorption rates of ionic probes are slower than a diffusion-controlled limit. This was taken as an indication that solvent molecules adsorbed at the surface prevent access to the surface. Alternatively, solvent molecules around the radical cations have to be lost prior to capture at the surface.

Several unique features are imposed on reactions that occur at a solid−liquid interface, features that are distinct from those exhibited by reactions in bulk solvents. Using concepts developed in solution, it is possible to effectively describe the surface effects; new features appear, such as the capture of ions by the surfaces. Polar solvents in contact with the surface hamper the ion as it attempts to penetrate to the surface.

4.13. Interaction of SiO_2 Surfaces with Surfactants

The surfactant Triton X-100 adsorbs strongly on porous SiO_2 both from cyclohexane[116] and from aqueous solution.[117,118] Fluorescence studies with pyrene indicate that the Triton molecules exist as micelle-like aggregates on the SiO_2. These aggregates exist as large domains when the surface coverage is >80% surfactant. The aggregates form at concentrations that are well below the cmc of the surfactant in aqueous solution. The silicas used in these studies were large spheres and present an essentially flat surface for the absorption. Much smaller micelle-like aggregates are formed in the gussets of small pore (150 Å) silica.[116]

4.14. Ultrathin Polymer Coatings on SiO_2 Surfaces

There is much interest in ultrathin polymer films on SiO_2, and most studies use X-ray, STM, and AFM techniques to examine the films.[119] The AFM studies tend to show a patchy morphology of polystyrene films prepared by spin-coating from polymer solutions of 0.05−0.075 wt % polymer. At higher polystyrene concentrations, that is, 0.1 wt % polymer, a continuous film is observed. The fluorescent probe, pyrene butyl trimethylammonium bromide, PN^+, has been incorporated onto the SiO_2 surfaces, and the pyrene fluorescence has been used to monitor polymer films deposited on the SiO_2−PN^+ surface.[120,121] The structure of the pyrene fluorescence, the fluorescence decay rate, and the rate of dynamic quenching and prompt quenching by O_2 of the PBN fluorescence on the SiO_2 have been used to inspect the nature of PMMA and PS films at various degrees of surface coverage. At low coverage, PS films are patchy, whereas PMMA films are continuous. Furthermore, the results were in quantitative agreement with published data from AFM studies of similar systems. The basic concept of these studies is that the presence of the polymer influences the photophysics of the pyrene moiety of the PN^+ probe. Interpretation of the data reflects on the nature of the polymer adsorbed to the silica surface. In particular, the fluorescence technique provides additional information to AFM with regard to the effect of the polymer coatings on the penetration of reactive species, such as O_2, to the probe, that is, to the silica−polymer interface. Information is also contained on the polymer-mediated interaction of molecular dopants, such as pyrene, with the silica surface.

4.15. Geometry-Dependent Reactions on SiO_2

The literature abounds with studies that show a marked cage effect of the solid surface on photophysical reactions. Free radical reactions also exhibit such phenomena in SiO_2 and porous glass.[122−126] The basic concept behind these probing studies is the photolysis of an A−B system to give two fragments, A and B, the reactions of which reflect their surroundings or containment. A favored molecule is dibenzyl ketone (DBK), the photochemistry of which is shown in Scheme 1.[122,124] The extent of the cage effect is

Scheme 1

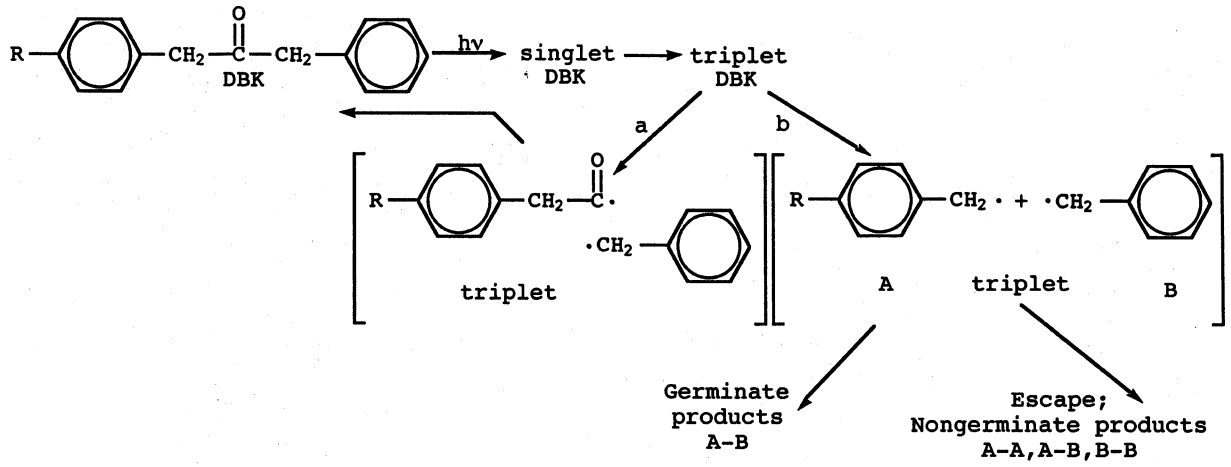

reflected in the relative yield of the products A−B, A−A, and B−B. The cage effect, α, where [AB − (AA + BB)]/[AB + (AA + AB)] × 100%, can be close to zero in homogeneous solvents such as benzene and 2-propanol, where little cage effect is seen and AA:AB:BB is 1:2:1. This ratio can rise to 33% on porous silica, where significant cage effects are observed.

4.16. SiO_2 as an Anchor for Other Oxides

There has been an enormous amount of work on the photochemistry of colloidal semiconductors.[127−130] Silica is an ideal host system for other more catalytically active oxides, many of which are used as industrial catalysts. From a photochemical point of view, TiO_2 is a popular oxide photocatalyst. This may be conveniently prepared as small clusters[128,129] or thin layers[130] on SiO_2. The new material consists of SiO_2 (modified by the high-temperature treatment of the preparation) with small islands of TiO_2.[128,129] Due to the loading of TiO_2 selected, the TiO_2 islands are well separated. Pyrene adsorbs inefficiently on TiO_2, but readily on the silanol groups of SiO_2 surfaces. Random adsorption of pyrene would lead to a large separation of TiO_2 clusters and pyrene molecules. However, the data show that pyrene is adsorbed in close proximity to the TiO_2 clusters. This leads to some quenching of the pyrene fluorescence by the TiO_2, but more so by the Ti^{3+}, which is produced photochemically in the TiO_2 cluster. From earlier studies, little movement of the pyrene is expected during the observations.[51] Photoionization of the pyrene results in pyrene cations and electrons trapped in the TiO_2 clusters. This leads to long-lived ion pairs. The lifetime of the pyrene radical cation is longer in the TiO_2−SiO_2 system compared to that on SiO_2 alone. To a lesser extent, this effect is also observed in the absence of pyrene, where direct excitation of TiO_2 gives long-lived Ti^{3+} and electrons trapped in the silica.

Preformed well-characterized porous silica provides a convenient host for photoactive TiO_2 nanoparticles. Modification of porous silica gel by the addition of active groups such as aluminum or titanium is particularly relevant to heterogeneous catalysis. Adding titania to the surface of silica gel increases the surface activity, and the silica gel support matrix results in a photocatalyst that is easier to handle. The matrix also stabilizes photoinduced charge separation on the surface.

4.17. Summary

To all extents and purposes high surface area silica sponsors all photochemical events that have been established in fluid solution. Transport on the surface is much smaller than diffusion in fluid solution. However, conditions can be arranged such that bimolecular reactions readily occur on the SiO_2 surface. Use can be made of the rigidity of the SiO_2 matrix, in arresting recombination reactions; in particular, photoinduced separation is markedly promoted in the matrix. The constricted porelike nature of the silica is a useful tool to modify, in a fractal sense, radiation-induced reactions in solvent forced into the pores. On silica, charge transfer sites occur to a small extent, but there is no significant observation of the chemistry they may produce. Heating the SiO_2 matrix has only a moderate effect on the chemistry of reactants adsorbed on it. This is not the case with γ-alumina, with which heating produces acidic sites that enrich the chemistry of adsorbed reactants. With this in mind, the review now turns to photoinduced and high radiation induced reactions on γ-Al_2O_3.

5. γ-Alumina

γ-Alumina, Al_2O_3, readily adsorbs organic molecules from alkane solution and the gas phase. Due to its varied forms it can influence both the thermo-[25] and photochemistry of the adsorbates. It is pertinent to first consider several of the varied forms of Al_2O_3. *ACS Monograph 184*[131] gives an extensive account of the many temperature-dependent forms of Al_2O_3 from boehmite to corundum. However, the particular formulation favored by chemists, namely, γ-alumina, is not discussed in detail. This is because γ-alumina tends to be a mixture of several forms.[131] Boehmite, AlOOH, or aluminum oxide-hydroxide, occurs naturally as diaspore and may be made in the laboratory by neutralization of solutions of aluminum salts, to give a gelatinous precipitate that may be associated with AlOOH; treatment under hydrother-

mal conditions gives boehmite crystals. To gain a high surface area material, it is conventional to dry the gelatinous material, and heating of this material leads to γ-alumina. However, heating gives rise to a variety of phases, collectively known as γ-Al_2O_3 or activated alumina. This is the material that possesses great adsorptive power and is technically important. Further heating, in the 400 °C range, creates active Lewis acid sites on the γ-Al_2O_3 surface and has a profound effect on the photochemistry of adsorbed materials. In this review, only γ-Al_2O_3 is considered along with heated material which contains varying degrees of Lewis acid sites.

5.1. Nature of the Surface

The surface of metal oxides is generally covered by hydroxyl layers. Hence, the physisorption between polyaromatic hydrocarbons and surfaces of metal oxides occurs by bonding between these hydroxyl groups and the π-electron system of polyaromatic hydrocarbons.[132,133] Several surface models have been proposed for γ-alumina on the basis of the fact that there are five different OH stretching bands in the infrared spectrum of γ-alumina in the region between 4000 and 1500 cm^{-1}. It is possible to consider the (100) face to be preferentially exposed with an aluminum ion in an octahedral interstice and located immediately below each surface OH group of a fully hydroxylated surface.[134] The dehydroxylation process was simulated by a statistical (Monte Carlo) method assuming a random removal of the equivalent OH pairs, without creation of defects (adjacent oxide ions or holes). The five different OH stretching bands were identified as belonging to OH groups with different numbers of nearest-neighbor oxide ions.

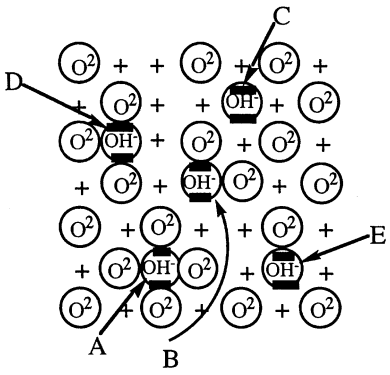

A model based on the coordination of the OH group either to a tetrahedral Al or to an octahedral, to a combination of each, or to both, has been proposed.[135]

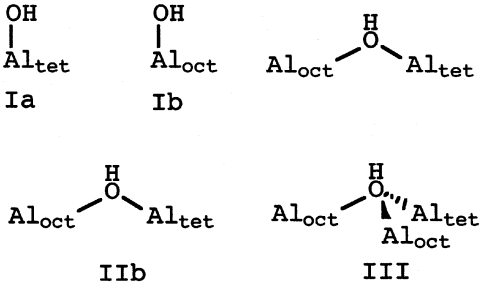

Recently magic-angle-spinning oxygen-17 NMR has been used to characterize various alumina surfaces.[136] The results indicate that type IIa and IIb OH groups (shown above) dominate on the γ-alumina.

According to both models, the effect of pretreatment temperature or heating of the alumina surface has been explained in terms of dehydration of these hydroxyl layers and the formation of Lewis acid sites on the surface. During dehydration, OH groups, which have lower acidity, combine with hydrogen from the neighboring sites of stronger acidity, forming water molecules. This process creates an anion vacancy (Lewis acid site), which exposes a coordinatively unsaturated (CUS) Al^{3+} cation and a cation vacancy (CUS oxygen). Lewis acid sites are strong electron acceptors to which π-electrons from pyrene and its derivatives can be transferred. For these reasons, the colored absorption bands of an arene on γ-Al_2O_3 (e.g., the 450 nm in the pyrene/γ-Al_2O_3) are assigned to that of radical cations (e.g., pyrene radical cation).

A simple representation of heat treatment of the surface of γ-Al_2O_3 may be given as

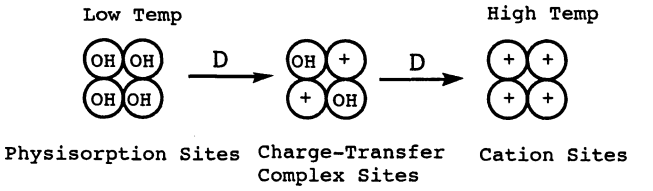

The heating process creates an anion vacancy (Lewis acid site) that exposes CUS aluminum cations and a CUS oxygen.

Co-adsorption of water on an activated γ-Al_2O_3 surface occurs at the Lewis acid sites. This leads to a decrease in the binding ability of these sites toward

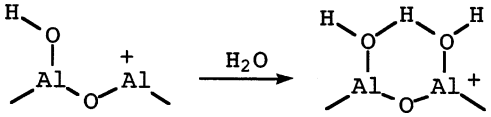

adsorbates, and the fraction of adsorbate adsorbed on the physisorption sites increases, whereas that at the Lewis acid and CUS sites decreases.

A measure of the OH groups/cm^2 compound to that of the Lewis acid sites is given in Table 11.[137]

The prior section on silica indicated that CT sites occur on SiO_2, albeit at low concentrations. It is to

Table 11. Specific Properties of γ-Alumina at Various Pretreatment Temperature (T_a)[a,b]

T_a (°C)	surface area (m^2/g)	OH groups (cm^{-2})	Lewis acid sites[b] (cm^{-2})
130	200	11.5×10^{14}	0.8×10^{14}
250	200	7.8×10^{14}	1.6×10^{14}
350	200	6.2×10^{14}	2.1×10^{14}
450	200	4.6×10^{14}	2.4×10^{14}
750	200	1.3×10^{14}	3.0×10^{14}

[a] Data taken from ref 143. [b] The numbers were taken from ref 133. [c] Calculated from the amount the cation radical of *N*,*N*,*N*′,*N*′-tetramethylbenzidine.

be expected that γ-Al_2O_3 contains (a) physisorption sites, that is, OH groups that via H atom bonding adsorb organic molecules (much like the majority of the sites on SiO_2) and (b) adsorption locations that could give rise to CT adsorption such as Lewis acid and CUS sites. These will vary according to the history of the sample, that is, the degree of thermal treatment that it has experienced, and would be of greater extent than those on SiO_2.

It is instructive to discuss the photophysics and photochemistry of adsorbed guest molecules on γ-Al_2O_3 in terms of the interplay of the physisorption center (PS) and the CT adsorption sites.

5.2. Charge Transfer Sites

As given in Table 11, heating γ-Al_2O_3 increases the extent of surface CT sites. This effect is readily seen by studies of the photophysics of adsorbed arenes on γ-Al_2O_3.[137−148] As in the SiO_2 system, a probe molecule of established photophysics is adsorbed onto γ-Al_2O_3, and the resulting spectroscopy is used to interpret the surface.

5.3. Spectroscopy of Probe Molecules on a γ-Al_2O_3 Surface

5.3.1. Charge Transfer Sites and Mulliken Theory

Excellent examples of this technique are provided by refs 138−141. Here, various arenes are adsorbed to activate γ-alumina (heated at 450 °C for 4 h), β-Ga_2O_3, and TiO_2 (anatase). The physisorbed molecules exhibit ionization and adsorption spectra that are commonly observed in solution. However, broad red-shifted emission bands are also observed, which are characteristic of CT interactions between the arene probe and the oxide surface. It is pertinent to note that with γ-Al_2O_3 the transition energies are proportioned to the ionization potentials of the arenes. This is interpreted via Mulliken CT theory,[147] where

$$h\nu_{CT} = I_D - E_A + C$$

where $h\nu_{CT}$ corresponds to the observed CT emission, I_D is the ionization potential of the donor (arene probe), E_A is the electron affinity of the surface, and C is a constant that depends on the donor−acceptor distance. Figure 7 shows that for several arenes a linear relationship is found between the mean value of the fluorescence and the first excitation maxima on γ-alumina and the I_D of the donor. These data provide convincing evidence of the CT character of the adsorption of arenes on activated γ-Al_2O_3.

5.3.2. Aminopyrene as a Surface Probe

Emission Spectroscopy. Several other photophysical studies also illustrate the increased surface content of CT states of probes adsorbed on heated γ-Al_2O_3. A direct example is provided by aminopyrene (1-AP), where photophysical studies have shown that, in solution, the interplay of the n−π^* and π−π^* states explains the observed solvent-dependent spectroscopy.[41−43] The studies have also demonstrated that protonation of the nitrogen atom of the amino group

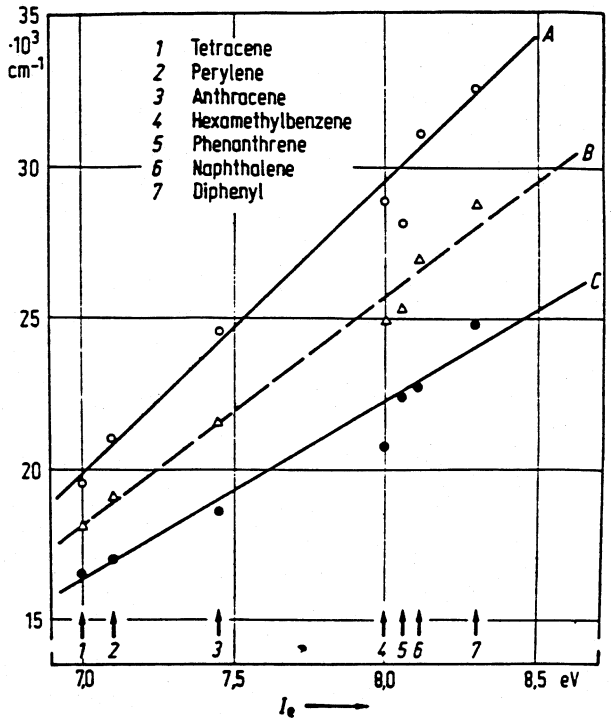

Figure 7. Energies of the CT bands of various aromatic hydrocarbons adsorbed on γ-Al_2O_3 versus the ionization potential of the hydrocarbons: (A) maximum of the absorption band, ν_A; (B) O−O ($\nu_A + \nu_F$)/2; (C) maximum of the fluorescence by ν_F. Reprinted with permission from ref 142. Copyright 1980 *Z. Phys. Chem.*

strongly effects the absorption and fluorescence spectra of AP. The spectral behavior of AP has been used to distinguish geminal and vicinal types of OH groups on silica gel surfaces.

The spectroscopy of aminopyrene on alumina surfaces demonstrates photophysical character that is similar to that on silica. For alumina at low T_a (T_a = 140 °C), adsorbed 1-AP exhibits a broad fluorescence band with a maximum at 440 nm, which is reminiscent of that of 1-AP in hydroxylated polar solvents. When adsorbed on alumina of higher T_a, the long-wavelength emission of the n−π^* states disappears and a pyrene-like emission (exhibiting vibrational structure at the wavelengths around 400 nm) is observed (see Figure 8). The latter emission band, which has the characteristic of π−π^* states, indicates a diminished contribution from the n−π^* state. The effects are explained by Lewis acid sites on the activated alumina, which interact with the lone-paired electrons of the amino group and reduce the interaction of the π-electron system of the pyrene moiety with the amino group, in other words, reducing the contribution from the n−π^* state. These effects are similar to those observed for 1-AP in acidic solutions, where protonation blocks the interaction between electrons of the nitrogen atom and the π-electrons. The emission of AP is characteristic of pyrene on alumina at high T_a.

Absorption Spectroscopy. For Al_2O_3 activated at low T_a, 140 °C, the absorption spectrum of 1-AP is reminiscent of that in polar solvents, together with a small amount of aminopyrene converted to cation radicals. The latter exhibits an absorption maximum at 445 nm.[148] With activation at high T_a, 750 °C, the

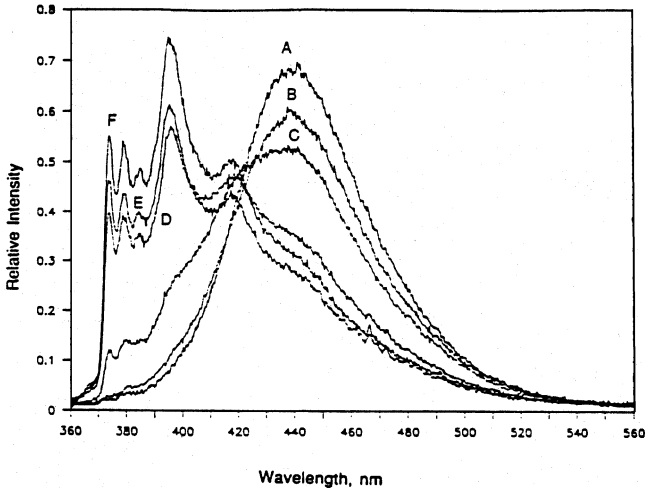

Figure 8. Fluorescence spectra of aminopyrene adsorbed on alumnia at various pretreatment temperatures: (A) un-preteated; (B) 140 °C; (C) 300 °C; (D) 450 °C; (E) 600 °C; (F) 750 °C. Excitation wavelength was 340 nm. Reprinted with permission from ref 144. Copyright 1991 American Chemical Society.

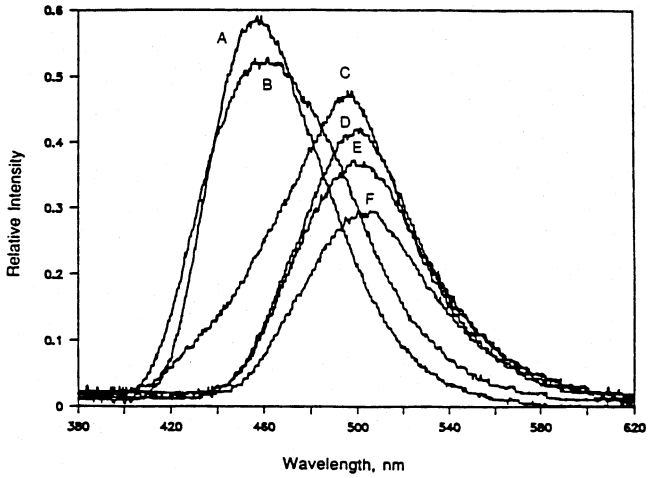

Figure 9. Fluorescence spectra of pyrenecarboxaldehyde adsorbed on alumina at various pretreatment temperatures: (A) un-preteated; (B) 140 °C; (C) 300 °C; (D) 450 °C; (E) 600 °C; (F) 750 °C. Excitation wavelength was 350 nm. Reprinted with permission from ref 144. Copyright 1991 American Chemical Society.

cation-radical formation increases due to the greater number of cation sites on the surfaces, and another absorption band appears in the region of 300−350 nm. The latter absorption band is similar to that of pyrene and/or protonated 1-AP, where the interaction between the two chromophores is inhibited by protonation. This band is attributed to AP adsorbed on the CT complex sites. Excitation of the cation radical of 1-AP on alumina surfaces does not give any observable visible emission.

5.3.3. Pyrenecarboxaldehyde as a Surface Probe

Emission Spectroscopy. Similar data are obtained with pyrenecarboxaldehyde (PCHO). The dependence of the fluorescence of PCHO on the polarity of the solvent has been described in terms of the mixing between $\pi-\pi^*$ and $n-\pi^*$ states in this molecule.[149] The emission of PCHO in nonpolar solvents occurs at shorter wavelengths, but in polar solvents the emission band becomes broader and shifts to longer wavelengths, whereas the emission yield increases dramatically.[150] Figure 9 shows the emission spectra of PCHO excited at 350 nm on alumina of various pretreatment temperatures. Emission of PCHO on the surface at low T_a shows a broad band with the maximum at 450 nm, which is similar to the emission of PA in protic solvent such at alcohols.[150] However, on surfaces with high T_a, PCHO exhibits an emission band with a maximum at 520 nm. Alumina surfaces at intermediate T_a show a combination of these two emission bands.[143]

Absorption Spectroscopy. The addition of an alkane solution of PCHO to alumina of high T_a (T_a = 300−750 °C) produces a greenish yellow color on the surface, which intensifies with increasing pretreatment temperature.

The diffuse reflectance spectra of PCHO adsorbed on two different alumina surfaces are shown in Figure 10. PCHO adsorbed on an alumina surface at T_a = 140 °C exhibits structured absorption bands with peak maxima at 400 and 380 nm, which are

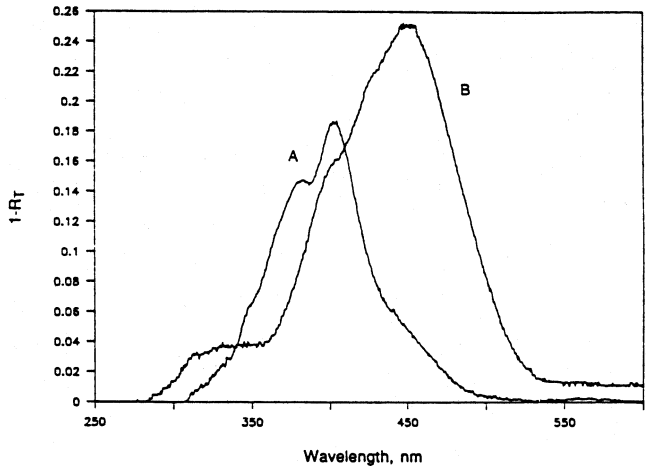

Figure 10. Diffuse reflectance spectra of pyrenecarboxaldehyde adsorbed on alumina at two different pretreatment temperatures: (A) 140 °C; (B) 750 °C. Reprinted with permission from ref 144. Copyright 1991 American Chemical Society.

similar to those of PCHO in solution. PCHO adsorbed on an alumina surface at T_a = 750 °C exhibits an absorption band with a maximum at 450 nm. These data are reminiscent of the earlier pyrene and aminopyrene studies. The Lewis acid sites on activated alumina interact with PCHO, leading to the formation of radical cations of PCHO, which are colored and exhibit emission at 520 nm. Direct excitation at 450 nm of PCHO adsorbed on alumina at T_a = 750 °C strongly supports the suggestion that the emission at 520 nm originates in the excited state of the PA cation radical. The possibility of excimer emission can be ruled out because of the very low loading of PCHO used (1×10^{-7} mol/g). It is pertinent to note that other studies also reported similar emission of the cation radical of PA on type H^+-Y zeolite.[151] It has been shown by ESR and electronic spectroscopic studies that polyaromatic hydrocarbons such as perylene and benzopyrene also form radical cations on silica−alumina cracking catalysts.[152−154] The fluorescence lifetime of this cation radical is

measured to be 6.1 ns. The fluorescence of the PCHO cation radical at 520 nm is quenched by O_2 with the bimolecular quenching rate constant of 5.7×10^6 m^3 mol^{-1} s^{-1}.

5.3.4. Pyrene

Radical Cations on Activated Alumina. Strongly activated γ-Al_2O_3 (T_a = 750 °C) thermally oxidizes several arenes, as illustrated above for PCHO,[143] aminopyrene,[144] and tetramethylbenzidene (TMB).[137] Even pyrene, with a higher ionization potential than the amines, does not escape the attention of the CT site on γ-Al_2O_3.[144] As shown in Figure 11, the absorption spectrum of pyrene adsorbed on alumina at low pretreatment temperature (T_a = 140 °C) shows a structured band with peak maxima at 320 and 340 nm, which are similar to those exhibited by pyrene in homogeneous solutions. However, the spectrum of pyrene on alumina pretreated at high temperature (T_a = 750 °C) exhibits an additional absorption band with a peak maximum around 450 nm. This can become a major absorption band in some samples, and only small absorption remains in the shorter wavelength region, 300−350 nm. The absorption band at 450 nm is reminiscent of the absorption spectrum of the radical cation of pyrene produced in low-temperature glasses.[148] The radical cation of pyrene prepared in trifluoroacetic acid solution containing 22 mol % BF_3−H_2O also exhibits a spectral maximum at 450 nm. The evidence strongly suggests the formation of the pyrene radical cation on γ-Al_2O_3 that has been preheated to 750 °C.

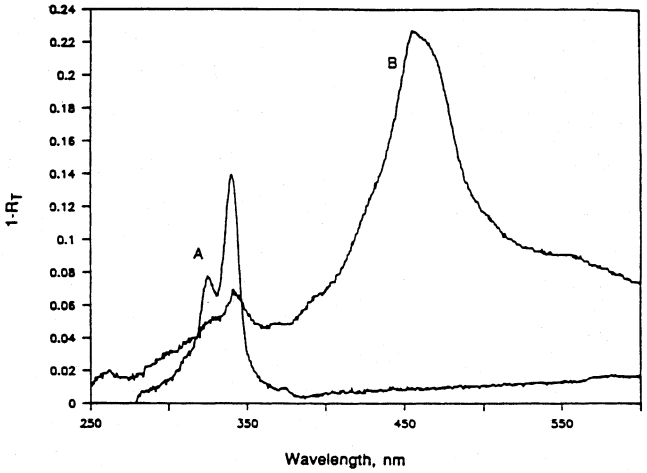

Figure 11. Diffuse reflectance spectra of pyrene adsorbed on alumina at two different pretreatment tempertures: (A) T_a = 140 °C; (B) T_a = 750 °C. Reprinted with permission from ref 144. Copyright 1991 American Chemical Society.

Emission Spectra of Pyrene on Activated Al_2O_3. The amount of pyrene radical cation that is thermally produced on γ-Al_2O_3 (T_a = 750 °C) is significantly less than that of the TMB radical cation.[137] This is probably due to the lower ionization potential of TMB compared to pyrene and to the situation where activation of γ-Al_2O_3 leads to a variety of CT sites of different oxidizing potentials. This is readily observed in the fluorescence of pyrene on γ-Al_2O_3 activated at different temperatures. At low pretreatment temperatures (T_a < 750 °C), the spectra are basically identical with those exhibited by pyrene in polar solvents, for example, water and alcohols. As indicated previously, the hydroxyl groups or the "physisorption sites", dominate on these low-T_a alumina surfaces, and pyrene molecules adsorbed on these alumina surfaces exhibit spectral behavior typically found for pyrene molecules in hydroxylated polar solvents. Increasing the pretreatment temperature leads to marked changes to both the structure and the quantum yield of pyrene fluorescence. Conversely, the fluorescence spectrum of pyrene on high-T_a alumina (T_a = 750 °C) exhibits a smaller III/I, 0.87. This spectrum is similar to that found for pyrene adsorbed on colloidal TiO_2,[155] and in this case, the fluorescence intensity is much less than that of pyrene adsorbed on low-T_a alumina surfaces. In the colloidal TiO_2 system, it has been proposed that pyrene is adsorbed at electron transfer sites. The decrease in the pyrene fluorescence on adsorption to high-T_a alumina surfaces is due to the Lewis acids, where fluorescence is quenched and radical cations are produced. For the sake of convenience, these adsorption sites are denoted as "cation sites". Direct excitation of the pyrene cation on the alumina surface into the 450 nm band does not give rise to any observable visible emission. As the pyrene cations also exhibit IR absorption, fluorescence of these species must also be located in the IR.

5.3.5. Summary of Different Sites on Activated Al_2O_3

As mentioned earlier, there exist at least five types of hydroxyl groups on alumina surfaces. Random dehydroxylation by high-temperature pretreatment creates various coordinatively unsaturated cations, which lead to a variety of charge transfer complex sites and cation sites. Thus, spectral behavior exhibited by pyrene adsorbed on alumina surfaces reveals a specific distribution or combination among these physisorption, CT complex, and cation sites. From the spectroscopic point of view, it can be rationalized that physisorption sites dominate on the low-T_a alumina surfaces, where adsorbed pyrenes exhibit absorption and emission spectra similar to those of pyrene in hydroxylated polar solvents. Pyrene adsorbed on the CT complex sites exhibits a fluorescence spectrum unlike that found in solutions but which similar to that found in colloidal TiO_s, whereas pyrene adsorbed on the cation sites does not fluoresce but exhibits a cation absorption band at 450 nm. The distribution of these adsorption sites is dependent on pretreatment temperature as follows:

$$\text{OH only physisorption sites} \xrightarrow{\text{low } T_a}$$

$$\text{OH + Lewis acid sites CT complex sites} \xrightarrow{\text{high } T_a} \text{Lewis acid and cation sites}$$

5.4. Quenching Reactions of Excited Arenes on γ-Al_2O_3

It is instructive to compare the quenching of the fluorescence of pyrene adsorbed on γ-Al_2O_3 to what has been stated earlier for SiO_2.

5.4.1. Oxygen Quenching at the Solid–Gas Surfaces

The interaction of singlet excited states of pyrene with molecular oxygen on two dry solid alumina surfaces, $T_a = 140$ and 750 °C, has been reported. In both cases the data are consistent with the Gaussian distribution model. The time-resolved fluorescence decays of pyrene on alumina at $T_a = 140$ °C and their simulated Gaussian decays at various amounts of oxygen are shown in Figure 12. A linear relationship

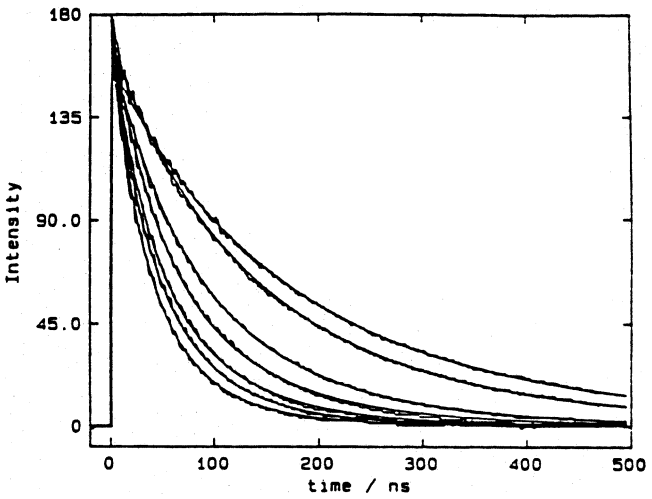

Figure 12. Fluorescence decays of pyrene adsorbed on alumina ($T_a = 140$ °C) with various equilibrium pressures of oxygen: (from top to bottom) 0, 0.23, 0.69, 1.27, 1.61, 1.96, and 2.3 Torr. Reprinted with permission from ref 144. Copyright 1991 American Chemical Society.

of the plots of the observed decay rates $\bar{k}_{obs}$ versus the pressure of O_2, as shown in Figure 13, allows the

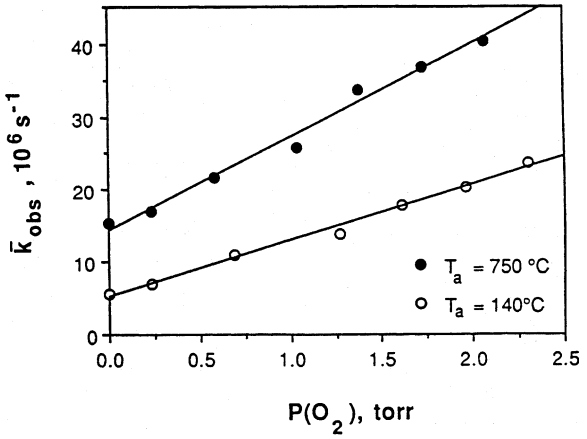

Figure 13. Decay rate constants of fluorescence for pyrene adsorbed on alumina at $T_a = 140$ and 750 °C as a function of the pressure of oxygen. Reprinted with permission from ref 144. Copyright 1991 American Chemical Society.

calculation of bimolecular quenching rate constants, which are found to be 1.41×10^8 and 2.64×10^8 m^3 mol^{-1} s^{-1} for the surfaces with $T_1 = 140$ and 750 °C, respectively. These numbers are in the same range as those reported in the literature for oxygen quenching of anthracene in the vapor phase [$(1.75-1.88) \times 10^8$ m^3 mol^{-1} s^{-1}].[156,157]

With silica gel, the mechanism of oxygen quenching of surface-adsorbed $^1P^*$ has been proposed to be of the Langmuir–Hinshelwood type, where the efficiency of the quenching process depends on adsorption of oxygen to the surfaces.[20] Another unique feature is that decreasing temperature leads to a higher quenching efficiency. To distinguish the mechanism of oxygen quenching on the alumina surfaces, this unique effect of temperature on the oxygen quenching of $^1P^*$ was studied on an alumina surface at $T_a = 140$ °C. Figure 14 represents the plot of I_0/I

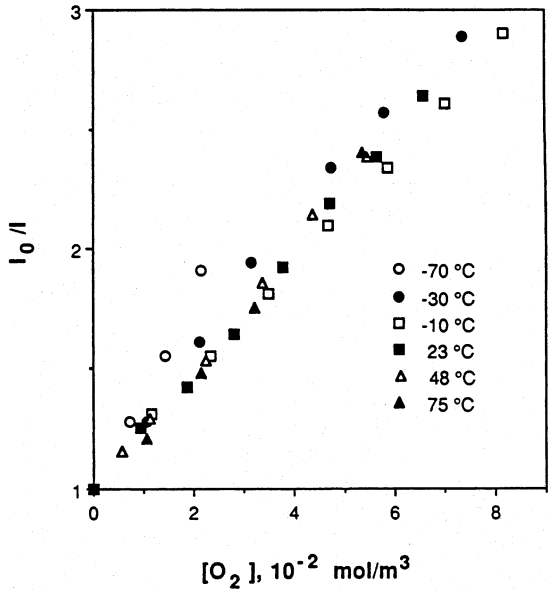

Figure 14. Steady state oxygen quenching of $^1Py^*$ on alumina at $T_a = 140$ °C at various temperatures. Reprinted with permission from ref 144. Copyright 1991 American Chemical Society.

versus $[O_2]$, where I_0/I is the ratio of steady state fluorescence intensity (monitored at 373 nm) in the absence of oxygen, I_0, to the intensity in the presence of oxygen, I; the studies are shown at various temperatures.[144]

The relationship between the steady state fluorescence intensities and quenching rate constants, based on the Gaussian distribution model, is given by

$$\frac{I_0}{I} = \exp\left(\frac{(\gamma_0)^2 - (\gamma_{obs})^2}{4}\right)\frac{\bar{k}_{obs}}{\bar{k}_0} \qquad (15)$$

the various symbols having been defined previously. In the present study, it was found that the γ parameter does not change significantly with the concentration of the quencher, O_2. Equation 15 then becomes

$$\frac{I_0}{I} = \mathrm{I} + \frac{k'_q}{k_0}[\text{quencher}]$$

The slope of the plot of I_0/I versus [oxygen] yields the value of k'_q/k_0, and subsequently the value of k'_q can be calculated.

The efficiency of the quenching process, which was determined as $k'_q/\bar{k}_0$ from the above plot, decreases with decreasing temperature from 75 to −10 °C, but increases with temperature over the range from −30 to −70 °C. This indicates that over the range from 75 to −10 °C, where the oxygen adsorption is rela-

tively small, the mechanism of the quenching process is a bombardment from the gas phase or Eley−Rideal kinetics; however, the mechanism switches to Langmuir−Hinshelwood kinetics at low temperatures when oxygen adsorption on the surface increases. The bimolecular quenching rate constants were calculated to be 1.51×10^8, 1.47×10^8, 1.43×10^8, and 1.31×10^8 m^3 mol^{-1} s^{-1} at 75, 48, 23, and −10 °C, respectively. These numbers are in agreement with the results from the time-resolved studies, but they are ~3 times greater than the values found for the quenching of $^1P^*$ on silica gel surfaces,[20] that is, 5.12×10^7 m^3 mol^{-1} s^{-1}. This also bears out the hypothesis that, at ambient temperatures, the mechanism for oxygen quenching on the alumina surfaces is via O_2 bombardment from the gas phase, or an ER mechanism.

If the bombardment mechanism is operative at the high temperatures, then the quenching rate constant should be proportional to the frequency of surface collisions. The total collisional frequency per unit area, Z, is related to the absolute temperature by the equation[52]

$$Z = n(kT/2\pi m)^{1/2} \quad (16)$$

where n and m are the concentration and the mass of oxygen, respectively. Equation 16 predicts that the ratios of k_q' at 23, 48, and 75 °C to k_q' at −10 °C are 1.06, 1.10, and 1.15, which agrees with the measured values of this study, 1.09, 1.12, and 1.15. This indicates that oxygen quenching on alumina surfaces at higher temperatures takes place via an O_2 bombardment mechanism.

5.4.2. Quenching of Excited Pyrene by Co-adsorbed CH_3NO_2 and Nitrobenzene

Both co-adsorbed CH_3NO_2 and nitrobenzene quench the fluorescence of co-adsorbed pyrene adsorbed on γ-Al_2O_3, the nature of the kinetics depending on T_a. At low T_a a linear relationship is found between [quencher] and the rate of decay of the fluorescence.

The dependence of the quenching process on surface pretreatment is illustrated by the quenching of $^1P^*$ by nitrobenzene on alumina at various pretreatment temperatures (Figure 15). Increasing the pretreatment temperature not only increases the number of Lewis acid sites, which can be seen from the change in the distribution width γ, but also decreases the bimolecular quenching rates k_q'. There is little change in the shape-compared fluorescence decays of pyrene adsorbed on the alumina surface ($T_a = 300$ °C) with various amounts of co-adsorbed nitrobenzene. Two possible interpretations can be drawn: first, the quenching efficiency may decrease with increasing pretreatment temperature; and second, the quenching may switch from dynamic to static in nature. The actual pyrene fluorescence decays given in Figure 15 show that the initial fluorescence intensity, $I_{t=0}$, drops sharply with increasing co-adsorbed nitrobenzene. Clearly this indicates that quenching of the pyrene excited state adsorbed on the CT sites must be static in nature. In other words, the probe and the quencher molecules are bound in close proximity so that quenching occurs well within the response time of the system ($t < 10^{-9}$ s). Similar data are obtained with alumina activated at high temperature, for example, 750 °C, at which the lifetime of the fluorescence of adsorbed pyrene is independent of quencher.

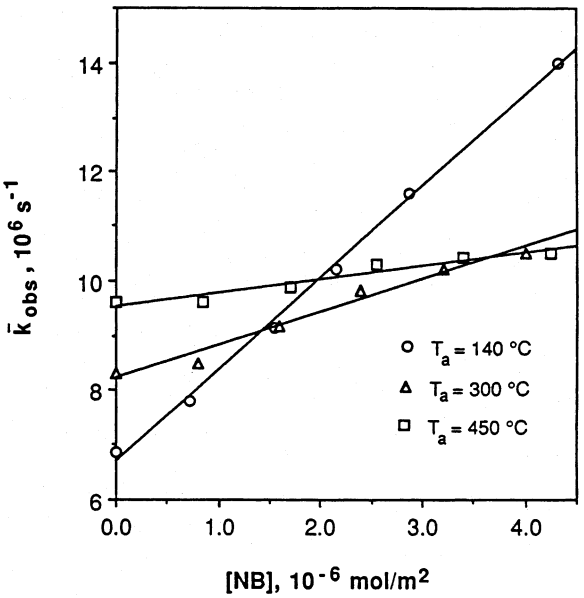

Figure 15. Decay rate constants of fluorescence for pyrene adsorbed on alumina surfaces as a function of nitrobenzene concentration. Reprinted with permission from ref 144. Copyright 1991 American Chemical Society.

Studies of pyrene fluorescence quenching by co-adsorbed nitromethane on alumina surfaces exhibit similar behavior. The quenching parameters of P* by CH_3NO_2 and nitrobenzene are summarized in Table 12.

Table 12. Quenching Parameters of $^1P^*$ with Various Quenchers[a]

quencher	T_a (°C)	γ	k_q' [b] (mol^{-1} s^{-1})
NB	140	0.42 ± 0.02	1.68×10^{12}
	300	0.54 ± 0.05	6.09×10^{11}
	450	0.61 ± 0.07	2.36×10^{11}
	750	1.57 ± 0.10	0
NM	140	0.42 ± 0.03	1.49×10^{11}
	300	0.55 ± 0.05	2.50×10^{11}
	750	1.56 ± 0.11	0
O_2	140	0.43 ± 0.03	5.70×10^6 [b]
	320	0.53 ± 0.05	5.84×10^6 [b]
	460	0.61 ± 0.01	6.31×10^6 [b]
	750	1.27 ± 0.04	7.57×10^6 [b]

[a] Data taken from ref 144. [b] The concentrations of oxygen were calculated from the solubility of oxygen in cyclohexane; the quenching rate constants are therefore represented in the units of m^3 mol^{-1} s^{-1}.

5.5. Surface Trapping of Electrons

Photoexcitation of arenes ($\lambda_{ex} = 320-350$ nm) on γ-Al_2O_3 produces arene radical cations, *but* there is no evidence of the concomitant negative part or electron.[144] However, the concomitant radical cations have long lifetimes of the order of seconds. The complex decay kinetics of the radical cations are due to electron tunneling between the radical cation and an unidentified surface-trapped negative species.

This is quite different from e^- trapped in OH groups on silica, where spectra typical of trapped electrons e^- are observed and the species have short lifetimes.[9]

5.5.1. Spectroscopy of Trapped Electrons e_t^-

Electrons trapped by surface OH groups may be observed on low-T_a γ-Al_2O_3 by radiolytic methods. This method eliminates interference from scattered laser emission. Figure 16 shows the spectrum of

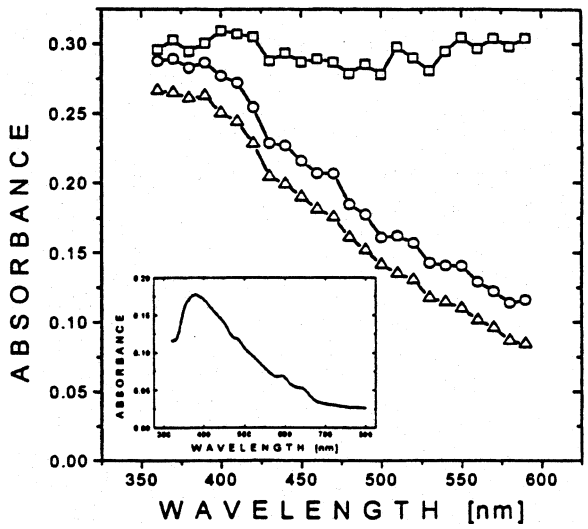

Figure 16. Pulse radiolysis data of γ-alumina obtained with a 2-ns pulse of 0.4 MeV electrons. Spectra were taken after the pulse (□) and at 1 (○) and 9 ms (△). (Inset) Long-lived species at 77 K after γ-irradiation with a dose of 8 kGy. Reprinted with permission from ref 146. Copyright 2003 American Chemical Society.

short-lived species obtained in the pulse radiolysis of γ-alumina in a vacuum (<1 mTorr).[146] The spectrum is essentially featureless, although the spectrum at longer times indicates a maximum below 400 nm. The maximum below 400 nm at 370 nm is confirmed by steady state experiments at 77 K and irradiation with γ-rays, as shown as an inset in Figure 16.

The spectra of Figure 16 are consistent with an initial rapid decay followed by a much slower one. Typical data to illustrate this point are given in Figure 17. It is noted that the rate of the initial sharp decay decreases smoothly with decreasing wavelength for 590−360 nm. The rapid decay is removed by SF_6 and O_2, whereas the long-lived decay is unaffected. The specificity of the reaction of SF_6 and O_2 with electrons indicates that the short-lived decay is due to surface-trapped electrons.

5.5.2. Kinetics of e_t^- Decay

The kinetics of the electron decay in Figure 17 are not well described by tunneling or any simple kinetic order. A good fit is obtained via an equation of the type[158,159]

$$I = I_0\, e^{-(kt)^\beta} \qquad (17)$$

The best fit is obtained with $\beta = 0.4$, as shown in Table 13. In these calculations, the long-lived component shown in Figure 16, obtained at 8 μs, was subtracted from the data at shorter time, and only the short-lived component was described by eq 17. The fits of experiment and theory are shown in Figure 17 (inset). It is noted that the kinetics are identical at two different radiation doses, as required by eq 17. This type of kinetics and formulation is akin to geminate ion kinetics. In liquid systems, the exponent in time is (−0.6) and reflects on the geminate and three-dimensional nature of the system.[158,159] In the present Al_2O_3 system, the geminate ion recombination occurs on a surface (i.e., in two dimensions). This is reflected in a reduced exponent in time, that is, $t^{-0.4}$. Hence, the decays of Figure 17 are attributed to geminate ion decay of the trapped electron e_t^- with its concomitant positive ion. The surface of γ-Al_2O_3 is rich in OH groups, and it is suggested that positive hole h^+, which is produced initially along with e^-, rapidly decays to H^+.

$$h^+ + {-}OH \rightarrow {-}O^- + H^+ \qquad (18)$$

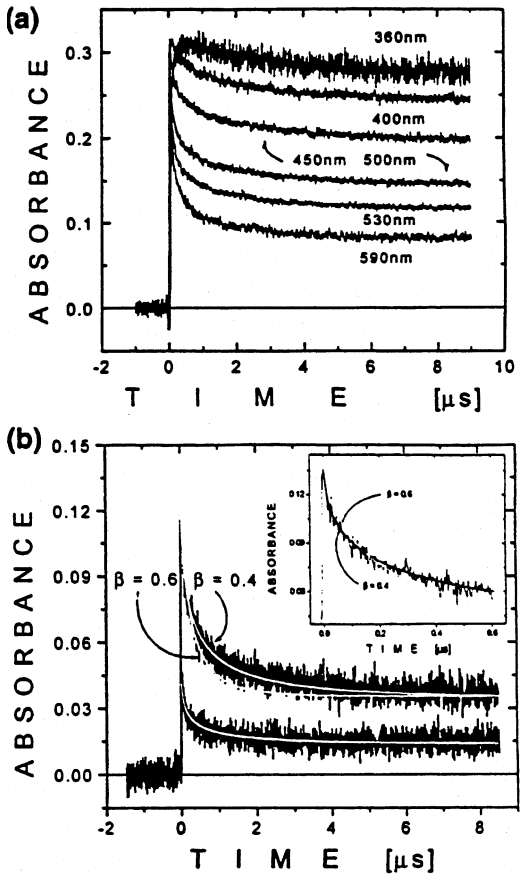

Figure 17. (a) Decay of e_t^- at various wavelengths. (b) Fitting of e_t^- decay at 590 nm to $I = I_0 e^{-(kt)^\beta}$. Parameters obtained are listed in Table 1. Reprinted with permission from ref 146. Copyright 2003 American Chemical Society.

Table 13. Parameters Used in Fitting the Electron Decays[a]

sample	I_0	k (s^{-1})	β	long-lived component
higher intensity	0.108	4.5×10^6	0.4	0.0355
lower intensity	0.035	4.5×10^6	0.4	0.0135

[a] Data taken from ref 146.

The geminate ion recombination that is observed is then the proton with e_t^- to give an H atom.

$$H^+ + e^- \rightarrow H^\bullet \quad (19)$$

Subsequently, the H atoms dimerize to produce H_2 gas, as observed on irradiation of these systems. Prior heating of the γ-alumina for 4 h at 450 °C eliminates the fast decay, whereas the long-lived decay is unaffected. This treatment decreases the surface OH content from 11.5×10^{14}/cm^2 while increasing the Lewis acid site concentration from 0.8×10^{14} to 2.4×10^{14}/cm^2. These data suggest the following mechanism: Radiolysis produces e^- and h^+. The yield of these species is significant, $G > 1.0$ species/100 eV. Both e^- and h^+ move to the surface, where they react with surface-adsorbed arenes to give radical ions. The H atom adduct is also formed via the interaction of P^- with H^+ formed in the original radiolysis process,

$$h^+, e_t^- + \text{arene} \rightarrow \text{arene radical ions} \quad (20)$$

followed by

$$\text{arene}^{\bullet -} + H^+ \rightarrow (\text{arene, H}) \quad (21)$$

These precise processes have been observed previously in methanol solution[160] and in polymer films.[161]

5.6. Hydrogen Atoms Formed in Radiolysis

In the absence of surface-adsorbed materials, H atoms are formed as indicated by the large yield of hydrogen gas produced on radiolysis of γ-Al_2O_3. The yield of H_2 on γ-Al_2O_3 is almost as large as that on SiO_2 and larger than that on zeolites, a solid that contains few OH groups. In SiO_2, it was shown[9] that H_2 was produced via H atom recombination on the surface, this process competing with H atom reactions with surface-adsorbed material. The similarity of the hydroxylated surfaces of SiO_2 and γ-Al_2O_3 and the similar yields of H_2 suggest that similar processes produce H_2 in both systems.

5.7. Summary of Radiolysis of γ-Al_2O_3

It can be concluded that electrons and positive holes can be produced on irradiation of γ-Al_2O_3 with 0.4 M eV of electrons. These species migrate to the surface of the solid, there producing chemical products of adsorbed molecules and also being trapped by surface OH groups. This chemistry is much akin to that observed in the radiolysis of zeolites but unlike that observed in porous silica, where excitonic chemistry is prevalent. It is well-known that excitation of amorphous SiO_2 leads to the formation of bound electron−hole pairs or excitons.[162−165] These singlet excitons rapidly decay (250 fs) to triplet excitons.[166] The free excitons can be localized at surface OH, causing a cleavage of the O−H band, giving $>SiO^\bullet$ and an H atom. In the case of zeolites and γ-alumina, the main role of excitation is ionization, and the subsequent surface chemistry directly reflects an ionic situation.

5.8. Final Products of Excitation of Arenes on γ-Al_2O_3

5.8.1. Initial Formation of Radical Cations

The foregoing studies have indicated that radical cations of guest molecules are formed on both SiO_2 and γ-Al_2O_3 surfaces. In the latter case the "history" of the sample dictates the extent of this electron transfer reaction. The subsequent reactions of the radical cations give rise to stable chemical products.[87,167−169] Earlier it was shown that pyrene molecules adsorb on γ-Al_2O_3 surfaces to form CT complexes. These species are formed at activated sites of γ-alumina and silica−alumina, which are generated by preheating the solids to $T_a > 350$ °C. The CT complexes exhibit absorption bands near the red edge of the characteristic absorption band of pyrene molecules. The radical cations formed on photoexcitation of the CT complexes adsorb strongly on the surfaces. These species exhibit a multilined EPR signal and characteristic UV−visible spectra. Diffuse reflectance studies show that the radical cations also interact with their parent molecules, forming monopositive dimeric radical cations.

5.8.2. Reactions of Radical Cations

The most prevalent reaction of the radical cation on the surfaces is hydrolysis. The photochemical products on both activated and nonactivated surfaces were separated by HPLC, and the collected fractions were studied spectroscopically. The pH dependence of the absorption and fluorescence spectra taken together with results of mass spectrometry indicates that the main products are hydroxypyrenes. Water reacts with the radical cation, forming the radical $Pyr(OH)^\bullet$, which is a key intermediate in subsequent reactions.

According to the above studies, the following reaction mechanism can be proposed for the reaction of $Pyr^{\bullet +}$. The latter is involved in a rapid equilibrium to form an adduct, which subsequently deprotonates to form the $Pyr(OH)^\bullet$ radical.

$$Pyr^{\bullet +} + H_2O \rightarrow Pyr(OH_2)^{\bullet +} \quad (22)$$

$$Pyr(OH_2)^{\bullet +} + H_2O \rightleftharpoons Pyr(OH)^{\bullet +}\, H_3O^+ \quad (23)$$

Although it was not directly observed in the experiments, the $Pyr(OH)^\bullet$ radical is proposed as an intermediate in the present system. However, such radicals are established in radiation chemistry, for example, for $OH^\bullet$ addition to benzene, methylated benzenes, biphenyl,[169,171] and pyrene.[172] It was proposed that formation of the radical cations was carried out through protonation of the hydroxyl radical adduct with subsequent elimination of water,[170] that is, reactions similar to the reverse reactions of 23 and 22. However, the experiments show that in the present system the reverse reaction 23 is inefficient even in concentrated $HClO_4$ (10 M). Similar data are reported for benzene radical cations, where the hydration of the benzene radical cation is practically irreversible.[169,171,173]

The rate-determining step could be the electron transfer from $Pyr(OH)^{\bullet}$ to $Pyr^{\bullet+}$. The products of the redox process can be hydroxypyrene or $Pyr(OH)^{+}$ cation.[174] The latter reacts further with water leading to dihydroxypyrene

$$Pyr(OH)\bullet + Pyr\bullet+ \rightarrow \begin{cases} PyrOH + Pyr + H^{+} \\ Pyr(OH)^{+} + Pyr \end{cases} \quad (24)$$

$$Pyr(OH)^{+} + 2H_2O \rightarrow Pyr(OH_2) + H_3O^{+} \quad (25)$$

The reaction of perylene radical cations with water in homogeneous solution produces 3,10-perylenequinone and perylene.[175] The reaction of 9,10-diphenylanthracene radical cation with water in acetonitrile gives equal amounts of *trans*-9,10-dihydro-9,10-dihydroxy-9,10-diphenylanthracene and 9,10-diphenylanthracene.[175] A similar reaction mechanism could be expected for $Pyr^{\bullet+}$ on γ-alumina and silica–alumina surfaces.

The influence of ferricyanide ion, $Fe(CN)_6^{3-}$, and O_2 on the product distribution further supports the hypothesis of $Pyr(OH)^{\bullet}$ radicals as key intermediates, where the presence of $Fe(CN)_6^{3-}$ (5×10^{-4} M) enhances the yield of the dihydroxypyrene. $Fe(CN)_6^{3-}$ can react as an electron acceptor instead of $Pyr^{\bullet+}$ in reaction (eq 24), resulting in a greater yield of hydroxy products. This reaction is similar to that in radiation chemistry, where $OH^{\bullet}$ radical adducts are quantitatively converted to hydroxy compounds.[176] However, in radiation chemistry, the $OH^{\bullet}$ radical adducts are converted to hydroxy compounds, whereas in the present system, the $Pyr(OH)^{\bullet}$ radical can convert to dihydroxypyrene.

$Pyr(OH)^{\bullet}$, a free radical, may also react with oxygen at a diffusion-controlled rate, leading to peroxy radicals

$$Pyr(OH)^{\bullet+}\ O_2 \rightarrow Pyr(OH)OO^{\bullet} \quad (26)$$

According to the literature, further reaction could lead to the formation of hydroxypyrene through an elimination of $HO_2^{\bullet}$ or to a formation of peroxide[170]

$$Pyr(OH)OO^{\bullet} \rightarrow PyrOH + HO_2^{\bullet} \quad (27)$$

$$Pyr(OH)OO^{\bullet} \rightarrow \text{peroxide} \rightarrow \text{products} \quad (28)$$

Similar studies[167] using ionizing radiation show products that are similar to those observed in photochemistry with the additional feature that H atom products are also produced. This is similar to data on SiO_2, and a similar mechanism is needed to account for the data. In these systems, energy is deposited in the silica–alumina by ionizing radiation, leading to CT processes forming radical cations by pyrene. These species are observed by steady state diffuse reflectance and time-resolved absorption spectroscopy. Electron paramagnetic resonance measurements at low temperature also confirm the identification of this species. Pre-irradiation of silica–alumina with subsequent addition of the arene also produces the same chemical reaction as that given by the radical cation of the arene. The cationic species are extracted into solution to give final products. High-performance liquid chromatography and steady state spectroscopic studies of the products show that a major product is hydroxypyrene with a G value (molecules per 100 eV of energy absorbed) of 0.76. The reaction of the pyrene radical cation with water produces a hydroxy-addition-type free radical, which is a key intermediate in the hydrolysis process. Oxygen and ferricyanide, which are present in the extraction solution, enhance the yield of hydroxypyrene, and earlier studies have shown that this supports the proposed reaction mechanism.

Studies similar to these with pyrene have been carried out with biphenyl and its chloro derivatives.[168] Essentially, the basic details of the photochemistry of pyrene and biphenyl systems on γ-Al_2O_3 are virtually identical. Diffuse reflectance spectroscopy shows that biphenyl molecules adsorbed on activated surfaces (T_a > 350 °C) form CT complexes and eventually chemical products. The existence of the latter is also confirmed via observation of an EPR signal on photo-irradiation into the CT band of the arene/Al_2O_3 sample. Photo-irradiation of the adsorbed organic molecules leads to radical cations, and dechlorination takes place. The co-adsorption of persulfate and dinitrobenzene significantly influences the electron transfer processes. The photochemical products on both activated and nonactivated surfaces were separated by HPLC, and the collected fractions were studied spectroscopically. The important reaction of radical cations is hydrolysis resulting in hydroxybiphenyl. The radical $BP(OH)^{\bullet}$ is suggested as a key intermediate in the photohydrolysis reaction.

Chlorobiphenyls exhibit dechlorination on irradiation on γ-Al_2O_3. The reactions of 4-chlorobiphenyl (CBP) and 4,4′-dichlorobiphenyl (DCBP) on surfaces can be divided into two types, namely, oxidation, degradation, and dechlorination. The former is similar to the reaction pattern for non-chlorosubstituted BP, resulting in chlorosubstituted hydroxybiphenyls.

The biphenyl (BP) formed in the product mixture of CBP is ascribed to photoinduced dechlorination. Homolysis of chlorinated biphenyls is well-documented.[177,178] Dechlorination can result from direct chlorine–carbon bond breakage or via a reduction process.

$$C_6H_5C_6H_4Cl \xrightarrow{h\nu/\text{surface}} C_6H_5C_6H_5Cl^{-} \quad (29)$$

Reductants such as dienes and amines are commonly used in photochemistry[179–181] to promote reduction.

CBP on surfaces may be reduced by intermediate $CBP(OH)^{\bullet}$ radicals, which are weak reductants, subsequently leading to dechlorination. However, this is contrary to the fact that the presence of CCl_4 (10^{-3} mol dm^{-3}) does not depress the yield of BP. If $CBP(OH)^{\bullet}$ reduces CBP to form the chlorine anion and BP, then CCl_4 should effectively compete with CBP because of its higher degree of chlorination. It is possible that in the present system the formation of chlorine ion is through bond cleavage, as the photon energy is comparable with the (Ph)C–Cl bonding energy, ~94.5 kcal mol^{-1}.[182,183] The photochemical reactions of DCBP are similar to those of CBP. Model systems of possible interest to environmental studies

have also been reported. It is found[184,185] that radiolysis of hexachlorobenzene on Al_2O_3 give rise to penta- and tetrachlorobenzene, presumably by electron attachment to remove the chlorine as Cl^-.

5.9. Summary

Compared to silica, γ-Al_2O_3 exhibits a vivid chemistry of ionic processes, which are associated with Lewis and Brønsted acid sites on the heated alumina surface. Surface features already observed in SiO_2 also appear, and again those events are reminiscent of solution chemistry. Both high-surface silica and alumina occur as small nanosized particles, and as the porosity of the material is minimal, little geometric size effects of this material on chemical reactions are observed. On the other hand, zeolites, and to some extent clays, which contain the elements of SiO_2 and Al_2O_3, exhibit marked geometric effects of reactions occurring in them. Zeolites and clays are also very ionic with a high percentage of exchangeable cations. The cations enter into additional reactions that are not observed on the two former oxides. It is a logical step to pursue chemistry similar to that reported in SiO_2 and γ-alumina, but now with zeolites and clays.

6. Zeolites

Silica and alumina may be cosynthesized into a class of materials called zeolites, consisting of $(SiO_4)^{4-}$ and $(AlO_4)^{5-}$ tetrahedra, with an empirical formula of

$$M_xAl_ySi_zO_u$$

Typical examples are zeolite Y, $M_{55}-Al_{55}-Si_{137}-O_{384}$, and zeolite X, $M_{80}Al_{80}Si_{112}O_{384}$. Negative charges on the zeolite framework are generated by the difference in charge between $[SiO_4]^{4-}$ and $(AlO_4)^{5-}$ tetrahedra, which are balanced by charge-compensating atoms. These materials are microporous and are well represented by Figure 18 where the buildup of a zeolite from the unit cage structure is shown, and Figure 19, which shows the connecting nature of the porous structure. Figures 19 and 20 show the probable locations of metal ions. An excellent review of structure, etc., is given in ref 186, and concepts of use are given in refs 187 and 188.

6.1. Structure

Figure 18 shows a schematic drawing of the zeolite framework structures together with the possible cation sites. The building block of zeolites A, X, and Y is the sodalite cage, pictured as one of the small cages in Figure 18. The sodalite cage has a structure of a truncated octahedral with Si^{4+} and Al^{3+} at the tetrahedral sites and possesses eight hexagonal windows and six square windows. Zeolite A (Si/Al ratio = 1.0), a synthetic material with no natural counterpart, is a simple cubic array of sodalite cages connected by the square double-four-membered rings (D4R) of SiO_4^{4-} and AlO_4^{5-}. There are three different types of cages in zeolite A, that is, D4R, sodalite cage, and α-cage. The cation locations are found to be on

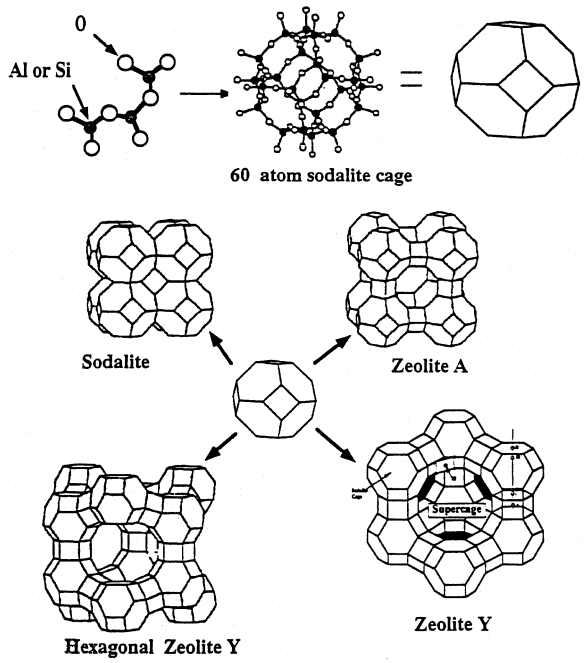

Figure 18. Illustration of zeolite composition and sequential construction utilizing the 60-atom sodalite to form clusters of cages in different ways, thus giving the indicated zeolite structures. Reprinted with permission from Stucky, G. *Naval Res. Rev.* **1991**, *18*, 28. Copyright 1991 U.S. Government Printing Office.

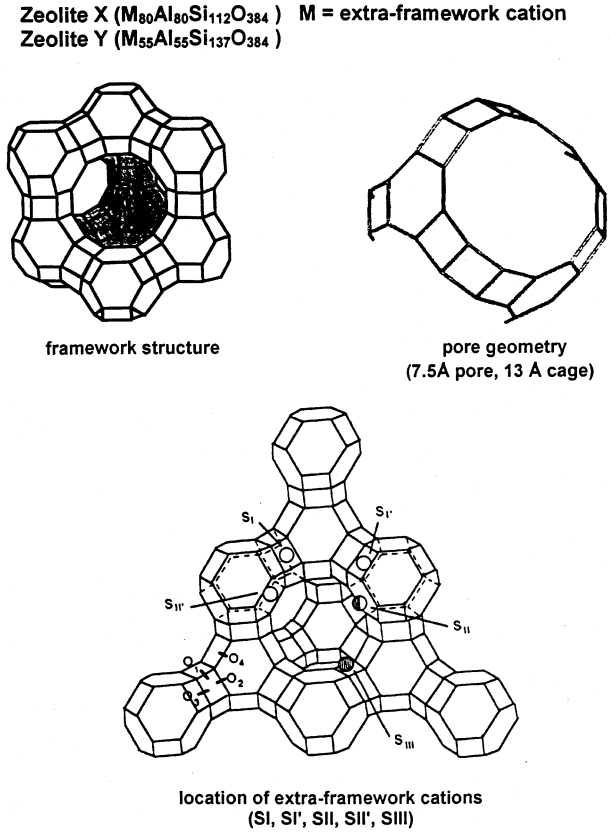

Figure 19. Section of perodic 3D lattice in zeolite Y.

site A in the center of the six-membered ring of sodalite cage and site E on the window of the eight-membered ring. Zk-4 is also a synthetic zeolite formed in the presence of tetramethylammonium ion and is isostructural to zeolite A but of higher frame-

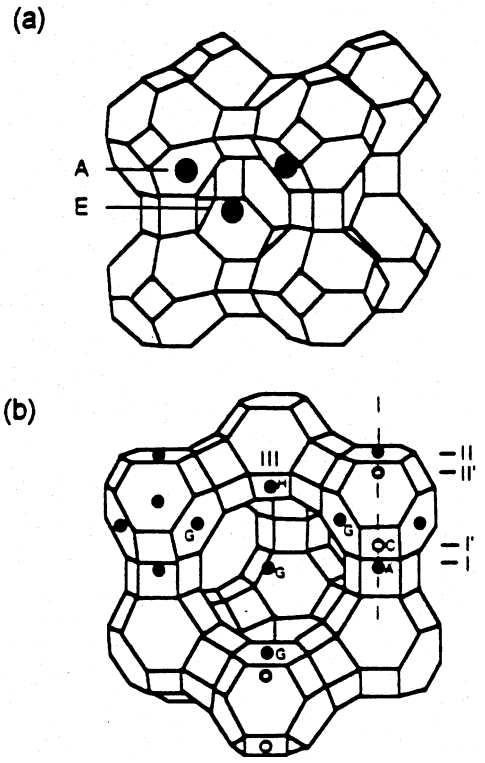

Figure 20. Structures of zeolites used with possible cation locations indicated for each zeolite: (a) zeolite A; (b) zeolites X and Y.

work Si/Al ratio. Both zeolites X and Y, having different framework Si/Al ratios (>1.5 for zeolite Y and <1.5 for zeolite X), are isostructural to the natural mineral faujasite. The structure is essentially a diamond lattice of sodalite cages connected via the double-six-membered rings (D6R) of SiO_4^{4-} and AI O_4^{5-}. By this connection, three cages are present (Figure 19): D6R, sodalite cage, and supercage. Alkali cations, which compensate the negative charges of the framework due to isomorphous substitution of Si by Al, are distributed among at least four kinds of sites (Figure 20): site I in the center of the D6R cage, site I′ inside the sodalite cage, site II on the wall of the supercage, and site III above the four-membered ring in the supercage. The occupation of the cation sites depends on the nature of the cations and on the conditions under which the samples are treated. In dehydrated zeolites X and Y, each sodalite cage contains four Na^+ ions in the type I′ sites, and each supercage also contains Na^+ in the type II sites. Foreign cations present in NaY occupy preferentially the cation sites; for example, Cu^{2+} and Cd^{2+} prefer site I′, whereas Tl^+ prefers site III. On complete hydration, water molecules fill the spaces of the cages. Generally, on average a total of ~4 water molecules are in the sodalite cage, ~24 in the *x*-cage of NaA, and 34−37 in the supercage of NaY and NaX. The water molecules are randomly located in the supercage of NaX and NaY but structured (pentagonal dodecahedron) in the *x*-cage of NaA.

Numerous zeolites have been synthesized, but for brevity only zeolites X and Y will be considered in detail, with some studies with the channel zeolite ZSM-5.

It is pertinent to note recent reviews in this area: refs 189 and 190 in synthesis, ref 191 in cationic reactions in zeolite, and ref 192, a recent review of selected photoprocesses in zeolites.

6.2. Adsorption and Adsorpton Sites

6.2.1. Metal Ions

Metal ions, M^+, are electrostatically adsorbed onto zeolites to maintain charge neutrality. For example, zeolite samples where the counterion is almost entirely Na^+ or K^+ can be prepared, and by simple ion exchange in water other cations may replace those already in the zeolite. With large organic cations, size can be the controlling factor in allowing the cation to progress into the channels and cages and, finally, through a zeolite crystal. Adsorption to the surface can occur regardless of size, but it is chemistry in the cages or channels that is sought after. Water also adsorbs readily into the zeolite and partially hydrates the cations M^+. More will be discussed on this later. The cation M^+ may be replaced by H^+, giving rise to an acidic zeolite. These latter materials are potent thermal catalysts and difficult to use in photochemistry.

6.2.2. Neutral Organic Molecules

Most neutral organic molecules adsorb to zeolites, typically in the supercages, or large channels of channel zeolites. In the case of arenes, the adsorption is very strong, whereas it is much weaker with alkanes. Dowsing the zeolite in typical solvents, water, methanol, cyclohexane, etc., followed by a partial drying, leads to a zeolite having cages filled with solvent. The loading is that expected from the physical properties of the solvent, that is, density and molecular weight. Typically, 5−6 cyclohexane molecules and ~25 methanol molecules can be incorporated into the supercage of ZY. Water is unique as it can also adsorb into the small side cages. Typically, 4 water molecules can adsorb in the small cage and ~40 in the supercage.

6.3. Sample Preparation

Polar organic cations, for example, methylviologen, MV^{2+}, can be exchanged onto a zeolite using water as a vehicle. Noncharged molecules, pyrene, anthracene, etc., are conveniently adsorbed from a low molecular weight alkane such as pentane or hexane. Subsequently, solvents are removed in a vacuum (<1 mTorr) at ~100 °C for 20 min. Even with hexanes, the author has found that pumping at room temperature is not sufficient to remove the solvent, and elevated temperatures are needed. An alternative study[287] indicates that water may be removed at room temperature by extended pumping at high vacuum. It is necessary, even with "dry" stored samples, to repump the sample at 100 °C just prior to study and to keep it under vacuum. Very short exposures of a dry zeolite sample to wet air (relative humidity ≥ 40%) can lead to a complete filling of the small channels with 4 water molecules. With longer exposures subsequent water molecules adsorb in the supercage.

Samples can be loaded also from solute vapor, a means of bypassing extraneous solvent, but this is a more tedious preparation.

6.4. Nature of Absorption Sites

Cations adsorb at positions of high electron density, namely, oxygen atoms of the framework. Water tends to cluster around the metal cations and onto other polar sites. Other sites, Lewis acid (LA), Lewis base (LB), and Brønsted acid (BA) can also lead to adsorption of organic molecules. The diagram below illustrates these centers of adsorption.

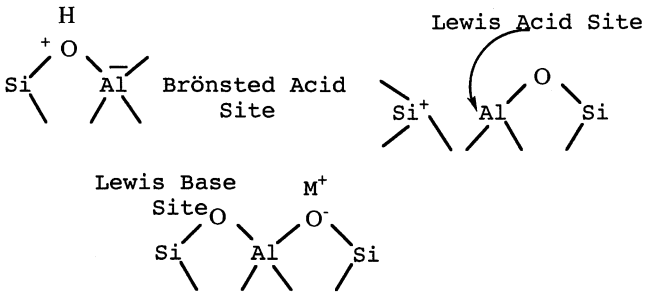

The Lewis acid site tends to accept electrons, whereas the Lewis base site tends to donate electrons, and the strength of the electron acceptor increases with increasing Si/Al ratios and with small compared to large exchange cations. The opposite is true for the electron-donating properties of the base site. The acidity of a zeolite is evident in the photochemistry of adsorbed similar ketones. This will be dealt with later.

The above experimental findings have been successfully understood in terms of the Sanderson electronegativity of zeolites (S_z), which is defined by the following Sanderson's equation.[193] The acidity of a zeolite is evident in the photochemistry of adsorbed similar ketones. This will be dealt with later.

$$S_z = (\mathrm{M}^x\mathrm{Al}^x\mathrm{Si}^{192-x}\mathrm{O}^{384})^{\mathrm{I}/[x+(192-x)+384]}$$

M, Al, Si, and O are the atomic electronegativities for alkali cation, aluminum, silicon, and oxygen, respectively, and x is the number of aluminum atoms per unit cell. The values of S_z calculated for zeolite samples are also given in Table 14. It is seen that

Table 14. Chemical Composition and Sanderson Electronegativity (S_2) of the Zeolites Used in This Study, Together with the Partial Charge on the Framework Oxygen (δ_O)[a]

sample	composition	S_2	δ_O
zeolite X	$LI_{46}Na_{34}Al_{80}Si_{112}O_{384}$	2.45	−0.40
	$K_{78}Na_4Al_{80}Si_{112}O_{384}$	2.36	−0.43
	$Rb_{58}Na_{22}Al_{80}Si_{112}O_{384}$	2.40	−0.45
	$Cs_{50}Na_{30}Al_{80}Si_{112}O_{384}$	2.25	−0.47
zeolite Y	$Li_{27}Na_{28}Al_{55}Si_{137}O_{384}$	2.60	−0.35
	$K_{50}Na_5Al_{55}Si_{137}O_{384}$	2.54	−0.37
	$Rb_{37}Na_{18}Al_{55}Si_{137}O_{384}$	2.50	−0.39
	$Cs_{32}Na_{23}Al_{55}Si_{137}O_{384}$	2.45	−0.40

[a] Data taken from ref 198.

the ability of zeolites to stabilize an unpaired electron (electronegativity) decreases in the sequence Li > Na > K > Rb > Cs and that for zeolites with the same exchange cation decreases in the order Y > X > A ≈ sodalite. The overall electron-accepting ability of the zeolites governs the electron trapping by the cations.

Another factor that has to be considered is the LA character of the sodium four cluster Na_4^{4+} in the small cage, which has a strong electron affinity.

Zeolites are powerful absorbers of many materials, which include those of interest in photochemistry. Small cations, for example, Na^+ and K^+, may be contained in the small side cage, whereas larger cations, for example, MV^{2+}, and neutral molecules are contained in the supercage. Water-soluble materials may be removed from the zeolite by an aqueous wash, whereas most neutral organics, for example, anthracene and naphthalene, are removed by washing the samples with methanol. Common solvents are removed under vacuum at 100 °C.

6.5. Nature of Zeolite Supercage Surface

We can say immediately that the supercages of zeolites containing metal ions are very polar. The Sanderson equation gives an increase of the relative degree of polarity in terms of an electronegativity. As in the case of earlier micellar work,[194] it is necessary to estimate how a guest molecule responds to the unique environment of the zeolite. Turning this around, it may be asked what an absorbed molecule can indicate of the nature of the zeolite surface. This approach has been dealt with previously in SiO_2, and γ-Al_2O_3 systems.

The questions posed could be the following:

(a) What is the nature of the surface, polarity, etc?

(b) How do guest molecules move in zeolite?

(c) How do co-adsorbed molecules, namely, solvents, affect (a) and (b)?

6.6. Surface Properties

Probing the zeolite surface is conveniently carried out with pyrene, where, as indicated previously, the fluorescence fine structure comments on the surroundings of pyrene.

Many studies of pyrene in zeolites have been reported.[195−200] In the fluorescence spectrum of pyrene in Figure 21,[199] only two peaks at 371 and 392 nm are clearly observed compared to the five seen in the solution phase. The quantum yield of fluorescence of pyrene on a zeolite is lower than that for pyrene on SiO_2 and in solution. The major difference on a zeolite compared to SiO_2 or solution is the broadness of the spectrum, which tends to obscure the fine structure. It is seen that water increases the number of fine structure peaks that are observed, the number of peaks seen clearly now being four. Methanol and other solvents cause a similar effect, but alkanes have no effect on the fine structure. It is pertinent to note that the spectral position also shows a red shift with increasing water, and this bathochromic shift, which correlates with the polarity experienced by the probe molecule, has been recorded previously for several systems.[201] This measurement is particularly useful in the case of molecules that do not show any marked

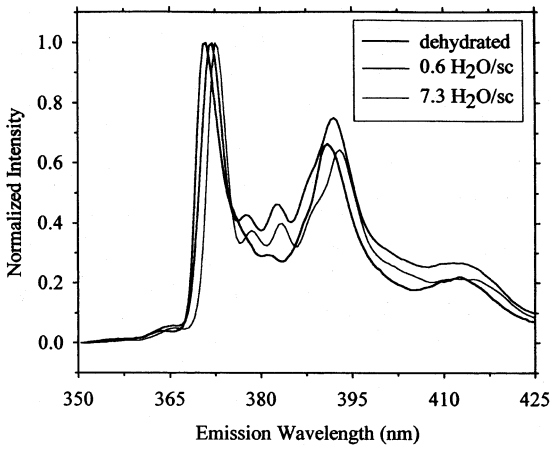

Figure 21. Effect of water on the fluorescence spectrum of pyrene in zeolite KY. The influence of H_2O can be reversed in KY by heating at 80 °C and evacuation at mTorr pressures for 15−30 min. Reprinted with permission from ref 199. Copyright 1999 American Chemical Society.

fluorescence fine structure change with changing environment, for example, anthracene and naphthalene. In zeolites the low incidence of the fluorescence III peak with respect to I is indicative of a very polar environment for the probe molecule and is not an unexpected conclusion. However, this measurement shows that the environment of the probe pyrene in zeolite Y is less polar than that in zeolite X.

Higher loadings of pyrene in zeolites tend to form pyrene excimers. This process is dynamic as shown by picosecond studies[202] at 30 °C and by slower nanosecond studies at 77 K. However, only a portion of the excimer grows at low temperature, and when excimers are formed, there is a significant red shift in the absorption spectrum of pyrene.[196,197] This feature indicates that ground state dimers of pyrene are present. The dimers are removed along with their characteristic spectrum on the introduction of water or pentane to the system.

This phenomenon indicates that the residual solvent molecules in the zeolites are located in such a way so as to prevent the interactions of excited pyrene monomer (^{1}Py*) with the ground state pyrene to form excimers and that, after removal of the solvent molecules, the pyrene molecules responsible for the excimers once again interact in the zeolite cavities. For the excimers so formed, time-resolved emission measurements of the sample, monitored at a wavelength of 460 nm, show that the time required for the formation of pyrene excimers is <0.1 ns at 20 °C. Steady state excitation measurements monitored at the same wavelength show that the pyrene molecules in the excimers are present in the form of monomers in the ground state. This differs from that observed for samples with higher pyrene loadings, where excimers are present in the form of ground state "dimers".

Effects of solvent molecules on the distribution of pyrene molecules are further examined by studies of adsorption of *n*-pentane into the Py-zeolite Y(0.05 Py/uc), which was evacuated to 2×10^{-3} Torr prior to adsorption of the solvent. As *n*-pentane molecules are adsorbed by the zeolite, the intensity of the pyrene excimer emission decreases, with an increase in intensity of the ^{1}Py* emission. This spectral change (at a 52 Torr vapor pressure of *n*-pentane) takes 40 min and is indicative of the restriction placed by pentane on the movement of molecules in the zeolite. Evacuation of the sample at 10^{-3} Torr reinstates the emission intensities of pyrene excimer and monomer, the process taking ~1 day. The experiments clearly demonstrate that residual solvent molecules play an important role in preventing excimer formation and that some pyrene molecules (those forming excimers) are located in close proximity in the same supercage. Furthermore, the results indicate that separation of the aggregated pyrene molecules (forming excimers) in the supercages of zeolite Y, which is forced by the co-adsorbed solvent molecules, returns to its original condition following removal of solvent. The distribution and inhomogeneity of the pyrene molecules in the zeolite is determined by the characteristics of the pyrene adsorption to the surface of the zeolite. These data also stress the point already raised in sample preparation where low presures and elevated temperatures are needed to remove adsorbed solvent from zeolites.

6.7. Diffusion

Several measurements of the rate of movement or diffusion of reactants in zeolites are available.[199,203−205] Due to the slow diffusion of most solutes in zeolites the rates of solute movement are measured over the millisecond time region and have to utilize the quenching of long-lived triplet states.

Triplet excited states of pyrene, phenanthrene, and naphthalene have been generated in zeolite KY by pulsed laser excitation, and the influence of co-adsorbed water on quenching of these triplet states by ferrocene and the immobile ferrocene derivative ferrocenyl-methyltrimethylammonium cation (FcMN) has been studied by transient absorption spectroscopy.[199] To make these measurements, the probe loadings in KY were deliberately kept low, such that quenching involves migration of molecules from one supercage to another. In all cases, maxima in bimolecular triplet quenching rates versus the number of H_2O per supercage (N_{sc}) were observed at $N_{sc} \approx 4$, a value that coincides with the number of H_2O molecules that fill the sodalite cages. For pyrene quenching by FcMN, the effect of 4 H_2O/sc was particularly dramatic, where the quenching rate increased by 3 orders of magnitude relative to dehydrated KY. Above $N_{sc} = 4$, further additions of H_2O lowered the rate of quenching. Similar effects of water have been published in other studies.[206] Typical data[199] are shown in Figure 22, where a dramatic influence of the first four water molecules on the quenching rate is shown. The rate constants extracted from these data and with 4 H_2O/sc are shown in Figure 22. It is concluded that the "magic" number of 4 H_2O/sc "corresponds" to the adsorption of these water molecules into the side cage containing the 4 Na^+ ions.[207] The arenes in the supercage are suggested to adsorb to the wall of this site, whereas the interaction of the arene with the site is weakened by the H_2O molecules, thus leading to more rapid diffusion. This does not completely preclude adsorption of the arene to

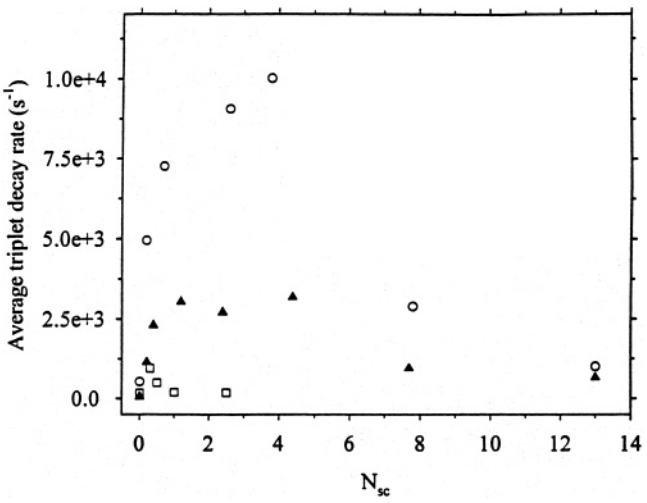

Figure 22. Influence of added solvent H_2O or C_6H_{12} on the average decay rate of ^3Py or $^3PBN^+$ in KY containing 1 mM ferrocene, $O^3Py(H_2O)$: (△) $^3PN^+(H_2O)$; (□) $PN^+(C_6H_{12})$. Reprinted with permission from ref 199. Copyright 1999 American Chemical Society.

another site on the supercage, where again adsorbed water reduces the interaction of the arene and this site. The rate of triplet quenching by FcMN, where quenching results from motion of the aromatic probes in their triplet state to FcMN, generally followed the trend $^3Np^* > {}^3Ph^* \gg {}^3Py^*$. This trend, as well as the influence of co-adsorbed H_2O on quenching, has been explained by the effects of adsorption and molecular size on the diffusion of these molecules in KY.

The rate constants may be used to calculate the diffusion constants of the arenes in the zeolite. The values obtained are in agreement with those obtained by more conventional methods, for small molecules (Table 15).

Table 15. Rate of Diffusion of Selected Solutes in KY at 20 °C: Effect of Coadsorbed Water

	diffusion constant ($cm^2\ s^{-1}$)		
solute	dehydrated	$4H_2O$/SC	$13H_2O$/SC
pyrene	10^{-13}	2×10^{-10}	6×10^{-11}
phenanthrene	10^{-10}	6×10^{-9}	2×10^{-9}
naphthalene	10^{-9}	3×10^{-9}	10^{-9}
ferrocene	5×10^{-10}	10^{-8}	10^{-9}

time to diffuse from one cage to the next one	
D (cm^2/s)	t (s)
3×10^{-7}	10^{-8}

Detailed treatment[204,205,208] of the diffusion of the arenes in the zeolite has been put forward and also extract diffusion constants of the same magnitude of those found above, that is, 10^{-15}–10^{-16} m^2/s at room temperature. The transfer of triplet energy from excited to arenes to Tl^{3+} had been reported in zeolite Y.[203] It is suggested that the energy transfer takes place from reactants in neighboring zeolite cages.

There are reports of radical reactions in zeolites that require radical migration. For diphenylmethyl radicals,[208] a prominent pathway for decay of these radicals is geminate in nature. The decay of benzyl radicals has been studied in zeolites.[209] For ZY the rate of decay decreases in the order of the exchanged Cm, Li^+, Na^+, K^+, Rb^+, Cs^+. It is suggested that this is due to the mobility of the radical, which decreases along this series of metal ions.

6.8. Mobility in the Supercage

There are two reports of limited mobility of a molecule in a zeolite supercage,[210,211] both utilizing the rate of isomerization of *trans*-stilbene. This rate is rapid (picoseconds) in solution, and short pulsed methods have to be used. In one paper,[210] a diconvolution method with nanosecond light flashes gave a rate of isomerization that was similar to that in viscous solvents. However, a direct picosecond study indicated a more rapid isomerization in the Na^+ form of zeolite Y, which varied with included solvent.[211] These data are summarized in Table 16.

Table 16. Fluorescence Lifetime of *trans*-Stilbene in Hydrocarbon Solvents and in Zeolites[a]

medium	fluorescence lifetime (ps)
hexane	66 (70) ± 8
methylcyclohexane	62
hexadecane	127 (157)
glycerin	580
ZSM-5	590
XSM-5 (77K)	1.5 ns
NaY (5 mM *trans*-Stilbene)	
solvent-free	52
$4H_2O$/SC	53
$13H_2O$/SC	22
H_2O bath	210, 195
1 cyclohexane/SC	71
2.5 cyclohexane/SC	105
cyclohexane bath	275, 258
solvent-free (77 K)	1.4 ns
NaY (100 mM *trans*-Stilbene)	
solvent-free	28
2.5 cyclohexane/SC	54
cyclohexane bath	165
KY (5 mM *trans*-Stilbene)	
solvent-free	54
$4H_2O$/SC	47
$13H_2O$/SC	30

[a] Data taken from ref 211. [b] Predetermined literature values are given in parentheses. The *trans*-stilbene concentration in ZSM-5 was 10 mM. [c] Values determined by nonlinear least-squares fitting to a single-exponential minimizing X^2.

Adding even small amounts of (1/sc) cyclohexane to NaY increases the lifetime of the *trans*-stilbene fluorescence τ_{fTS}, that is, restricts its mobility. On the other hand, small amounts of H_2O lower τ_{fTS} to the lowest value observed in all systems. Other studies have shown that small amounts of H_2O added to these zeolites increase the diffusion of aromatic species included in them, presumably by weakening the π electron–cation interaction.[199,211] Thus, the decrease in τ_{fTS} could result from the combination of the high polarity of the zeolite medium favoring a polar transition state along with the effect of water on the absorption site. At these low water contents, it cannot be strictly stated that the small decreases in τ_{fTS} are from an increase in mobility, because the effect that H_2O has on the polarity of the *trans*-stilbene microenvironment is unknown.

Bathing the sample in H_2O appears to restrict motion. It has been shown that certain nonpolar molecules such as anthracene migrate to the exterior surface of the zeolite particles when H_2O is included in the zeolite.[212] However, this was observed only at certain loadings of H_2O much higher than used here but lower than the maximum loading attainable by bathing the sample in H_2O. It seems unlikely that molecules such as *trans*-stilbene, which are essentially insoluble in H_2O, could migrate through the zeolite to the particle exterior when the zeolite voids are filled with H_2O. Thus, bathing the zeolite in H_2O should trap *trans*-stilbene in the particle interior. Given that absorption of *trans*-stilbene should be considerably weakened by the presence of H_2O, then τ_{fTS} in this sample may reflect bulk solvent properties in the zeolite. It is pertinent to note that the rapid rate of isomerization of stilbene is of the order of that reported for the rapid pyrene excimer formation in a supercage.

It can be concluded that restricted local motion of a molecule in a supercage can be rapid and <100 ps. On the other hand, longer range motion, that is, cage to cage, is slower, taking micro- to milliseconds. In both cases solvents play an important role in redefining this kinetic motion.

The slower cage-to-cage diffusion of reaction(s) in a zeolite is modum operandis of many photochemical reactions in these systems. The quenching of arene of luminesence in zeolites illustrates the point.

6.9. Quenching of Arene Fluorescence by Mobile Reactants

In these studies it is pertinent to note that the lifetime of the fluorescence that is quenched is itself a function of the zeolite, that is, metal counterion, and the Sanderson potential.

6.10. Lifetime Measurements

Many arenes, including pyrene, exhibit shortened fluorescence lifetimes in zeolites.[198] Figure 23 shows the decay of excited pyrene in zeolite X with Li^+, K^+, Rb^+, and Cs^+ counterions. The fluorescence decay rate decreases with the order of the above cations. The decays are fitted with the Gaussian relationship used earlier in the SiO_2 system, giving here the following half-lifetimes for the fluorescence: Li^+ (86 ns), K^+ (44 ns), Rb^+ (9.4 ns), and Cs^+ (2.5 ns). Similar effects are observed in zeolite Y. The decrease in the fluorescence lifetimes corresponds to a decrease in the fluorescence quantum yields (Table 17). The shortening of the fluorescence lifetime can be understood via the heavy atom effect on increasing the intersystem coming to the triplet state via spin−orbit coupling, an effect also suggested in other studies.[213,214] The decrease in the fluorescence lifetimes also correlates with the decrease in the Sanderson electronegativity S_2 in these samples and with the partial charge on the framework oxygen cation δ_O.

This is defined as

$$\delta_O = (S_z - S_0)/157S_0^{1/2}$$

This suggests that the photochemistry of arenes in zeolites may be interpreted in terms of data from the solution phase. However, if a zeolite is looked upon as a "solvent" for the arenes, then conventional zeolite thinking, via acid sites etc., may provide a better concept for interpreting the data. The arenes may form partial charge transfer states with zeolite framework, which would correlate well with the charge on the framework. In fact, the fluorescence lifetime of most arenes is independent of temperature from about 300 to 77 K. This is quite unlike the behavior reported for these arenes in more conventional systems, for example, polymer film,[57,58] where the interaction of the arene and the host is weak. A strong CT interaction of the arene with the zeolite will depend on the electronegativity of the zeolite, or charge on the framework,[215] and, unlike conventional photochemistry, would probably exhibit no temperature dependence. More work is needed in this area.

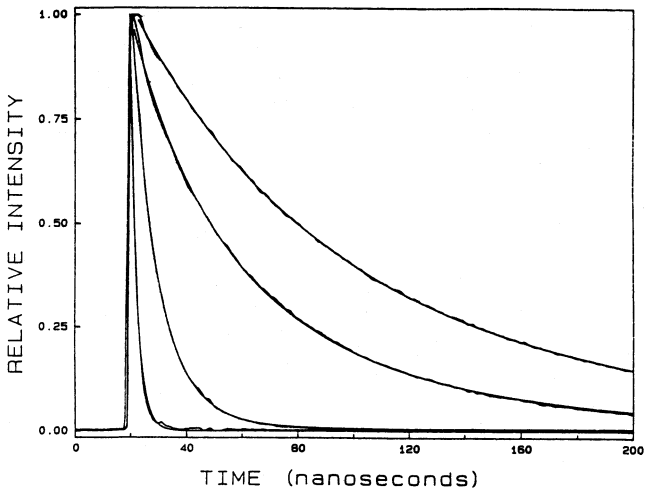

Figure 23. Time-resolved emission decay of pyrene in Li^+, K^+, Rb^+, and Cs^+ zeolites X (from slow to fast decay) monitored at 400 nm. The smooth lines are curve-fitted lines using the Gaussian distribution model. The zeolites were preactivated at 550 °C for 8 h. The pyrene loading was 2.8×10^{-4} mol/g. Reprinted with permission from ref 198. Copyright 1994 American Chemical Society.

Table 17. Quantum Yields (Reference 198) of the Observed Species in Zeolites; Fluorescence Lifetimes, T (ns)[a]

sample	^{1}Py*	τ	^{3}Py	Py^+	$Py^{\bullet-}$
$Li_{46}X$	0.61		0.0093	0.0096	0.0035
$K_{76}X$	0.41		0.0082	0.0088	0.0053
$Rb_{58}X$	0.11		0.0093	0.0088	0.0058
$Cs_{50}X$	*b*		0.0147	0.0094	0.0068
$Li_{27}Y$	0.40	60.2	0.0038	0.0048	0.0018
$K_{50}Y$	0.11	30.8	0.0034	0.0048	0.0032
$Rb_{37}Y$	0.07	6.7	0.0046	0.0049	0.0037
$Cs_{32}Y$		1.75	0.0126	0.0055	0.0042
NaY		40.6	0.00	0.00	0.00

[a] Data taken from ref 198.

6.10.1. O_2 Quenching

The literature contains much information on the quenching of pyrene excited states by a variety of quenchers. Studies to this effect have already been discussed for pyrene on SiO_2. Similar data are obtained for the quenching of pyrene fluorescence by O_2 in zeolites.[215] As in SiO_2 the suggested mechanism

is a mixture of Langmuir−Hinshelwood and Eley−Rideal quenching. This is concluded[216] as the rate of O_2 quenching increases with decreasing temperatures, thus highlighting the role of adsorbed O_2 and the LH mechanism. O_2 quenching of the pyrene excited state is very efficient in all cases and follows Stern−Volmer kinetics. The O_2 quenching rate constants for excited pyrene monomers [$(1.97 \pm 0.06) \times 10^{11}$, $(2.43 \pm 0.10) \times 10^{11}$, and $(2.24 \pm 0.10) \times 10^{11}$ $M^{-1}s^{-1}$ for zeolites A, X, and Y, respectively] are obtained from the quenching kinetics for pyrene−zeolites by assuming a concentration of O_2 in the zeolite similar to that in the gas phase.[215]

The rate constants for the reaction of the excited state with O_2, shown in Table 18, exhibit a marked effect of pyrene loading, higher loading blocking the diffusion of O_2 to the excited pyrene.[196] This blocking effect is shown quite clearly in Figure 24, where increasing water adsorption completely blocks the O_2 quenching. This is also seen with other solvents, and it is probably safe to say that all solvents, when adsorbed in zeolites, will significantly decrease the diffuse of co-adsorbed solvents.

Table 18. Biomolecular Rate Constants for the O_2 Quenching of Excited Pyrene Monomer and Dimer[a]

zeolite	concn of pyrene (10^6 mol/g)	k_q [b] (10^{-11} M^{-1} s^{-1})
A[c]	0.5	1.97 ± 0.06
X[c]	1.5	2.43 ± 0.10
Y[c]	1.5	2.24 ± 0.10
X[d]	180	0.37 ± 0.04
X[e]	180	0.22 ± 0.02

[a] Data taken from refs 196 and 215. [b] The experiments were done at room temperature (22 ± 1 °C), assuming the O_2 concentrations in zeolites are the same as in the gas phase. [c] O_2 quenching of excited pyrene monomer. The pyrene concentrations in these cases were low enough to preclude the formation of dimer. [d] O_2 quenching of excited pyrene monomer. [e] O_2 quenching of excited pyrene dimer.

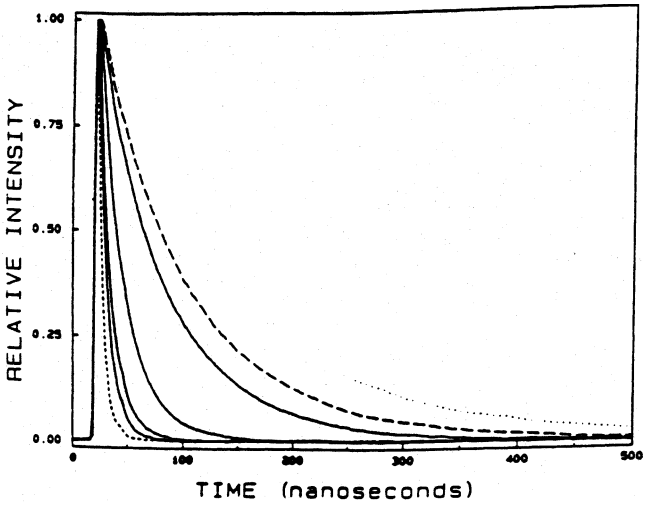

Figure 24. Effect of co-adsorbed water in pyrene-impregnated zeolite X on the time-resolved pyrene fluorescence monitored at 400 nm: (···) fully hydrated sample; (- - -) dehydrated sample at 15.2 Torr of oxygen; (− − −) dehydrated sample under vacuum (10^{-3} Torr). The four solid lines represent the fastest decay at 1.7, 2.7, 4, and 5.3% co-adsorbed water by weight. The oxygen pressure was 15.5 ± 0.3 Torr for the partially hydrated samples. Reprinted with permission from ref 215. Copyright 1989 American Chemical Society.

6.10.2. Dimethylaniline

DMA efficiently quenches the excited singlet states of pyrene[217] and anthracene.[218] For DMA a rate constant of 3×10^9 L M^{-1} s^{-1} is obtained via fitting of the experimental data with a Gaussian distribution. This indicates rapid movement of DMA in the zeolite structure. Lowering the temperature or inclusion of hexane markedly decreases the rate of the reaction data, which supports the concept of DMA diffusion in the zeolite. At higher concentrations the situation is more complex and will be discussed subsequently. The net result of the reaction is the pyrene radical anion, $P^{\bullet-}$, and the DMA radical cation, $DMA^{\bullet+}$.

6.10.3. Immobile Quenchers, Cu^{2+}, Tl^{+}, Etc.

Metal cations are bound tightly in zeolites and should exhibit little diffusion in the nanosecond to microsecond time scale. Yet the metal ions Cu^{2+} and Tl^{+}, etc., efficiently quench pyrene fluorescence. It is noted that water has only a small effect on the reaction rates, which suggests that the reaction does not involve movement of the reactants in the zeolite.[196] A similar static quenching of pyrene fluorescence is also observed for perylene, where the mechanism of energy transfer (giving excited perylene and its fluorescence) is also observed. Here, the mechanism of energy transfer is attributed to a Förster-like mechanism. The perylene quenching of ^{1}pyrene* in zeolite X follows a Förster dipole−dipole interaction mechanism with critical transfer distances of 38.9 ± 3.0 Å for hydrated samples and 37.6 ± 1.4 Å for dehydrated samples.

For zeolite X, co-adsorbed water drastically decreases the oxygen-quenching efficiency but enhances the Tl^{+} quenching of pyrene fluorescence. On the other hand, co-adsorbed water does not affect the energy transfer quenching between ^{1}pyrene* and perylene. In both hydrated and dehydrated zeolite X samples, Tl^{+} quenches ^{1}pyrene* via an electron-tunneling mechanism. The active radii for the hydrated and dehydrated zeolite X samples are calculated to be 16.0 ± 1.6 and 11.1 ± 1.0 Å, respectively.

With zeolite A, co-adsorbed water does not block oxygen quenching of ^{1}pyrene*, which requires close contact of reactants. In addition, Tl^{+} ions do not quench singlet excited pyrene in zeolite A under any of the conditions stated above. In this zeolite, pyrene is adsorbed at the surface of zeolite A, giving ready access to oxygen, whereas Tl^{+} ions are adsorbed in the zeolite pores at some distance from pyrene.

6.10.4. Diffusion and Rapid Quenching

As indicated earlier, higher loadings of quencher markedly alter the nature and rates of the quenching kinetics. Prime examples are given in refs 218−221. The following consideration brings this into focus. At low solute loading, both probe and quencher are located in different supercages, and movement or "special" kinetics is required for reaction to occur. At higher loadings there is an increased probability that

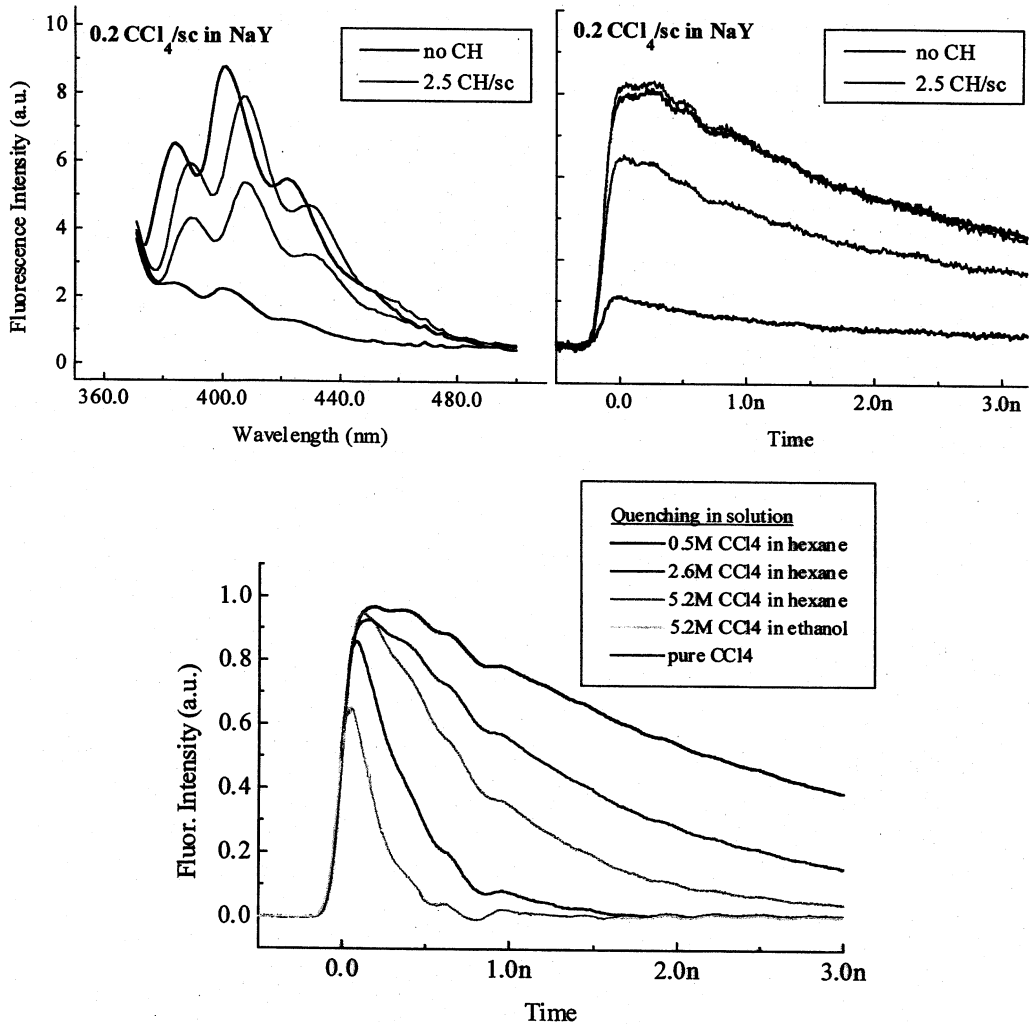

Figure 25. Quenching of anthracene fluorescence by CCl_4 in sodium Y. Reprinted with permission from ref 218. Copyright 2001 Elsevier.

probe and quencher will occupy the same supercage. With random occupancy, the distribution of guest molecules in the zeolite cages should follow a Poisson arrangement, as in a micellar system.[4] The reaction of a probe and quencher in the same cage should be rapid. Studies show that double occupancy, probe and quencher in the same cage, is far more frequent than that allowed by the Poisson distribution[218,219] and that the reaction rate is much faster than that expected by prior experience in other systems. To discuss this situation it is essential to have reliable rapid quenching (picoseconds) of reactants in zeolite systems.

6.10.5. Rapid Reactions in Supercages

Rapid response[218,220] studies in the picosecond range show ultrafast photoinduced electron transfer in zeolites. Typical data are shown in Figure 25 for the quenching of anthracene fluorescence by CCl_4 in NaY. Both steady state measurements and fast spectrophotometry show at a CCl_4 loading of 0.2 CCl_4/sc that the anthracene fluorescence is promptly and markedly quenched.[220] The co-adsorption of 2.5 C_6H_{12}/sc greatly reduces this effect. In the dry zeolite the quenching is well beyond that predicted by a Poisson distribution, but C_6H_{12} brings the data in line with this distribution. The effect of CCl_4 in various solvents in quenching anthracene fluorescence is also shown. The static quenching is minimal in all but 5.2 M CCl_4 in ethanol. This is in marked contrast to the quenching in 0.2 CCl_4/Se (~0.2 M). Obviously, the zeolite introduces a new dimension to the quenching, and for the fluorescence response in the zeolite it is possible to state that the quenching occurs in <5 ps.

In the pyrene system the products of the reaction are the radical cation $Py^{\bullet+}$ and Cl^- or CCl_3^-. The $P^{\bullet+}$ species is clearly seen spectroscopically, and its decay

$$Py + CCl_4 \rightarrow Py^{\bullet+} + Cl^- + CCl_3$$
$$Py + CCl_4 \rightarrow Py^{\bullet+} + CCl_3^- + Cl$$

exhibits an initial rapid response followed by a very slow reaction. The initial rapid reaction in the microsecond region is concluded to be via reaction of $P^{\bullet+}$ with Cl^- or CCl_3^- in the supercage, where the species were originally created by the light quantum. This competes with the escape of Cl^- from the cage and retards the backreaction. The final products are those already established for this photosystem in SiO_2, that is, chloropyrenes.

Similar data were obtained for the quenching of anthracene (An) fluorescence by CH_3NO_2, NM in NaY, and 2-methyl-2-nitropropane in NaX.[218] Three forms of quenching were observed in NaY, including static quenching, dynamic quenching on time scales of <0.3 ns, and dynamic quenching on time scales of >1 ns. Static quenching of ^{1}An* by NM was extensive. For example, a 50% drop in the initial intensity of ^{1}An* decay profiles was observed at NM loadings equivalent to 0.10 M in the zeolite, or 0.13 NM/sc (where sc ≡ supercage). This level of quenching was not predicted by a random or Poisson distribution of NM among the An-occupied cages. In this case, only 13% of the An-occupied supercages should be occupied by NM at loadings of 0.13 NM/sc. To explain the enhanced static quenching, the action of conjugate acid−base sites has been invoked, whereby An adsorbs to acidic, cationic sites. This adsorption induces the co-adsorption of NM to nearby negatively charged oxygen atoms or basic sites. In NaX, ionization of NM to *aci*-NM was observed. Thus, to test quenching in NaX, the less acidic nitro compound 2M2NP was used. In NaY, static quenching of ^{1}AN* by 2M2NP was indistinguishable from quenching by NM, whereas in NaX quenching was much less extensive relative to NaY. The latter result is explained by a higher number of basic adsorption sites (or negative charges) as well as a higher degree of intrinsic basicity of adsorption sites in NaX, relative to NaY. Through competitive effects, these sites lower the extent of adsorption of 2M2NP to the An-induced basic sites. The dynamic quenching of ^{1}An* on time scales of <0.3 ns is explained by intracage diffusion of quenchers randomly loaded into An-occupied supercages. The quenching on time scales of >1 ns is explained by electron tunneling to quenchers located outside the An-occupied supercages.

Nanosecond studies of 1,4-dicyanobenzene and 4,4′-dimethoxybicumene in zeolites have also concluded that abnormally rapid reactions take place.[221]

6.11. Electron Transfer in, from, and to Zeolites

One of the earliest examples of electron transfer in a zeolite is that of electron trapping via γ-irradiation of the zeolite.[222] γ-Irradiation of the zeolite NaY produced a pink color and an EPR signal indicative of electron trapping by the Na^+ ions. The 13-line structure of the EPR signal indicated that the trapped electron is Na_4^{3+}.[223] The same species was also observed by Na vapor deposited into the zeolite.[224,225] The formation of cations of guest molecules was also shown, an important aspect of zeolite catalysis.[191] A selected example is[226] the formation of cation radicals and protonated species of *all-trans*-1,6-diphenylhexatriene, anthracene, pyrene, and perylene in the acidic zeolites H^+-ZSM-5, H^+-mordenite, and H^+-Y. These systems were studied using solid state NMR and diffuse reflectance and fluorescence spectroscopy. The two types of species form concurrently, and cation radicals are more stable than the corresponding protonated species. The Brønsted acid sites are responsible for the formation of the protonated species, and the Lewis acid sites, associated nonframework Al atoms, for the formation of cation radicals. In contrast to solutions of strong acids, the transformation of protonated species into cation radicals does not occur in zeolites, where they revert to the original neutral molecules. Exposure of the samples to laboratory air accelerates this process, and only cation radicals are subsequently observed. The stabilities of cation radicals and protonated species depend on the size of zeolite cavities and channels and on the nature of the aromatic molecules. Further reactions of cation radicals are observed in zeolites with large interstitial space. This sets the scene to expect the formation of trapped electrons, radical anions, and radical cations in the photolysis of zeolites and the photolysis of solutes in zeolites. At this stage it is important to return to the earliest work in this area,[222] or the radiolysis of zeolites.

6.12. Radiolytic Events in Zeolites

The following processes occur on subjection of zeolites to high-energy radiation.

$$z \rightarrow h^+ + e^- \text{ (ionization of zeolite framework)} \quad (30)$$

$$h^+ + e^- \rightarrow \text{recombine (electron−hole recombination)} \quad (31)$$

$$h^+ \rightarrow h^+_{trap} \text{ (hole trapping)} \quad (32)$$

$$e^- \rightarrow e^-_{trap} \text{ (electron trapping)} \quad (33)$$

$$h^+_{trap} \rightarrow e^-_{trap} \text{ (recombine) (trapped charge recombination)} \quad (34)$$

$$e^-_{trap} + Q \rightarrow Q^- \text{ (quenching of trapped electrons)} \quad (35)$$

Processes 32 and 33 can be expanded further into hole trapping and electron trapping by different species.

$$h^+ \rightarrow z^+ \text{ (hole trapping by zeolite framework)} \quad (36)$$

$$h^+ + S \rightarrow S^+ \text{ (hole scavenging)} \quad (37)$$

$$e^- + Na_n^{n+} \rightarrow Na_n^{(n-1)+} \text{ (electron trapping by cation clusters)} \quad (38)$$

$$e^- + (H_2O)_n \rightarrow (HO)^-_{2n} \text{ (formation of hydrated electrons)} \quad (39)$$

$$e^- + Q \rightarrow Q^- \text{ (electron scavenging)} \quad (40)$$

Z denotes the zeolite framework, Z^+ the trapped hole in the zeolite framework, e^- an electron in the conduction band, and e^-_{trap} the trapped electron. Na_n^{n+} is the cation cluster capable of trapping of electron and $(H_2O)_n$ the liquidlike water cluster in the zeolite cavities. S and Q are hole and electron scavengers, respectively, including foreign species

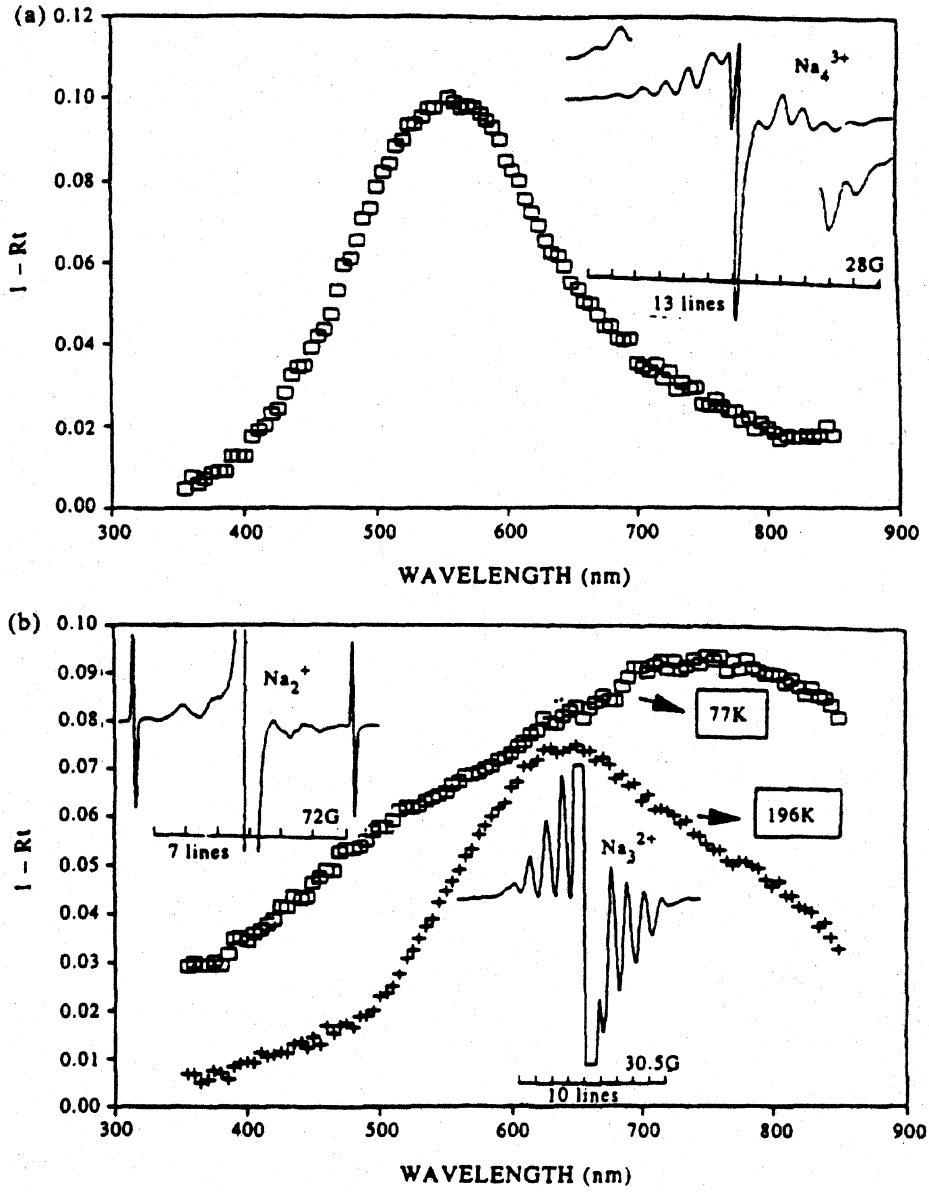

Figure 26. Spectroscopic measurement of zeolites γ-irradiated at 77 K using a combination of UV−visible absorption and ESR techniques. The corresponding ESR spectra are shown in the insets: (a) $Na_{80}X$ measured at 77 K; (b) $Na_{12}A$ measured at 77 and 196 K. Reprinted with permission from ref 231. Copyright 1998 Elsevier.

such as metal ions introduced by ion exchange, organic molecules adsorbed in the supercage, and impurities and defect sites in the zeolites.

Electrons may be injected by a variety of methods into zeolites, high-energy radiation (radiolysis), photolysis of the zeolite itself, photolysis of an incorporated molecule, or thermal methods.

Radiolysis is the present choice of electron injection as no foreign solutes are included in the zeolite.

6.12.1. Radiolysis

In radiolysis a positive hole is produced on the zeolite and an electron is ejected for subsequent capture in the zeolite. Typical optical and EPR spectra of electrons in zeolites prepared by this method are shown in Figure 26. The optical spectra exhibit broad bands, which progress to the red portion of the spectrum with smaller Na^+ clusters. The number of EPR hyperfine lines is given by $2nI + 1$, where I is the nuclear spin of the ion $I = {}^3/_2$ for ^{23}Na, ^{39}K, and ^{41}K. Therefore, Na^{3+} exhibits 13 lines; Na_3^{2+}, 10 lines; and Na^{2+}, 7 lines. Depending on the zeolite and its countercation, a whole variety of trapped electron species can be observed. Several of these species and their modes of preparation are given in Table 19. The stability of the electrons in the various clusters decreased according to Sander-

Table 19. Cation Cluster Trapped Electrons Produced in Zeolites Using Different High-Energy Excitation Sources

zeolite	γ-ray/ESR	far-UV laser photolysis	pulse radiolysis
NaSod	Na_3^{2+}	Na_4^{3+}, Na_3^{2+}	Na_4^{3+}, Na_3^{2+}
NaA	Na_3^{2+}, Na_2^+	Na_4^{3+}, Na_3^{2+}, Na_2^+	Na_4^{3+}, Na_3^{2+}, Na_2^+
NaZK-4			Na_4^{3+}, Na_3^{2+}, Na_2^+
NaX	Na_4^{3+}	Na_4^{3+}, Na_3^{2+}	Na_4^{3+}, Na_3^{2+}
NaY	Na_4^{3+}	Na_4^{3+}, Na_3^{2+}	Na_4^{3+}
KX	K_4^{3+}, K_3^{2+}	K_4^{3+}, K_3^{2+}	K_4^{3+}, K_3^{2+}
KL	K_3^{2+}	K_3^{2+}	
NaM		Na_3^{2+}, Na_2^+	

Table 20. Quantum Yields of the Observed Species[a]

sample	^{1}Py*	^{3}Py	Py$^{\bullet+}$	Py$^{\bullet-}$
Li−X	0.61	0.0093	0.0093	0.0035
K−X	0.41	0.0082	0.0088	0.0053
RB−X	0.11	0.0093	0.0088	0.0058
Cs−X	*b*	0.0147	0.0094	0.0068
Li−Y	0.40	0.0038	0.0048	0.0018
K−Y	0.11	0.0034	0.0048	0.0032
RB−Y	0.07	0.0046	0.0049	0.0037
Cs−Y	0.0126	0.0055	0.0042	

[a] Data taken from ref 198.

son potentia, that is, electrons trapped by Li^+ more stable than those trapped by Cs^+. The stability of the trapped electrons in the various zeolites decreases as Y > X > A ≈ sodalite.[226−231]

The electronic structures of these ion cluster trapped electrons are understood in a cavity model, by noting their similarity to the F centers produced in irradiated sodium halogen salt crystals. Thus far, a successful quantum mechanical description of such identities has been achieved for the Na_4^{3+} ion cluster.[232−234] The unpaired electron is treated as being "solvated" by the four Na^+ ions in a tetrahedral structure imbedded in the partially charged aluminosilicate framework of zeolites. The electron on the s-like ground state is found to be well localized within a radius of 3.4 Å around the center of the Na_4^{4+} tetrahedron. The delocalized nature of its first three p-like excited states, which are non-degenerated due to the anisotropy of the framework structure, can be seen from the electron distribution of the neighboring cages. The charges on the zeolite framework therefore exhibit a dramatic influence on the absorption spectrum of Na_4^{3+}, which is due to the s → p electronic transition. This is in exact agreement with the experimental findings that the absorption spectra of Na_4^{3+} in zeolites shift toward shorter wavelength with increasing Si/Al ratios (i.e., decreasing framework charges). The spectral shift data were also empirically understood using the Sanderson electronegativity S_z.[227,235,236] The maximum positions of the Na_4^{3+} absorption bands in faujasites with different Si/Al ratios decrease monotonically with the increasing electronegativities of zeolites, which correlates well with the stability−electronegativity relationship discussed earlier.

Electrons injected into zeolites, by far-UV irradiation[228] or via photolysis of arenes included in the zeolite,[226,237,238] all exhibit sodium-trapped species that are spectroscopically identical to those found on the radiolysis of the zeolite.

6.12.2. Reactions of Alkali Metal Trapped Electrons

The alkali metal trapped electrons, for example, Na_4^{3+}, react with many solutes that are included in the zeolite. The process of Na_4^{3+}, that is, the electron, may also react, prior to trapping, with solutes. The rate constants for reaction with O_2 are much lower than those measured for O_2 reactions in solutions and the O_2 quenching of excited states. The rate constants vary only slightly but are of the order of $2-4 \times 10^4$ $Torr^{-1}$ s^{-1}.

The largest oxygen quenching rate constant in NaX is observed for the singlet excited state of pyrene, that is, $(1.32 \pm 0.26) \times 10^7$ $Torr^{-1}$ s^{-1}, which is 1000 times faster than that for oxygen quenching of Na_4^{3+} in the same zeolite. It is indicative of an activation-controlled reaction between Na_4^{3+} and O_2 within an encounter pair. The small entry pore of the sodalite cage (2.6 Å) explains the inefficient quenching by O_2 of the ion cluster trapped electrons in sodalite NaSod; oxygen pressures up to 6000 Torr were used. By the same principle, no oxygen quenching of Na_2^+ in NaA means that Na_2^+ is located in the sodalite cage of the NaA and is not accessible to oxygen. It is found that the oxygen reaction rate constants for Na_4^{3+} in different faujasites decrease as the Si/Al ratios increase, following the same trend as the stability properties; that is, the more stable Na_4^{3+} is, the more difficult it is to quench.[235,238]

6.12.3. Reactions of e− with Metal Cations

Metal ions such as Cu^{2+}, Cd^{2+}, Co^{2+}, Ni^{2+}, Zn^{2+}, Pb^{2+}, and Tl^+ tend to react with both the untrapped (precursor) and trapped electron Na_4^{3+}. For Cd^{2+}, the initial spectral adsorption of Cd^{2+} and NaY decreases statically with increasing cation exchange with Cd^{2+}.[229]

The reaction between the precursor electrons and Cd^{2+} ions in the zeolite is described in a Perrin model in which an active sphere is defined for the immediate electron scavenging. The active radius found is $R_c = 13.3$ Å.

$$e^- + Cd^{2+} \rightarrow Cd^+$$

Similar quenching studies on other cations give $R_c = 17.4$ Å for Cu^{2+} and $R_c = 17.0$ Å for T.$^+$ The kinetic traces monitored at 500 nm (Na_4^{3+}) show an enhanced decay pattern with increasing loadings of Cd^{2+} ions.

$$Na_4^{3+} + Cd^{2+} \rightarrow Na_4^{4+} + Cd^+ \qquad (41)$$

These decay kinetics are well fitted by an electron tunneling equation, where the electron transfer rate is derived from an exchange interaction.

$$k(r) = \nu \exp(-r/a) \qquad (42)$$

The precursor, ν, is the electron transfer rate at contact, r is the separation between the electron donor and the acceptor, and a is the attenuation length. For zeolites $Cd_xNa_{55-2x}Y$, ν and a are $(2.02 \pm 0.16) \times 10^8$ s^{-1} and 1.28 ± 0.04 Å, respectively. Production of reduced Cd^{2+} or Cd^+ with a spectral absorption band around 300 nm is clearly observed.[227] The same trend is seen for other M^{2+} cations. The reduced ions M^+ in zeolites are more stable than those produced in aqueous solutions. In solution, microsecond lifetimes are measured, whereas the M^+ species is stable in zeolites. The oxidative metal ions in zeolites not only participate in electron scavenging and electron transfer reactions but also play a role in modifying the potentials among the Na^+ ions and creating new trapping sites.

In contrast to other metal cations, Ti^+ ions at a low content of <0.25 per unit cell give rise to an increased production of Na_4^{3+} in Na^+-form zeolites X and Y. This is attributed to the ambivalent nature of Tl^+

ions; that is, it can be reduced to Tl^0 and also oxidized to a higher valence, Tl^{2+}. While participating in electron-scavenging reaction, hole scavenging by Tl^+ ions leads to the enhanced yield of Na_4^{3+} as it decreases the extent of the backreaction of the hold with e^-. A new transient absorption band centered at 450 nm in irradiated zeolite NaX and NaY with high Tl^+ ion contents is attributed to the formation of new sites due to the modification of zeolites by the presence of Tl^+ ions.[229]

6.12.4. Trapping of e— by Water Clusters

Small, nanometer dimension water droplets may be constructed in the zeolite cavities. These small water pools trap precursor electrons to give species that are reminiscent of hydrated electrons;[229] typical data are shown in Figure 27. These date mirror those

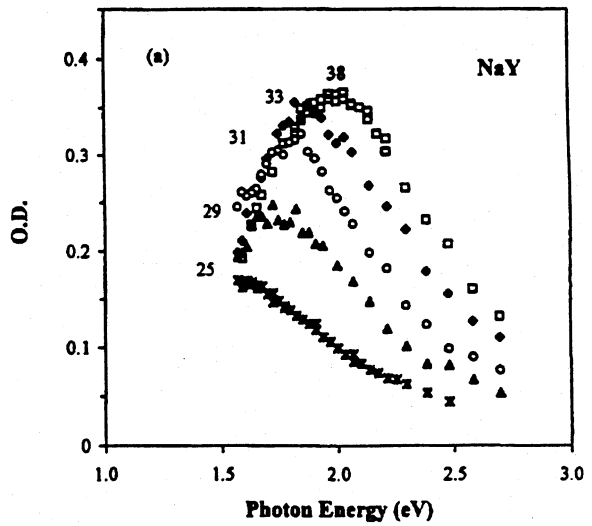

Figure 27. Spectra of e^- trapped in sodium Y with water pools as indicated. Reprinted with permission from ref 231. Copyright 1998 Elsevier.

carried out for water clusters in the gas phase.[239−241] The hydrated electron cluster $(H_2O)_n^-$ reacts with various quenchers, O_2, N_2O, etc. These molecules move in the free space of the zeolite/water system.

As expected, oxygen quenching of $(HO)_{2n}^-$ is dependent on the water content in zeolites, with the rate constant changing from $k_q = 4.68 \times 10^2$ $Torr^{-1}$ s^{-1} in fully hydrated NaX with 41 H_2O per pseudo cell to $k_q = 7.24 \times 10^4$ $Torr^{-1}$ s^{-1} in NaX with 35 H_2O per pseudo cell. The upper limit for k_q for a diffusion-controlled oxygen-quenching reaction is $k_q = 1.58 \times 10^7$ $Torr^{-1}$ s^{-1} in completely dehydrated NaX. The decrease in the quenching rate constant with the increasing water content is due to the blocking of the channels by water. Similar effects are also observed with N_2O as a gas quencher. It needs to be pointed out that this quenching leads to the formation of OH radicals.

$$(H_2O)_n^- + N_2O \xrightarrow{H^+} OH + N_2$$

This reaction increases the total OH yield from irradiation of the zeolite and H_2O.

$$H_2O \rightarrow H_2O^+ + e^-$$

$$H_2O^+ + H_2O \rightarrow H_3O^+ + OH$$

Methylviologen, MV^{2+}, reacts at a diffusion-controlled rate with hydrated electron e_{aq}^-.

$$MV^{2+} + e_{aq}^- \rightarrow MV^+$$

As MV^{2+} is bound tightly in the zeolites, this reaction may be used to measure the mobility of $(HO)_{2n}^-$ in the zeolite. This is achieved by observing the rate of decay of $(HO)_{2n}^-$ and the rise of $MV^{+\bullet}$ from the immobile MV^{2+}. The diffusion constants are then calculated via the Smoluckowski equation giving $D = 1.2 \times 10^{-7}$ cm^2 s^{-1} for 31 waters on the cage and 3.5×10^{-7} cm^2 s^{-1} for x38 included H_2O molecules. These values are much lower than that in bulk water, $D = 4.9 \times 10^{-5}$ cm^2 s^{-1}. It is noteworthy that the transfer from Na_4^{2+} to $(H_2O)_n^-$ may be observed spectroscopically.[230]

However, solutes such as pyrene cannot compete with the Na_4^{4+} cluster for electrons. It is possible to observe e^- transfer from K_3^{2+} to pyrene, in K^+-exchanged zeolites. The electron affinity of K_3^{3+} is smaller than that of pyrene and other arenes, making it possible to produce arene radical anions in KX and KY via the reaction of e^- with the arene.

6.13. Cation Formation

The formation of stable radical cations and their reactions in zeolites has already been referred to,[191,226] and, here, it is necessary only to draw attention to a few studies. Photolysis of many arenes in zeolites leads to photoionization via one- and two-photon processes.[235,238,242,243] The arene radical cations produced are the concomitant part of the trapped electron in alkali metal clusters. These species are also formed via radiolysis of the arene in a zeolite, the h^+ produced in the zeolite entering into electron transfer with the arene. This area has been extensively reviewed[244] and covers extensive work on the EPR of several arenes radiolyzed in zeolites. As shown earlier, the hole, initially produced, creates radical cations of the adsorbates. EPR studies identify these species and the subsequent temperature-induced transformation. These studies are particularly important to zeolite catalysis, as many of these processes are involved in the cracking of organic molecules. It is pertinent to note that the stabilized radical cations on the zeolite are not as reactive as their counterparts in solution. For example, dimethlanniline laniline reacts rapidly with biphenyl and pyrene radical cations on SiO_2 and in solution. However, little reactivity is observed for these radical cations with DMA in zeolites.[217] One might suspect this to be the case due to the stability endowed by the partial negative charge of the zeolite on the radical cation.

6.13.1. Electron Extraction from Zeolites

Photoexcitation of molecules in zeolites can also give rise to electron transfer from the zeolite to the guest molecule, thus forming a radical anion.[198,245]

Many factors such as the Si/Al ratio, the nature of charge balancing cations, the preactivation temperature, the pyrene loading, the state of hydration, and the nature of the surfaces (external versus internal) were examined to understand the formation and stabilization of $Py^{\bullet-}$ in these samples and also the mechanism of the photoinduced electron transfer processes. The studies show that photoinduced electron transfer does not occur from pyrene to pyrene in the zeolites to produce $P^{\bullet+}$ and $Py^{\bullet-}$, but occurs between pyrene molecules and the acidic and basic sites of the zeolites. The basic site of the zeolites, responsible for the formation of $Py^{\bullet-}$, requires the special environment of the zeolite supercage; it is noteworthy that $Py^{\bullet-}$ cannot be formed on the external surface of a zeolite. The formation $Py^{\bullet-}$ in the different alkali-ion-exchanged zeolites X and Y follows the order of basicity of these samples, which is calculated using the Sanderson electronegativity equalization principle. Preactivation of the samples at temperatures of 350, 550, and 750 °C does not affect the ratio of the anion to cation, $Py^{\bullet-}/Py^{\bullet+}$, yields. Posthydration of the samples alters the photophysical processes in the zeolites and gives rise to an increase in the yield of $Py^{\bullet-}$. At low light intensities, the photoinduced electron transfer follows a single-photon mechanism. Table 17 illustrates the yields of excited singlet, triplet, radical anion, and radical cation of pyrene in several zeolites. In all cases the yields are smaller than those reported in solution phase. The yields of the radical anion correlate well with the partial change on the zeolite framework. This indicates that the yield of this species is related directly to the basicity of the zeolite.

Photoexcitation of methylviologen, MV^{2+}, on SiO_2 gives rise to the reduced viologen, $MV^{\bullet+}$, and presumably a cation state of the SiO_2. Similar data are obtained with MV^{2+} in zeolites.[246] The subsequent decay of $MV^{\bullet+}$ follows the framework basicity of the zeolite, the longest lifetime for $MV^{\bullet+}$ being observed in a Cs-exchanged zeolite. The electron transfer can take place without light if the zeolites are heated.[247,248]

Methylviologen is an exchange ion in these systems. It is possible to also include arenes, such as anthracene and naphthalene, in the same supercage as MV^{2+}. The constraints placed by the zeolite in the reactants lead to efficient ground state charge transfer between the two guest molecules, forming MV^{+} and $arene^{\bullet+}$, and this leads to brightly colored zeolites. This area has been reviewed previously,[247] and no further discussion is called for here. Excitation with visible light of the CT ground complex in the zeolite leads to charge separation as observed by rapid spectrophotometry.[243] It is claimed that the zeolite contributes significantly to extending the lifetimes of the ions compared to solution. The popular photochemical molecule ruthenium tris(bipyridyl) has been incorporated into zeolites, via internal synthesis.[249,250] Photoinduced electron transfer to MV^{2+} is observed with the two reactants being in separate supercages. The lifetime of the ion pair was estimated at ~1 h. This may be compared to microseconds in solution. So far, attention has been drawn to the marked effects of zeolites on electron transfer processes. There are reports of several unique effects of zeolites on organic reactions. It is pertinent to draw attention to these studies.

6.14. Pore Restriction of Reactions

The narrow nanometer dimension of the pores and supercage cages in zeolites have been alluded to earlier. Attention was also drawn to the ease with which molecules, in particular co-adsorbed solvent, restrict the motion of reactant theory modified the subsequent physical processes and reactions. However, even more profound modification of chemical reactants by zeolites has been illustrated.[251−257] Figure 28 gives the structures of several ketones listed

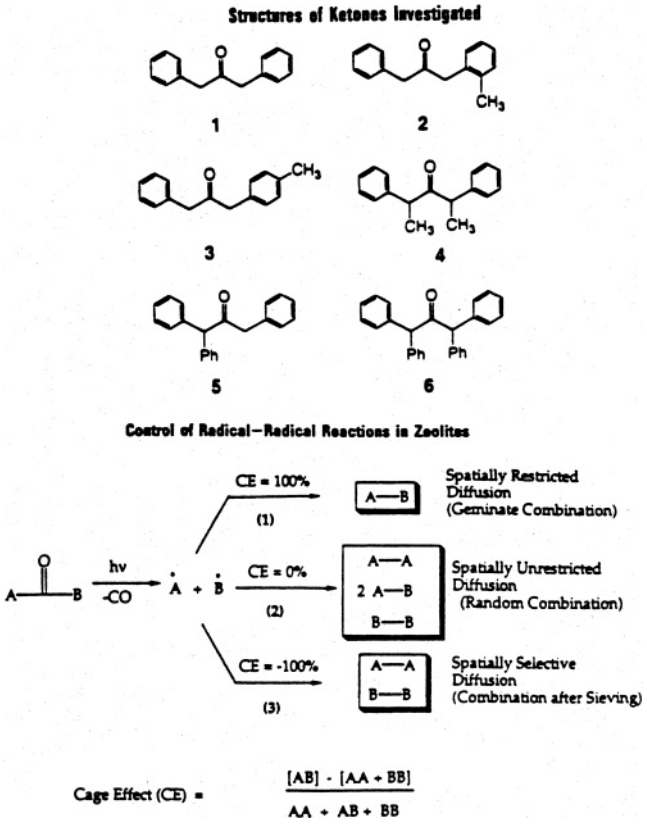

Figure 28. Photoylsis of ketones on zeolites: three limiting "cage effects" for secondary radical−radical combinations. The cage effect is defined in terms of the product ratios observed in the photolysis as shown in the figure. Reprinted with permission from ref 257. Copyright 2000 American Chemical Society.

as 1−6, together with the various permutations of the radical−radical process that ensue on photolysis of these compounds. Molecules 1−6 are chosen as their interaction with zeolite is affected by their size or geometry. Due to the dimension of the molecules and that of the zeolite, the following can be stated:

Molecules 1 and 3 will fit into the external pores of MFI zeolites (the MFI zeolites being silicalite and ZSM-5) and will access the interior of the zeolite. Molecules 2 and 4−6 will be able to locate a benzene ring into the pores of the external surface but will not be able to enter the zeolite itself. Photolysis rapidly leads to reduced A and B, which subsequently recombine to give products A−B, B−B, and A−A. In

nonviscous solution the cage effect is close to zero and leads to randomization of the radicals in the medium.

Photolysis of molecule 2 on MFS zeolites results in the formation predominantly of A−A and B−B as products. This happens as photolysis in a pore on the surface produces two radicals, A and B, one of which remains on the surface and one of which enters the interior of the zeolite. Thus, A and B are segregated and A−A and B−B recommendation is favored. At higher loadings the surface pores are filled, further adsorption is to the surface, and a two-phase system, with a different cage effect, is obtained.

Photolysis of molecule 3 is at the internal surface of the zeolite where radicals A and B are constrained in pairs in a region of space. Th major product is A−B. For molecules 1 and 4 the geometry of the radicals generated together with the restriction of the zeolite limits their subsequent recombination reactions and produces steric chemistry. For molecule 1, the product 1,2-diphenylethane dominates, and for molecule 2 the products are styrene and ethylbenzene. For molecules 4−6 in zeolites EPR signals of the radicals persist for many hours.

Photolysis of molecules 1−6 in zeolites such as X and Y leads to selective recombination of the radicals A and B, which can be influenced by the zeolite-incorporated alkali metal ion. These studies illustrate several aspects of photochemical reactions where the geometry of the zeolite directs the outcome of the products.

6.15. Aromatic Ketones in Zeolites

6.15.1. Effects of Acidic Centers

Much is known regarding the photochemistry of aromatic ketones in solution, in particular acetophenone and benzophenone.[258] The important features are that excitation of the ketone leads to the rapid (picosecond) formation of the triplet excited state. The benzophenone triplet reacts rapidly (less than a microsecond) with many solvents to give radicals.

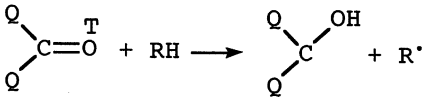

In zeolites, for example, ZSM5, it has been shown[259] that at low loadings of benzophenone (10^{-7} mol/g) the photoemission is due to the acidic form, which changes to that of the normal nπ^* state at higher loadings, and there is no indication of the $\pi\pi^*$ state. However, in the analogous acetophenone system, recent studies[260] show that the polar nature of a zeolite enhances the $\pi\pi^*$ state of this molecule.

The small porous nature of the zeolite systems poses many restrictions on chemical reactions. Studies show that the restriction and nature (nπ^* $\pi\pi^*$) of the benzophenone excited state markedly affect the photochemistry of several ketones and other molecules in zeolites.[261−264]

It is instructive to consider laser flash photolysis studies of the triplet excited state of benzophenone, B^T, on various surfaces, SiO_2 and zeolites NaY, KY, NaX, and KX, and in rigid media at room temperature, polyethylene and polyethylmethacrylate.[265] The studies point to similarities of the spectroscopy and kinetics of B^T in fluid solution, in solid solution (polymers), and on a SiO_2 surface. However, stark differences are observed for B^T in zeolites, where the absorption spectrum mimics that of the protonated ketone. The reactivities of B^T with C_6H_{12} and CH_3OH are an order of magnitude smaller than those of liquid C_6H_{12} and CH_3OH. These data are discussed in terms of the interaction of benzophenone with acidic sites in the zeolites and restrictions placed on the reactants in the zeolite cages. This is one of the few cases in which zeolites inhibit rather than promote reactions of solute adsorbed in them.

6.15.2. Photooxidation of Alkenes in Zeolites

There are several reports of the visible photooxidation of alkenes in zeolites.[266−273] The basic observation is that the zeolite host induces CT complexes of O_2 with the alkene, which lead to a spectral absorption that tails into the red part of the spectrum. Excitation into this visible band leads to selected products, quite unlike the solution phases where random products are obtained. In solutions this is interpreted as a proton transfer from the hydrocation radical cation to O_2^- as the invited step. However, UV excitation is needed for this process, in contrast to the zeolite systems where lower energy visible quantum initiates chemistry. An example is

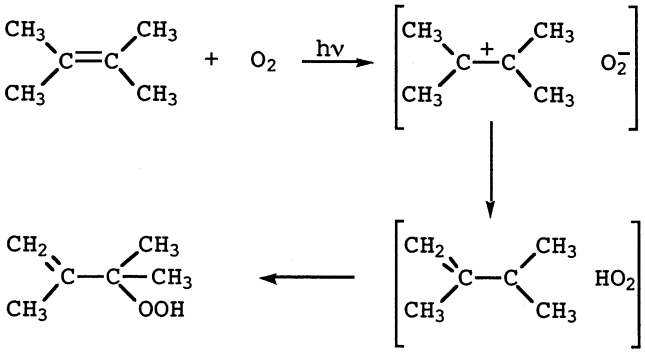

Other examples of selective oxidation are

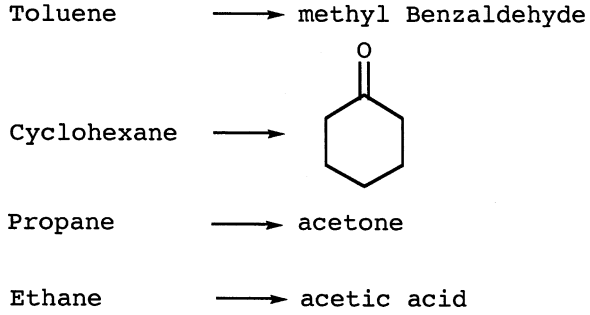

These studies are noteworthy as the zeolite reduces the energy needed to produce the chemistry (visible other than UV photons), and the process is selective.

6.15.3. Asymmetric Photoreactions within Zeolites

The confined spaces of zeolites are also conducive in achieving chiral induction for several molecules.[274] Excess diastereometric material up to 90% and

enantiometric excesses up to 78% have been achieved by various systems. Reference 274 deals in detail with the many aspects of this unique chemistry. The authors suggest that the zeolite cavity and the alkali metal ions contained in the cavity (up to 5 m) force the molecules to adopt a geometry in which enhanced interaction occurs between the chiral center and the site of the reaction. The alkali metal ions interact with the adsorbed molecules and help to induce the transformations. In solution, this effect is wasted by the interaction of the solvent molecules with any alkali metal ions present, thus inhibiting their interactions with the molecule of interest. These interesting studies refer back to earlier studies in which the metal ions of the zeolite markedly decrease fluorescence lifetimes and enhance triplet yields of adsorbed molecules.

6.16. Channel Zeolites

Channel zeolites are particularly useful in creating arrangements of molecules, an aspect which will be illustrated later.

Studies[197,198] of adsorption and location of pyrene molecules in zeolites L and mordenite using photophysical techniques reveal that the internal surfaces of both zeolites are polar, similar to that observed for zeolites X and Y. The external surface of zeolite L is similar to its internal surface for the adsorption of pyrene, and excimers are easily produced on it, whereas the external surface of mordenite is different from its internal surface for adsorption, and excimers are not observed on it even at the highest loading of pyrene. Due to the protection of pyrene molecules by the channels, the efficiency of O_2 quenching of the excited pyrene is 1 order of magnitude smaller in zeolite L than in zeolites X and Y, and 30−35% of pyrene cannot be quenched by O_2 in mordenite. The rotational movement of pyrene in the zeolites is also restricted by the structure as revealed by fluorescence anisotropy measurements.

6.17. Directed Energy Transfer

The long narrow channels of some zeolites, for example, zeolite L (ZL), have been used to align various dye molecules to accentuate energy transfer.[275−277] The concept of the process is to use the cylindrical channels of ZL to align a host of dye molecules. A suitable choice of dye molecules for this procedure is pyronine blue

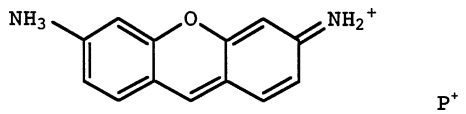

P+

which will lie with its long axis approximately along that of the zeolite channel. The zeolite crystal is first loaded with P+′, then the molecule oxonine OX+

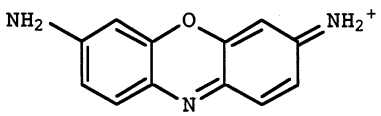

OX+

is loaded to the surface. Excitation of the P+ blue now gives rise to emission from the chromophore at the ends of the channel, due to energy transfer along the antenna molecules in the channel to the receptor at the end of the zeolite crystal. A typical example of the process is shown in Figure 29a. The process can be more generalized by placing "stop-cock" receptor molecules to cap the zeolite. A diagram of a possible stopcock molecule is shown in Figure 29b. These studies again show the versatility of zeolites in constraining and organizing systems to promote unique facets of the physical events induced in them.

6.18. Further Selected Examples

There are numerous examples of photoinduced reactions in zeolites that do not fit easily into the above agenda. Several are selected to illustrate the utility of zeolites in many systems and are discussed briefly.

6.19. Luminescence of Inorganic Molecules in Zeolites

Inorganic cations have been exchanged into zeolite and their emission characteristics used to comment on the zeolite.[278−283] For Ag^+ in zeolites Y and X,[278] the luminescence is similar to that of Ag^+ in rare gas matrices, and the spectrum shifts with the Si/Al ratio as a consequence of the charge density and polarizability of the Ag^+ environment. Cuprous ion (Cu^+) is readily produced from Cu^{2+} adsorbed in zeolites. The quenching of the luminescence of the Cu^+ by O_2 can be used to assess the distribution of Cu^+ in the zeolite.[279] Other studies with UO_2^{2+} have looked at energy transfer.[280,281] It was found that the efficiency of the energy transfer depended on the apparent dimensionality of the zeolite.[282] For zeolite A with surface-bound UO_2^{2+}, the transfer of energy to Eu^{3+} was high at 93%, whereas UO_2^{2+} on the inner surface of X and Y gave only an efficiency of energy transfer of 40%. The channel-like zeolite ZSM-5, in which the dimensionallity decreases, gave only a 20% efficiency of energy transfer.[280]

IR studies of Eu^{3+} ions in zeolite Y have been used to investigate the site symmetry of the luminescent probe.[283,284] The studies suggest that Eu^{3+} is at sites of C_s, C_n, or C_{nv} symmetry and that a glassy environment exists for the probe. A pertinent review[284] outlines in more detail these and other studies with inorganic probes in zeolite. This area has not seen as much activity as that with luminescent organic probes in zeolites, but it could give invaluable information on the microenvironment in zeolites.

Zeolites have also played host to compounds of silver, Ag_2S and Ag_4S_2,[287] and Ag^+.[286,287] Silver chloride has also been constructed in zeolites,[285] and it is reported that photolysis of this material can lead to water splitting, giving H_2 and O_2. Heating (>600 °C) the product reduces more water to H_2. Another study also claims that visible light illumination of a silver zeolite at 600 °C gives rise to O_2 from adsorbed water and molecularly dispersed silver.[289] A question does arise as to whether this system is stable at this temperature. The splitting of water to O_2 probably occurs via the mechanism given below, which was

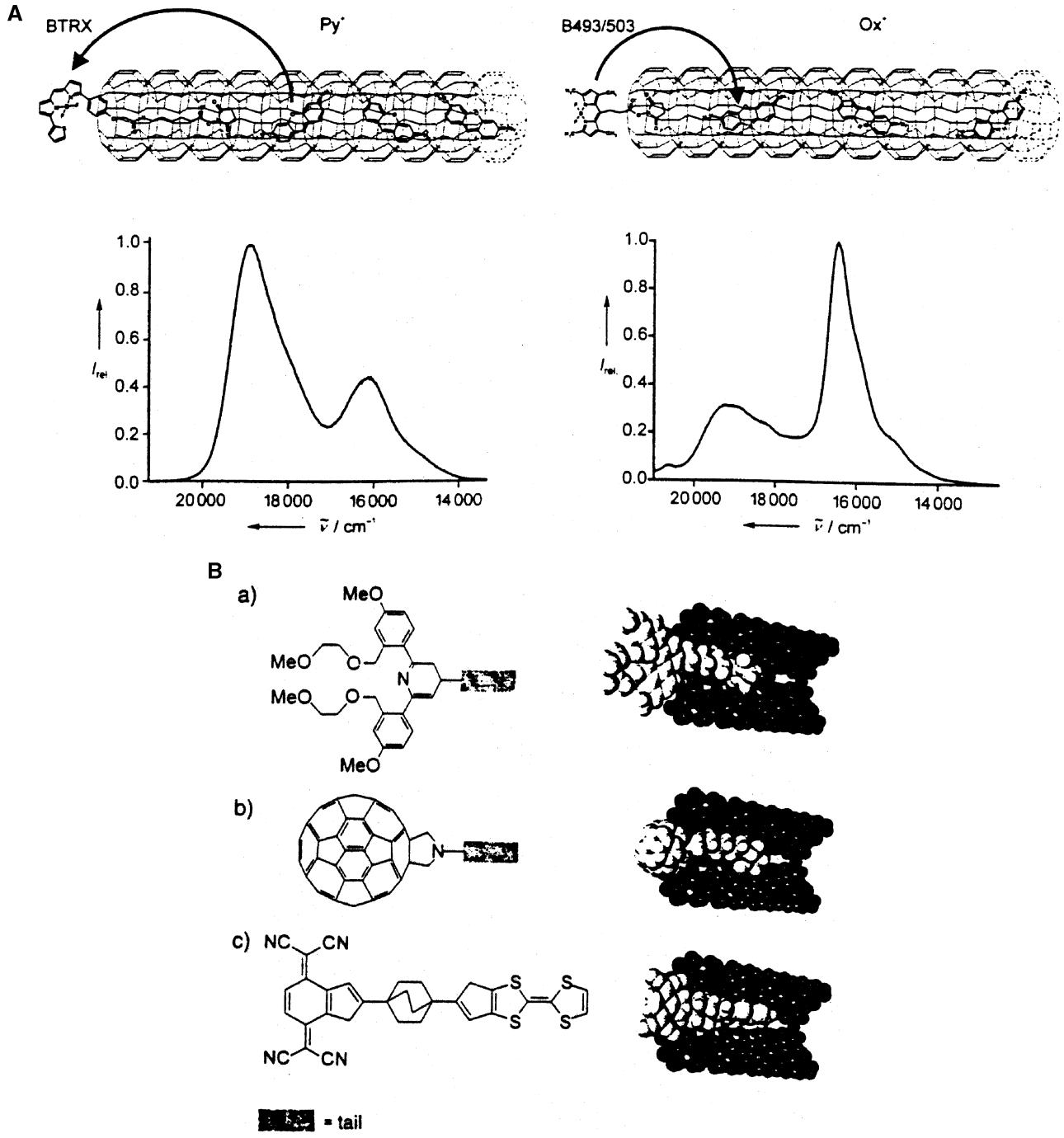

Figure 29. (A) (Left, top) P^+-filled zeolite L channels. The ends of the channels are modified by BTRX stopcocks for external trapping of electronic excitation energy. (Left, bottom) Fluorescence spectrum after selective excitation of P^+. (Right, top) Ox^+-filled zeolite L channels. The ends of the channels are modified with B493/503 stopcocks for electronic excitation energy injection. (Right, bottom) Fluorescence spectrum after selective excitation of B493/503. Reprinted with permission from ref 277. Copyright 2003 Wiley. (B) Examples for stopcock molecules. The space-filling model of a channel is shown (cut in half) with the stopcock to illustrate that the dimensions of the stopcock are appropriate: (a) fluorescent chemosensor; (b) C_{60}-based stopcock; (c) molecular rectifier stopcock. Reprinted with permission from ref 277. Copyright 2003 Wiley.

established for a $Ag^+/AgCl$ colloid system.[290]

$$Ag^+ + OH^- \xrightarrow{h\nu} Ag + OH$$

$$OH + OH \rightarrow H_2O_2$$

$$H_2O_2 + nAg \rightarrow \frac{1}{2}O_2 + H_2O + nAg$$

catalytic reaction

A recent paper[291] studying O_2 production at an illuminated silver chloride anode suggests an alternative mechanism. It is suggested that light absorption by the $Ag^+/AgCl$ electrode leads to charge transfer, forming Ag^0 and Cl atoms. This is followed by Cl atom dimerization giving Cl_2, hydrolysis of which gives HOCl, H^+, and Cl^-. The HOCl is finally catalytically decomposed by Ag^+ to O_2.

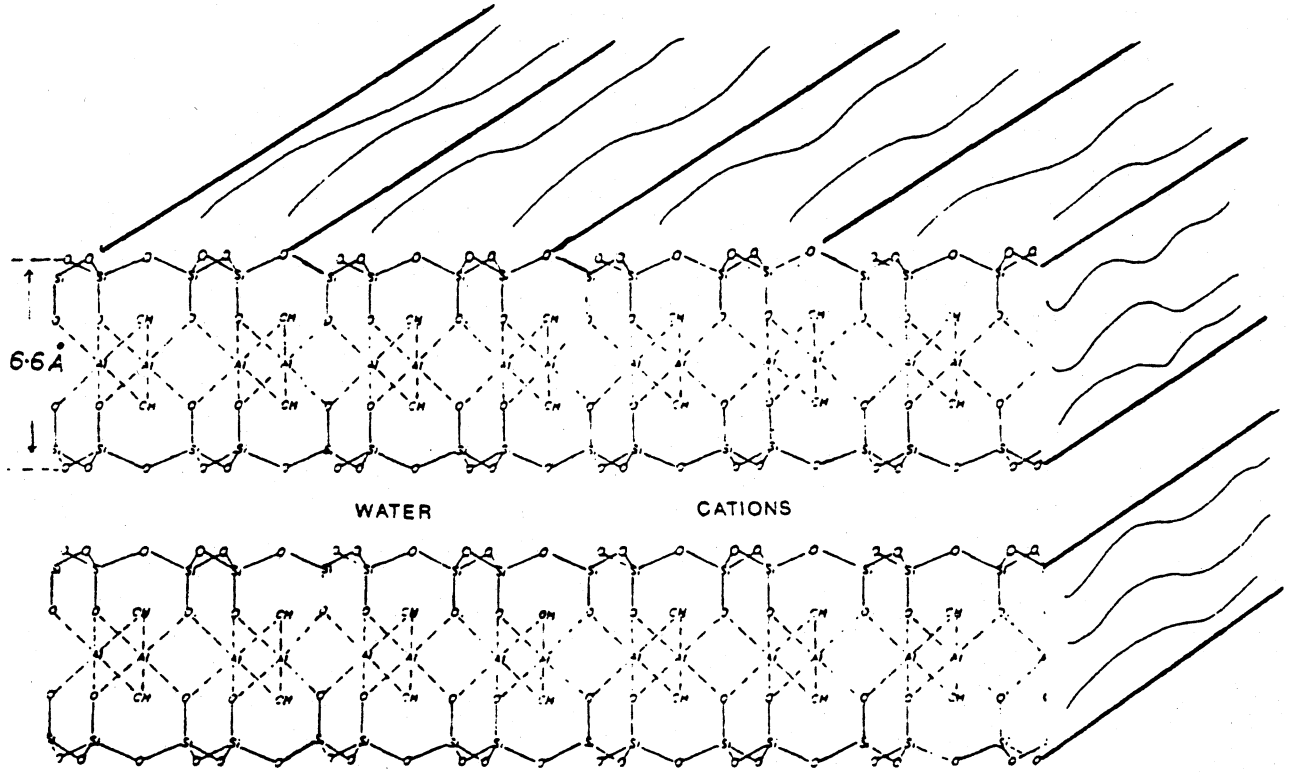

Figure 30. Diagrammatic representation of a 2:1 layer clay structure.

6.20. Summary

The photochemistry of various chemical systems in zeolites is reminiscent of that seen previously in SiO_2 and γ-Al_2O_3. Molecules are adsorbed on the zeolite surface at CT sites that are of acidic nature. The effects of the acidic sites on the zeolite can be significantly decreased if the sites are blocked with ammonia, water, or alcohols. The arenes then exhibit photophysical characteristics seen in polar solvents. An advantage of these sites in zeolites, one that differs from that in SiO_2 or γ-Al_2O_3, is the enhancement of oxygen−organic CT complexes, which lead to intriguingly selective chemistry in photoexcitation. Another feature, which differs from that in SiO_2 or γ-Al_2O_3, is the selective nature of the smaller pores of the zeolite in promoting certain reactions at the expense of others. This is apparent in photoinduced free radical reactions, where only small radicals enter the zeolite. The small tight confinement of molecules in the supercages enables the construction of CT complexes such as those formed between methylviologen and arenes. The polar and ionic nature of the zeolite leads to significant charge stabilization following photoexcitation of adsorbed molecules. The CT sites also lead to charge separation with low-energy quanta, and ionic products are formed at much lower energies than in solution. The coupling of the acid and base sites of the zeolite leads to several marked catalytic effects on photochemical reactions.

With silica the large sizes of the pores enable incorporation of large solutes, at sizes that cannot diffuse through the pores of zeolite X or Y. To some extent the organized silica MCM41 incorporates large solutes, but as it is not a zeolite, it does not process the catalytic sites of these materials. Attempts to provide this activity by incorporation of Al led to silica−alumina catalysts.

It is difficult to extend the size of the supercages in zeolites to incorporate large molecules. To some extent this can be achieved by the use of expanding bentonite clays, which have empirical formulas similar to those of zeolites but a different geometric structure.

7. Photochemistry on Clay Systems

Finally, it is appropriate to draw attention to some studies in clay systems. The earlier part of this review dealt with "natural" SiO_2 and Al_2O_3, whereas these species may be reorganized to give "ionic" zeolites or ionic clays. The mismatch in the valency of Al and Si produces zeolite structures that contain countercations to balance the structure. The same is true of clays, but these structures differ considerably from those of zeolites. These structures are layered, and in water the layers can be pried apart to make colloids. This is a property unique to clays and important in the ecology system. Although this review deals with solid structures, it is important to consider the "small solid colloidal" structures of water−clay colloids.

7.1. Structures of Clay

Figure 30 shows a diagramatic representation of two clay layers with the Al, Si, and O atom positions shown in the end cuts and the interlayer space with water and cations. Ionization of such expanding clays in water leads to layer separation and colloid particles containing charge of $n(-ve)$ and with nM^+ in solution. The metal ions are depicted as M^+ and the

number of charges as n. Heating a normal clay at 104 °C leads to a dry clay as the interlayer water is lost. The clay sheets are ~6.6 Å thick, and the interlayer space varies with water content from ~5 Å upward.[292,293] A convenient synthetic clay for study is laponite, containing Li, Mg, Si, and O.

7.2. Colloidal Clay

Laponite is a synthetic counterpart of natural hectorite clay with a layered structure. The layer is composed of two SiO_4 tetrahedral sheets and one MgO_6 octahedral sheet arranged in a TOT sandwich (T = SiO_4 tetrahedral sheet and O = MgO_6 octahedral sheet). The Mg^{2-} ions in the octahedra are partially substituted by Li^+ ions, which provide the source of the negative charge of the sheet. The negative charge produced by the substitution is compensated by Na^+ cations located in the interlayer space. The interlayer space can also accept water molecules and, as a consequence, is expanded to an extent depending on the actual conditions of hydration. The surface of a dried laponite particle is built up of an outer surface that involves siloxane bonds and a lateral surface of the layers that include broken and terminated Si−O and Mg−O and/or Li−O bonds. The particle also includes an interlayer surface partially covered by Na^+ cations. The main advantage of this material compared to naturally occurring clays is that the laponite is available in a high degree of purity and contains a minimum of other active atoms such as Fe^{3+} and Cu^{2+}. The copper and iron contents of natural clay are photoactive and quench the fluorescence of adsorbed probe molecules.

The alkali metal counterions of the clay may be exchanged with other cations, which are then located at the clay surface. The well-known luminescent probe ruthenium tris(bipyridine) [$Ru(bpy)_3^{2+}$] is an ideal molecule to locate at the surface of a colloidal clay system. Numerous studies with this probe[294−296] have been reported. Time-resolved emission spectra display a red shift in the emission maximum over time. Results of kinetic and spectral analyses indicate the existence of two distinct adsorption environments for the luminescent probe molecule on the flat clay surface. Each type of adsorption of the probe molecule results in a unique lifetime and emission spectrum, which are obtained through mathematical deconvolution of observed data based on a multiexponential model. Additional experiments utilizing clay powders and films, luminescence quenching reactions, ion exchange measurement, and chemical modifications of the clay surface provide evidence for the nature of the distinct adsorption mechanisms. An interpretation is proposed on the basis of the existence of two different types of adsorption zones at the surface of the clay. At one type of adsorption zone the water is held rigidly and presents an environment to the ruthenium tris(bipyridine) probe that results in a short lifetime and a blue-shifted emission. The second absorption zone involves a stronger interaction directly with the clay surface so that the photophysics are less influenced by the nature of the surrounding water. Direct comparison of photophysical properties of the luminescent probe on the clay and in ice at −20 °C supports the model.

Other cations, for example, the tetramethylbenzidine radical cation TMB^+, also absorb strongly to the clay surface and give rise to dimer cations.[297] This facilitates studies to measure the rate of radical cation (negative) clay particle interaction.

Photolysis (λ < 4000) of benzidine (BD) or TMB in aqueous or alcohol/water mixtures in the presence of colloidal clay leads to a green solution. Flash photolysis studies indicate that the initial photochemical event is photoionization in the bulk aqueous phase

$$TMB \xrightarrow{h\nu} TMB^+ + e^-_{aq}$$

as both TMB^+ and e^-_{aq} are observed spectroscopically. The hydrated electron e^-_{aq} reacts rapidly ($\tau_{1/2}$ < μs) with O_2, giving O_2^-; TMB^+ has a much longer lifetime (τ > 1 ms), which is shortened in the presence of clay, when the spectrum characteristic of TMB^+ (λ_{max} = 4700 Å) is replaced with a spectrum with λ_{max} = 3900 and 6250 Å. The resulting species is bound tightly to the clay and is most probably cationic in nature. Unfortunately, its EPR signal is too broad for identification purposes. Addition of acid to the sample changes the color of the clay from green to orange, the color of the dication, TMB^+, and the EPR signal disappears. This is typical of the behavior of TMB^+ in micellar NaLS solutions. The studies show that TMB^+ is captured by the anionic clay, and the TMB^+−clay interaction gives rise to a dimer of TMB^+.

7.3. Surface Configuration of Adsorbed Molecules

The cationic probe molecule (pyrenylbutyl)trimethylammonium bromide (PN^+) adsorbs strongly to colloidal clays[294,297,298] and tends to cluster on the clay surface, as the predominant luminescence in that of the excited $(PN^+)_2$* or excimer.

$$PN^+ \xrightarrow{h\nu} (PN^+*) \xrightarrow{PN^+} (PN^+)_2^*$$

Addition of a cationic detergent such as cetyltrimethylammonium bromide (CTAB) decreases the excimer yield and gives a concomitant increase in the yield of monomer excited states (PN^+)*. This is due to a mixing of the PN^+ and the cationic detergent on the surface, which leads to a separation of the clustered PN^+ on the surface. A cationic detergent with a carbon chain of >8 is needed to observe this effect. The addition of CTAB also causes a decrease in the degree of fluorescence polarization. This is due to loosening of the chromophore of PN^+ from the clay surface by the CTAB that gives it greater rotational mobility.

These studies have identified the nature of the configuration of adsorbed molecules on clay surfaces and indicate how the geometry of adsorbed molecules at the surface controls the photochemistry. This is borne out by steady state and time-resolved fluorescence quenching studies of excited PN^+ by cetylpyridinium chloride (CP^+). Both reactants are adsorbed on colloidal laponite clay, and typical data are shown in Figure 31. Initial addition of quencher CP^+ leads

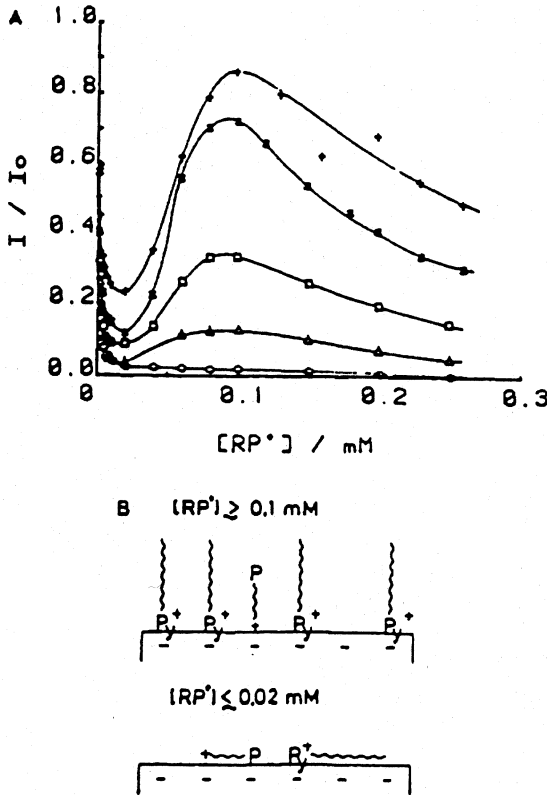

Figure 31. (A) Influence of the alkyl chain length of various alkylpyridinium ions on the PN^+ fluorescence quenching behaviors in Laponite colloids (5 g/L): (○) ethyl-; (△) pentyl-; (□) octyl-; (∗) dodecyl-; (+) hexadecyl-; $\{PN^+\} = 5 \times 10^{-7}$ M. (B) Schematic model for PN^+ fluorescence quenching by alkylpyridinium ions: (Py^+ ∿), alkylpyridinium ions; (+ ∿ P) PN^+. Reprinted with permission from ref 298. Copyright 1985 American Chemical Society.

to an efficient quenching of PN^+ fluorescence. Further increase of quencher gives a reverse effect, whereby the fluorescence recovers to a yield greater than that observed without quencher. The degree of recovery increases with the chain length of the alkylpyridinium ions. These results are examined in terms of a change in geometrical arrangement of PN^+ adsorbed on the clay (Figure 31). PN^+ tends to cluster on the clay surface, and the molecules lie on the surfaces with the pyrene chromophore close to the surface. Co-adsorption of alkylpyridinium (AP^+) onto the clay surface places the cationic quenching pyridinium group at the clay surface in close contact with the pyrene chromophore. This leads to quenching of pyrene fluorescence. Further addition of AP^+ leads to the formation of a layer of surfactant that solubilizes and locates the pyrene chromophore away from the clay surface. Fluorescence quenching decreases as the pyrene chromophore is now located in a hydrophobic organic environment, quite unlike that of the polar clay surface. The PN^+ fluorescence in hydrophobic environment is larger than that in a polar environment, which accounts for the subsequent increase of PN^+ in CP^+, which is greater than that in the absence of the quencher.

PN^+ fluorescence is quenched by dimethylaniline, nitrobenzene, and nitromethane in a CTAB−laponite system, and the kinetics are of the Poisson type. This indicates that the adsorbents exist in the form of clusters or zones on the clay surface. With laponite the islands are finite, containing ∼100 cationic exchange sites grouped together in close proximity.[299]

7.4. Degree of Dispersity of Colloidal Clay

The photophysical properties of water-soluble tetrakis(*N*-methylpyridyl)porphyrin (TMPyP) are altered upon adsorption to the surface of a smectite clay mineral in an aqueous disperson.[300] In particular, the Soret absorption band shifts from 421 nm in aqueous solution to 452 nm when the molecule is adsorbed on the external face of a clay sheet in contact with the bulk solution. Upon intercalation between clay sheets, the Soret band further shifts to 488 nm. The net Soret absorption band observed in a particular clay sample is a superposition of contributions from intercalated versus externally adsorbed porphyrin and provides a convenient method to monitor the degree of dispersion or extent of deflocculation of a clay dispersion to produce primary particles or single sheets. Furthermore, the spectral changes can be utilized to assess the effect of chemical and physical modification to the clay dispersion on the extent of face-to-face particle aggregation. Shifts in the fluorescence spectrum parallel those of the Soret band. A mechanism that could account for the substantial spectral changes observed is proposed.

7.5. Pillared Clay

The interlayer spacing of clays may be "propped" open to give uniformally spaced layers with hydroxide alumina prepared by slowly dissolving $AlCl_3$ in water.[300] The pillaring agent is believed to be $Al_{13}O_4(OH)_{24}(H_2O)_{12}^{7+}$.[301] Also, alkylammonium compounds can be used to give spacings of 15.5 Å (*n*-butyl) and 14.5 Å (ethyl).

Hydroxy-aluminum-pillared montmorillonite, hectorite, and tetraalkylammonium-pillared hectorite prepared in this way exhibit enhancements in adsorptive properties. Photochemical quenching of intercalated ion-exchanged tris(bipyridine)ruthenium probe molecules is used to track the rate of penetration of reactive species into the interlamellar region from solution. The microporosity of the alkylammonium-pillared clays depends on the degree of layer separation as does the extent to which the pores are blocked by the alkyl substituents. Studies utilizing gas phase oxygen to react with tris(bipydridine)-ruthenium intercalated within the pillared clays as dry powders report on the microporosity of the various clay samples. Much has been done in this area of clay research, which is of immediate interest to catalysis in industry.

7.6. Dry Clays

To adsorb probe molecules to the system colloidal clay particles, it is necessary to achieve some positive charge on the probe, for example, ruthenium−trisbipyridyl or pyrene−alkyl-trimethylammonium. Pyrene will not adsorb on aqueous colloidal clay systems, but it will adsorb on "dry" clays. The probe has been used in studies[302−304] of the surface properties on laponite. It has been shown that the adsorption

capacity, polarity, and electron-accepting ability of the laponite surface are dependent on the preactivation temperature and on actual conditions that laponite undergoes. In the case of thermal activation, the surface polarity of laponite increases in the temperature range of 100−350 °C, whereas above 440 °C the polarity decreases. The adsorption capability of the surface for pyrene molecules increases dramatically at preactivation temperatures >100 °C. The electron transfer between the adsorbed pyrene molecule and the surface active sites (which accept electrons from the adsorbed pyrene molecules) takes place only in the temperature range of 100−400 °C. Pyrene cation radicals start to form on the lateral surface of laponite at 115 °C. The effect increases linearly with the temperature up to 350 °C and then decreases dramatically as the temperature increases beyond 440 °C.

Irradiation of the samples with UV light (370−300 nm) dramatically increases the yield of the pyrene radical cations and is 24 times larger than the sample without irradiation. The formation of pyrene radical cations is shown to be a single-photon ionization process. This was done by varying the intensity of UV light and by irradiation under the presence of O_2. The mean lifetime of the pyrene radical cation created on the surface of Na^+−laponite ($\tau_{1/2}$) is 74 h. There is a distribution of electron-accepting sites on the surface that ionize the adsorbed pyrene molecules. These sites require different photon energies for the adsorbed pyrene molecules to promote the electron transfer. UV light with energy as high as 3.4 eV (340 nm) is sufficient for all surface active sites to accept electrons from the adsorbed pyrene molecules. Below this energy, some sites cannot accept electrons from the molecules. Experiments of blocking the lateral surface of the clay with polymetaphosphate molecules and adsorption of water and NH_3 on the surfaces reveal that most of the active sites (82−86%) are located on the lateral surface, whereas others (14−18%) are located elsewhere in the regions that are unaffected by these molecules.

Pyrene may be photoionized in laponite to produce a broad absorption band from 450 to 800 nm.[304] Laponite has a layered structure with charge-balancing Na^+ ions only in the interlayer space, and so electron trapping by the cations can occur within this space. It is known from XRD studies that after dehydration the thickness of the interlayer space is approximately the size of a Na^+ ion. The confinement of the cations in the interlayer space by the TOT layers restricts the geometry of the Na^+ clusters. The Na_2^{2+} and Na_3^{3+} clusters are the most probable electron-trapping sites expected in the clay. The spectrum exhibits absorption bands in the region of 400−800 nm that are similar to those seen in mordenite, where Na_2^+- and Na_3^{2+}-trapped electrons are observed. Examination of the signal decays at different wavelengths shows that the absorption band is composed of more than one type of trapped electron. The signal decays are grouped into two types of trapped electrons; therefore, the absorption band in the spectrum is assigned to Na_3^{2+} for the shorter wavelength part and to Na_2^+ for the longer wavelength part.

The photooxidation of arenes on laponite leads via the radical cation to stable product.[305,306] This is clearly seen in the photochemical reactions of the model compound biphenyl on laponite surfaces. Diffuse reflectance and fluorescence spectroscopic studies indicate that adsorbed biphenyl molecules interact with solid surfaces in two ways: a physical interaction that leads to a bathochromic shift and a broadening of absorption bands, and a chemical interaction that leads to surface complexes with CT character. Photo-irradiation of the surface complexes results in the formation of radical cations, $Ph_2^{\bullet+}$, which are observed by diffuse reflectance and EPR spectroscopy. Product analysis confirms that biphenyl is photochemically degraded on laponite on irradiation into the CT band and that the mechanism is free radical in nature. The important reaction of radical cations on surfaces is hydrolysis, resulting in hydroxy compounds. The present results indicate that layered silicates are more active than silica−alumina gels in the above processes.

Similar data are obtained with thianthrene (Th) on laponite; that is, photoinduced electron transfer from thianthrene to laponite is observed. Diffuse reflectance and fluorescopy studies show that adsorbed thianthrene molecules interact with the clay surface in two ways: the first, where a physical interaction leads to a spectrum perturbation, and a second, where a chemical interaction leads to ground state surface complexes with CT character. Time-resolved fluorescence studies indicate that thianthrene is adsorbed at various surface sites, resulting in nonexponential fluorescence decay. Photo-irradiation of the CT surface complexes induces electron transfer, leading to radical cations, $TH^{\bullet+}$, which are observed by diffuse reflectance and EPR spectroscopy. Recombination of the electron−ion pairs is observed when samples initially irradiated at low temperatures are warmed. A subsequent photo-irradiation leads to further reaction of $Th^{\bullet+}$. Product analysis confirms that on irradiation into its surface CT band thianthrene is photochemically oxidized, that the mechanism is free radical in nature, and that the important reaction of $Th^{\bullet+}$ on clay surfaces is hydrolysis.

These few studies indicate that the photochemistry of molecules adsorbed on clays is quite similar to that observed on zeolites. Only a few studies are available, and a precise comparison is not possible. The importance of photochemistry on clays to ecology cannot be overemphasized, and more studies on clay systems are needed in the future.

7.7. Summary

The surfaces discussed in this review highlight the important role that surfaces can play in radiation-induced molecular processes. With one "edge" of the work, the surfaces enrich the chemistry of the molecular systems. With the other "edge", a comparison of the chemistry of systems on a surface to that in the well-established area of solution or gas phase chemistry provides new insights of the surfaces themselves. Particular attention is paid to the role

that the surfaces play in ionic reactions of molecules adsorbed on them. Ionic reactions are a minor component of excitation of silica, but are prominent on γ-aluminia, zeolites, and clays. This is consistent with the amorphous nature of SiO_2 and the ionic nature of the other materials. With zeolites, the small internal dimensions play a major role in "size" selection of radiation-induced reactions. γ-Aluminia and zeolites contain various reactive centers (as in thermal catalysis). These introduce the role of CT complexes of guest molecules into radiation-induced chemistry.

8. Symbols

An	anthracene
1-AP	1-aminopyrene
1-APH*	protonated 1-AP
AP^+	alkylpyridinium
BA	Brønsted acid
BP	biphenyl
BD	benzidene
CBP	chlorobiphenyl
CP^+	cetylpyridinium
CT	charge transfer
DABCO	1,4-diazabicyclo[2.2.2]octane
DBK	dibenzyl ketone
DCBP	dichlorobiphenyl
DMA	dimethylaniline
δ_O	partial charge on O_2
$^1\Delta_gO_2$	singlet O_2
e^-	free electrons
e_t^-	trapped electron
E_A	electron affinity
ER	Eley−Rideal mechanism
FcMn	ferrocenylmethyltrimethylammonium cation
FS	Fischer Scientific Co.
$G(x)$	yield of products (molecules) per 100 eV of energy absorbed
h^+	positive hole
h_{trap}^+	trapped h^+
I_D	ionization potential
$\bar{k}$	average (Gaussian) rate constant
LA	Lewis acid
LB	Lewis base
LH	Langmuir−Hinshelwood mechanism
MCB	Matheson Coleman-Bell Co.
Na_n^{n+}	sodium cation clusters
NM	nitromethane
Ox^+	oxonine
PBA	pyrenebutyric acid
PCA	pyrenecarboxylic acid
PCHO	pyrenecarboxaldehyde
PN^+	pyrenylbutyltrimethylammonium cations
PMMA	polymethyl methacrylate
Py	pyrene
$^1Py^*$	singlet excited pyrene
$^3Py^*$	triplet excited pyrene
Py_2^*	excimer of pyrene
$Py_2^{\bullet+}$	pyrene radical cation
$Py^{\bullet-}$	pyrene radical anion
PS	physisorption centers
P^+	pyronine
S_z	Sanderson potential
T_a	activated temperature
$Th^{\bullet+}$	thianthrene radical cation
TMB	tetramethylbenzidine
TMB^+	radical cation of TMB
TMPyP	tetratris(*N*-methyl)pyridyl porphyrin
TNM	tetranitromethane

9. Acknowledgment

I thank R. Patti, D. Bennett, and R. Egendoerfer for typing the manuscript, June Thomas for proofreading, and the University of Notre Dame for much support.

10. References

(1) Fendler, J. H. *Membrane Mimitic Chemistry*; Wiley: New York, 1982.
(2) Grätzel, M. *Energy Sources by Photochemistry and Catalysis*; Academic Press: New York, 1963.
(3) Kalyanasundaram, K. *Photochemistry in Microheterogeneous Systems*; Academic Press: New York, 1987.
(4) Thomas, J. K. *Chemistry of Excitation at Surfaces*; ACS Monograph 181; American Chemical Society: Washington, DC, 1984.
(5) Claesson, S., Engstrom, T., Eds. *Solar Energy—Photochemical Conversion and Storage*; National Swedish Board for Energy Source Development: Sweden, 1977.
(6) Kalyanasundaram, K.; Grätzel, M. In *Chemistry and Physics of Solids*; Varselov, R., Howe, R., Eds.; Springer-Verlag: Berlin, Germany, 1984; p 111.
(7) Kamat, P. V.; Meisel, D. *Semiconductor Nanoclusters-Physical, Chemical and Catalytic Aspects*; Elsevier: Amsterdam, The Netherlands, 1997; p 1562.
(8) Wilkinson, F.; Beer, R.; Honda, K.; Eds. *Photochemical Processes in Organised Media*; Elsevier Science: New York, 1991; p 377.
(9) Zhang, G.; Mao, Y.; Thomas, J. K. *J. Phys. Chem*. **1997**, *101*, 7100.
(10) Thomas, J. K. *J. Phys. Chem*. **1987**, *91*, 267.
(11) Wilkinson, F.; Kessler, R. W. *J. Chem. Soc., Faraday Trans*. **1981**, *77*, 309.
(12) Oelkrug, D.; Honnen, W.; Wilkinson, F.; Willsher, C. J. *J. Chem. Soc., Faraday Trans*. **1987**, *83*, 2081.
(13) Oelkrug, D., Wolfbeis, O. S., Eds. *Fluorescence Spectroscopy, New Methods and Applications*; Springer-Verlag: Heidelberg, Germany, 1993; p 65.
(14) Brunauer, S.; Emmett, P. H.; Teller, E. *J. Am. Chem. Soc*. **1938**, *60*, 309.
(15) Brunauer, S. *The Adsorption of Gases and Vapors*; Princeton University Press: London, U.K., 1943; Vol. 1, p 140.
(16) Gregg, S. J.; Sing, K. S. W. *Adsorption Surface Area and Porosity*; Academic Press: London, U.K., 1967.
(17) Iler, R. K. *The Chemistry of Silica*; Wiley: New York, 1979.
(18) Thomas, J. K. *Chem. Rev*. **1993**, *93*, 301.
(19) Albery, W. J.; Bartlett, P. N.; Wilde, C. P.; Darwent, J. R. *J. Am. Chem. Soc*. **1985**, *107*, 1854.
(20) Krasnansky, R.; Koike, K.; Thomas, J. K. *J. Phys. Chem*. **1990**, *94*, 4521.
(21) Avnir, D. *J. Am. Chem. Soc*. **1987**, *109*, 2931.
(22) Elias-Kohau, T.; Shein Tuch, M.; Avnir, D. *Chem. Eng. Sci*. **1991**, *46*, 2787.
(23) Klafter, J.; Blumen, A.; Zumofan, G. *J. Lumines*. **1984**, *3*, 627.
(24) Levitz, P.; Drake, J. M.; Klafter, J. *J. Chem. Phys*. **1988**, *9*, 5224.
(25) Breton, G. W.; Dans, K. A.; Kropp, P. J. *J. Org. Chem*. **1992**, *57*, 6646.
(26) Kropp, P. J.; Dans, K. A.; Tubergen, M. W.; Kepler, K. D.; Watson, V. P.; Craig, S. L.; Baillargeon, M.; Breton, G. W. *J. Am. Chem. Soc*. **1993**, *115*, 3071.
(27) Kropp, P. J.; Crawford, S. D. *J. Org. Chem*. **1994**, *59*, 3102.
(28) Kropp, P. J.; Breton, G. W.; Craig, S. L.; Crawford, S. D.; Dorland, W. F.; Jones, J. E.; Raleigh, J. S. *J. Org. Chem*. **1995**, *60*, 4146.
(29) Foti, C. J.; Fields, J. D.; Kropp, P. J. *Org. Lett*. **1999**, *1*, 903.
(30) Kropp, P. J.; Breton, G. W.; Fields, J. D.; Tring, J. C.; Loomis, B. R. *J. Am. Chem. Soc*. **2000**, *122*, 4280.
(31) Fields, J. D.; Kropp, P. J.; *J. Org. Chem*. **2000**, *65*, 5937.
(32) Nicholls, C. H.; Leermakers, P. A. *Adv. Photochem*. **1971**, *8*, 315.
(33) Krasnansky, R.; Thomas, J. K. *J. Photochem. Photobiol. A: Chem*. **1991**, *57*, 81.
(34) Cehelnik, E. D.; Cundall, R. B.; Lockwood, J. R.; Palmer, T. F. *Chem. Phys. Lett*. **1974**, *27*, 568.
(35) Kalyanasundaram, K.; Thomas, J. K. *J. Am. Chem. Soc*. **1977**, *99*, 2039.
(36) Krasnansky, R. Ph.D. Thesis, University of Notre Dame, 1990.
(37) Bauer, R. K.; deMayo, P.; Ware, W. R.; Wu, K. C. *J. Phys. Chem*. **1982**, *86*, 3781.
(38) Bauer, R. K.; deMayo, P.; Ware, W. R.; Wu, K. C. *J. Am. Chem. Soc*. **1982**, *104*, 4635.
(39) Bauer, R. K.; deMayo, P.; Ware, W. R.; Wu, K. C. *J. Phys. Chem*. **1983**, *87*, 460.
(40) Lochmuller, G. H.; Kersey, M. T.; Hunnicutt, M. L. *Anal. Chim. Acta* **1985**, *125*, 267.
(41) Hite, P.; Krasnansky, R.; Thomas, J. K. *J. Phys. Chem*. **1986**, *90*, 5795.

(42) Krasnansky, R.; Thomas, J. K. *Langmuir* **1994**, *10*, 4551.
(43) Milosavljevic, B. H.; Thomas, J. K. *J. Phys. Chem*. **1988**, *92*, 2997.
(44) Young, G. T. *J. Colloid Sci*. **1958**, *13*, 67.
(45) Anderson, J. H.; Lambard, J.; Hair, M. L. *Colloid Interface Sci*. **1975**, *50* (3), 519.
(46) de Mayo, P. *Pure Appl. Chem*. **1982**, *54* (9), 1623.
(47) Iler, R. K. *The Chemistry of Silica*; Wiley: New York, 1979; pp 209−211.
(48) Sindorf, D. W.; Maciel, G. E. *J. Am. Chem. Soc*. **1983**, *105*, 1487.
(49) Krasnansky, R.; Thomas, J. K. In *The Colloidal Chemistry of Silica*; Bergna, M. E., Ed.; ACS Symposium Series 234; American Chemical Society: Washington, DC, 1994; p 223.
(50) Francis, C.; Lin, J.; Singer, L. A. *Chem. Phys. Letts*. **1963**, *94*, 162.
(51) Marro, M. A. T.; Thomas, J. K. *J. Photochem. Photobiol. A: Chem*. **1993**, *22*, 251.
(52) Liu, Y. S.; Ware, W. R. *J. Phys. Chem*. **1993**, *27*, 5950.
(53) Liu, Y. S.; de Mayo, P.; Wac, W. R. *J. Photochem*. **1993**, *97*, 5995.
(54) Bauer, R. K.; deMayo, P.; Natarajan, L. V.; Ware, W. R. *Can. J. Chem*. **1984**, *62*, 1229.
(55) Ruetten, S. A.; Thomas, J. K. *J. Phys. Chem. B* **1998**, *102*, 598.
(56) Ruetten, S. A. *J. Phys. Chem. B* **1999**, *103*, 1278.
(57) Bennett, R. G.; McCartin, P. J. *J. Chem. Phys*. **1966**, *44*, 1969.
(58) Stevens, B.; Thomaz, M. F.; Jones, J. *J. Chem. Phys*. **1967**, *46*, 405.
(59) Bensasson, R.; Land, E. J. *Trans. Faraday Soc*. **1971**, *67*, 1904.
(60) Koichi, K. *Triplet−Triplet Absorption Spectra: Joem Handbook 1*; Bunshin Publishing: Tokyo, Japan, 1989.
(61) Carmichael, I.; Hug, G. L. *J. Phys. Chem. Ref. Data* **1984**, *15*, 15.
(62) Horrocks, A. R.; Kearvell, A.; Tickle, K.; Wilkinson, F. *Trans. Faraday Soc*. **1966**, *62*, 3393.
(63) Horrocks, A. R.; Wilkinson, F. *Proc. R. Soc. London* **1968**, *A306*, 257.
(64) Richards, J. T.; West, G.; Thomas, J. K. *J. Phys. Chem*. **1970**, *74*, 4137.
(65) Chihara, K.; Baba, H. *Chem. Phys*. **1977**, *25*, 299.
(66) Chihara, K.; Baba, H. *Bull. Chem. Soc. Jpn*. **1925**, *48*, 3903.
(67) Brown, R. G.; Phillips, D. *Chem. Phys*. **1973**, 630.
(68) Drake, J. M.; Levitz, P.; Turro, N. J.; Nitsche, K. S.; Cassidy, J. F. *J. Phys. Chem*. **1988**, *92*, 4680.
(69) Levin, P. P.; Costa, S. M. B.; Vierra-Ferreira, L. F.; Lopez, J. M.; Ribeiro, F. R. *J. Phys. Chem. B* **1997**, *101*, 1355.
(70) Iu, K.; Thomas, J. K. *J. Am. Chem. Soc*. **1990**, *112*, 3319.
(71) Iu, K.; Thomas, J. K. *J. Photochem. Photobiol. A: Chem*. **1993**, *71*, 55.
(72) Bauer, R. K.; Borenstein, R.; de Mayo, P.; Okada, K., Rafalska, M.; Ware, W. R.; Wu, K. C. *J. Am. Chem. Soc*. **1982**, *104*, 4635.
(73) Bjarreson, D. W.; Peterson, N. O. *J. Am. Chem. Soc*. **1990**, *112*, 988.
(74) *J. Phys. Chem*. **1989**, *93*, 4551.
(75) de Mayo, P.; Natarajan, L. V.; Ware, W. R. *J. Phys. Chem*. **1985**, *89*, 3526.
(76) Turro, N. J.; Zimmt, M. B.; Gould, I. R. *J. Am. Chem. Soc*. **1985**, *107*, 5826.
(77) Kajania, S.; Azarani, A.; Johnston, L. J. *J. Phys. Chem*. **1991**, *95*, 4430.
(78) Ruetten, S. A.; Thomas, J. K. *J. Phys. Chem. B* **1999**, *10*, 9285.
(79) Ruetten, S. A.; Thomas, J. K. *Langmuir* **2000**, *16*, 234.
(80) Zhang, G.; Thomas, J. K.; Eremenko, A.; Kikteva, T.; Wilkinson, F. *J. Phys. Chem. B* **1997**, *101*, 8569.
(81) Worrall, D.; Williams, S. L.; Wilkinson, F. *J. Phys. Chem*. **1997**, *101*, 4709.
(82) Oelkrug, D.; Reich, S.; Leicester, P. A.; Wilkinson, F. *J. Phys. Chem*. **1991**, *95*, 269.
(83) Mao, Y.; Thomas, J. K. *J. Phys. Chem*. **1995**, *99*, 2048.
(84) Mao, Y.; Thomas, J. K. *Chem. Phys. Lett*. **1994**, *226*, 127.
(85) Beck, G.; Thomas, J. K. *Chem. Phys. Lett*. **1983**, *94*, 553.
(86) Johnson, L. J. *Photochemistry in Organised and Constrained Media*; VCH: New York, 1991; p 359.
(87) Mao, Y.; Thomas, J. K. *Langmuir* **1992**, *8*, 2501.
(88) Biesinger, R. J.; Montgomery, C. G. *Phys. Rev*. **1970**, *B2*, 4988.
(89) Gillis, H. A.; Klassen, N. V.; Teather, G. G.; Lokan, K. H. *Chem. Phys. Letts*. **1971**, *10*, 481.
(90) Forster, T.; Kaper, K. Z. *Phys. Chem*. **1954**, *1*, 275.
(91) Oelkrug, D.; Radjaipour, M.; Erbse, J. *Z. Phys. Chem*. **1974**, *88*, 23.
(92) Berlman, I. B. *Handbook of Fluorescence Spectra of Aromatic Molecules*; Academic Press: New York, 1971.
(93) Vigouroux, J. P.; Durand, J. P.; LeMoel, A.; LeGressus, C.; Griscom, D. L. *J. Appl. Phys*. **1985**, *57*, 5139.
(94) Thomas, J. K. *Int. J. Photoenergy* **2002**, *4*, 27.
(95) Meisel, D. In *Nanoscale Materials*; Liz-Marzow, L., Kamat, P., Eds.; Kluwer: Dordrecht, The Netherlands, 2003; p 119.
(96) Schatz, T.; Cook, A. R.; Meisel, D. *J. Phys. Chem. B* **1998**, *102*, 7225.
(97) Dimitrijevic, N. M.; Henglein, A.; Meisel, D. *J. Phys. Chem. B* **1999**, *103*, 7073.
(98) Wheeler, J.; Thomas, J. K. *J. Phys. Chem*. **1982**, *86*, 4540.
(99) Prasad, D. R.; Hoffman, M. Z. *J. Phys. Chem*. **1984**, *88*, 5660.
(100) Stramel, R. D.; Thomas, J. K. *J. Chem. Soc., Faraday Trans*. **1986**, *82*(2), 799.
(101) Kuczynski, J. P.; Milosavljevic, B. H.; Lappin, A. G.; Thomas, J. K. *Chem. Phys. Lett*. **1984**, *104*, 149.
(102) Mao, Y.; Breen, N. E.; Thomas, J. K. *J. Phys. Chem*. **1995**, *99*, 9909.
(103) Xiang, B.; Kevan, L. *J. Phys. Chem*. **1994**, *98*, 5120.
(104) Ebbsen, T. W.; Ferraudi, G. *J. Phys. Chem*. **1983**, *87*, 3713.
(105) Milosavljevic, B. H.; Thomas, J. K. *Radiat. Phys. Chem*. **1984**, *23*, 237.
(106) Mao, Y.; Thomas, J. K. *Chem. Phys. Lett*. **1994**, *226*, 127.
(107) Freeman, D. L.; Doll, J. D. *J. Chem. Phys*. **1983**, *78*, 6002.
(108) Samuel, J.; OttHolenghi, M.; Avnir, D. *J. Phys. Chem*. **1992**, *26*, 6398.
(109) Kavanagh, R.; Thomas, J. K. *Langmuir* **1998**, *14*, 352.
(110) Shafer, M. W.; Awschaalom, D. D.; Warnok, J. *J. Appl. Phys*. **1987**, *61*, 5439.
(111) Koicke, K.; Thomas, J. K. *J. Chem. Soc., Faraday Trans. 1* **1992**, *88*, 195.
(112) Harris, J. M. Personal communication.
(113) Ren, F. Y.; Harris, J. M. *Anal. Chem*. **1996**, *68*, 1651.
(114) Waite, S. W.; Marshall, D. B.; Harris, J. M. *Anal. Chem*. **1994**, *66*, 2052.
(115) Ren, F. Y.; Waite, S. W.; Harris, J. M. *Anal. Chem*. **1995**, *67*, 3441.
(116) Kavanagh, R.; Thomas, J. K. *Phys. Chem. Chem. Phys*. **2002**, *4*, 193.
(117) Levitz, P.; Van Damme, H. *J. Phys. Chem*. **1986**, *90*, 1302.
(118) Levitz, P.; Van Damme, H.; Keravis, D. *J. Phys. Chem*. **1984**, *88*, 2228.
(119) Stange, T. G.; Mathew, R.; Evans, D. F.; Hendrickson, W. A. *Langmuir* **1992**, *8*, 920.
(120) Ellison, E. H.; Thomas, J. K. *Langmuir* **1996**, *12*, 1870.
(121) Ellison, E. H.; Thomas, J. K. In *Multidimensional Spectroscopy of Polymers*; Urban, M. W., Provder, T., Eds.; ACS Symposium Series 598; American Chemical Society: Washington, DC, 1994; Chapter 24, p 410.
(122) Turro, N. J. *Tetrahedron* **1987**, *43*, 1589.
(123) de Mayo, P.; Johnson, L. J. In *Preparative Chemistry using Supported Reagents*; Taszolo, P., Ed.; Academic Press: San Diego, CA, 1987; Chapter 4.
(124) Turro, N. J.; Baretz, B. H. *J. Am. Chem. Soc*. **1983**, *105*, 1310.
(125) Frederick, B.; Johnson, L. J.; de Mayo, P.; Wong, S. K. *Can. J. Chem*. **1984**, *62*, 403.
(126) Johnson, L. J. In *Photochemistry in Organised Media*; Ramamurthy, V. Ed.; VCH Press: New York, 1991; p 364.
(127) Kamat, P. V. *Chem. Rev*. **1993**, *93*, 267. Moss, J.; Grätzel, M. *J. Am. Chem. Soc*. **1984**, *106*, 4336. Rothenberger, G.; Moser, J.; Grätzel, M.; Serpone, N.; Sharma, D. K. *J. Am. Chem. Soc*. **1985**, *107*, 8054. Hoffmann, M. R.; Marim, S. T.; Choi, W.; Bahnermann, D. W. *Chem. Rev*. **1995**, *95*, 76.
(128) Anderson, C.; Bard, A. J. *J. Phys. Chem*. **1989**, *93*, 7544.
(129) Ruetten, S. A.; Thomas, J. K. *Photochem. Photobiol. Sci*. **2003**, *2*, 1018.
(130) Anpo, M.; Aikawa, N.; Kubokawa, Y.; Che, M.; Louis, C.; Giamelco, E. *J. Phys. Chem*. **1985**, *89*, 5017.
(131) Misra, C. *Industrial Alumina Chemicals*; ACS Monograph 184; American Chemical Society: Washington, DC, 1996. Wells, A. F. *Structural Inorganic Chemistry*, 5th ed.; Clarendon Press: Oxford, U.K., 1984.
(132) Anderson, J. H.; Lombardi, J.; Hair, M. L. *Colloid Interface Sci. (Proc. Int. Conf.)* **1975**, *50*, 519.
(133) Pohle, W. *J. Chem. Soc., Faraday Trans. 1* **1982**, *78*, 2101.
(134) Peri, J. B.; Hannan, R. B. *J. Phys. Chem*. **1960**, *64*, 1526.
(135) Knözinger, H.; Ratnasamy, P. *Catal. Rev.−Sci. Eng*. **1981**, *17*, 31.
(136) Waiter, I. H.; Oldfield, E. *J. Phys. Chem*. **1989**, *93*, 6144.
(137) Pankasem, S.; Thomas, J. K. *Langmuir* **1992**, *8*, 501.
(138) Rampfer, K.; Uhl, S.; Oelkrug, D. J. *Mol. Struct*. **1984**, *114*, 225.
(139) Oelkrug, D. J.; Radjaipour, M.; Erbse, H. *Z. Phys. Chem*. **1974**, *88*, 23.
(140) Honen, W.; Krabichler, G.; Uhl, S.; Oelkrug, D. *J. Phys. Chem*. **1983**, *87*, 4872.
(141) Uhl, S.; Krabichler, G.; Rampfer, K.; Oelkrug, D. *J. Mol. Struct*. **1986**, *143*, 279.
(142) Oelkrug, D.; Radjaipour, M. *Z. Phys. Chem*. **1980**, *123*, 163.
(143) Pankasem, S.; Thomas, J. K. *J. Phys. Chem*. **1991**, *95*, 6990.
(144) Pankasem, S.; Thomas, J. K. *J. Phys. Chem*. **1991**, *95*, 7385.
(145) Beck, G.; Thomas, J. K. *Chem. Phys. Lett*. **1983**, *94*, 553.
(146) Milosavljevic, B. H.; Thomas, J. K. *J. Phys. Chem. B* **2003**, *107*, 11907.
(147) Miller, A. *The Exciplex*; Academic Press: New York, 1975; p 23.
(148) Shida, T.; Iwata, S. *J. Am. Chem. Soc*. **1973**, *95*, 3473.
(149) Kalyanasundaram, K.; Thomas, J. K. *J. Phys. Chem*. **1977**, *81*, 2176.
(150) Bredereck, K.; Förster, Th.; Oesterlin, H.-G. *Luminescence of Organic and Inorganic Materials*; Kallmann, H. P., Spruch, G.

M., Eds.; International Conference; New York University: New York, 1962; p 161.
(151) Baretz, B. H.; Turro, N. J. *J. Photochem*. **1984**, *24*, 201.
(152) Rooney, J. J.; Pink, R. C. *Trans. Faraday Soc*. **1962**, *58*, 1632.
(153) Hall, W. K. *J. Catal*. **1962**, *1*, 53.
(154) Kortum, G.; Schickenmaier, V. *Z. Phys. Chem*. **1966**, *48*, 267.
(155) Chandrasekaran, K.; Thomas, J. K. *J. Am. Chem. Soc*. **1983**, *105*, 6309.
(156) Ware, W. R.; Cunningham, P. T. *J. Chem. Phys*. **1965**, *43*, 3826.
(157) Asmolor, E. J.; Kaylou, O. V. *Kinet. Katal.* **1978**, *19*, 979.
(158) Choi, H. T.; Haglund, J. A.; Lipsky, S. *J. Phys. Chem*. **1983**, *87*, 1583.
(159) Mozumder, A. *Fundamentals of Radiation Chemistry*; Academic Press: New York, 1999.
(160) Zhang, G.; Thomas, J. K. *J. Phys. Chem*. **1994**, *98*, 11714.
(161) Milosavljevic, B. H.; Thomas, J. K. *Radiat. Phys. Chem*. **2001**, *62*, 3.
(162) Tanimura, K.; Tanaka, T.; Itoh, N. *Phys. Rev. Lett.* **1983**, *51*, 423.
(163) Tanimura K.; Itoh, C.; Itoh, N. *J. Phys. C* **1988**, *21*, 1869.
(164) Itoh, C.; Tanimura K.; Itoh, N. *J. Phys. C* **1988**, *21*, 4693.
(165) Itoh, C.; Suzuki, T.; Itoh, N. *Phys. Rev. B* **1990**, *41*, 3794.
(166) Saeta, P. N.; Greene, B. I. *Phys. Rev. Lett*. **1993**, *70*, 3588.
(167) Audebert, P.; Daguzan, P.; Dos Santos, A.; Gauthier, J. C.; Geindre, J. P.; Guizard, S.; Hamoniaus, G.; Krastev, K.; Martin, P.; Petite, G.; Antonett, A. *Phys. Rev. Lett*. **1994**, *73*, 1990.
(168) Mao, Y.; Thomas, J. K, *Langmuir* **1994**, *10*, 709.
(169) Mao, Y.; Thomas J. K. *J. Chem. Soc., Faraday Trans*. **1992**, *58*, 3079.
(170) Dorfman, L. M.; Taub, I. A. *J. Chem. Phys*. **1962**, *36*, 305.
(171) Sehested, K.; Hart, E. *J. Phys. Chem*. **1975**, *79*, 1639.
(172) Barber, D. J.; Thomas, J. K. *Radiat. Res*. **1978**, *74*, 51.
(173) Steenken, S. *J. Chem. Soc., Faraday Trans. 1* **1987**, *83*, 113.
(174) Ristagno, C. V.; Shine, H. J. *J. Org. Chem*. **1971**, *36*, 4050.
(175) Sioda, R. E. *J. Phys. Chem*. **1968**, *72*, 2322.
(176) Kanodia, S.; Madhaven, V.; Schuler, R. H. *Radiat. Phys. Chem*. **1988**, *32* (5), 661.
(177) Ruzo, L. O.; Zabik, M.; Schuetz, R. D. *J. Am. Chem. Soc*. **1974**, *96*, 3809.
(178) Ruzo, L. O.; Safe, S.; Zabik, M. J. *J. Agric. Food Chem*. **1975**, *23*, 594.
(179) Bunce, N. J.; Kumar, Y.; Ravanal, L.; Safe, S. *J. Chem. Soc., Perkin Trans. 2* **1978**, 880.
(180) Olashi, M.; Tsujimoto, K.; Seki, K. *J. Chem. Soc., Chem. Commun*. **1973**, 384.
(181) Nordblom, G. D.; Miller, L. L. *J. Agric. Food. Chem*. **1974**, *22*, 57.
(182) Egger, K. W.; Cocks, A. T. *Helv. Chim. Acta* **1975**, *56*, 1516.
(183) Davidson, R. S.; Goodwin, J. W.; Kemp, G. *Adv. Phys. Org. Chem*. **1994**, *20*, 191.
(184) Zacheis, G. A.; Gray, K. A.; Kamat, P. *J. Phys. Chem*. **1999**, *103*, 2142.
(185) Zacheis, G. A.; Gray, K. A.; Kamat, P. *J. Phys. Chem*. **2001**, *105*, 4715.
(186) Beck, D. W. *Zeolite Molecular Sieves, Structure, Chemistry and Use*; Wiley: New York, 1974.
(187) Barrer, R. M. *Zeolites and Clay Minerals as Solvents and Molecular Seives*; Academic Press: London, U.K., 1978.
(188) *Atlas of Zeolite Framework Types*, 5th ed.; Elsevier: Amsterdam, The Netherlands, 2001.
(189) Robson, H.; Lillered, K. P. *Verified Synthesis of Zeolite Materials*; Elsevier: Amsterdam, The Netherlands, 2001.
(190) Cundy, C. S.; Cox, P. A. *Chem. Rev*. **2003**, *103*, 663.
(191) Garcia, H.; Roth, H. D. *Chem. Rev*. **2002**, *102*, 3947.
(192) Hashimoto, S. *J. Photochem. Photobiol. C* **2003**, *4*, 19.
(193) Sanderson, R. T. *Chemical Bonds and Bond Energy*, 2nd ed.; Academic Press: New York, 1976.
(194) Thomas, J. K. *The Chemistry of Excitation at Interfaces*; ACS Monograph 189; American Chemical Society: Washington, DC, 1984.
(195) Liu, X.; Thomas, J. K. *Langmuir* **1993**, *9*, 727.
(196) Iu, K.-K.; Thomas, J. K. *Langmuir* **1990**, *6*, 471.
(197) Liu, X.; Thomas, J. K. *Chem. Mater*. **1994**, *6*, 2303.
(198) Liu, X.; Iu, K.-K.; Thomas, J. K. *J. Phys. Chem*. **1994**, *98*, 7877.
(199) Ellison, E. *J. Phys. Chem*. **1999**, *103*, 9314.
(200) Liu, X.; Mao, Y.; Ruetten, S. A.; Thomas, J. K. *Sol Energy Mater. Sol. Cells* **1995**, *38*, 199.
(201) Kavanagh, R.; Iu, K.-K.; Thomas, J. K. *Langmuir* **1992**, *8*, 3008.
(202) Hashimoto, S. *Chem. Phys. Lett*. **1996**, *252*, 236.
(203) Hashimoto, S.; Kirkae, S.; Tobita, S. *Phys. Chem. Chem. Phys*. **2002**, *4*, 5856.
(204) Hashimoto, S.; Hagin, M.; Barzykin, A. V. *J. Phys. Chem. B* **2002**, *106*, 1844.
(205) Barzykin, A. V.; Hashimoto, S. *J. Chem. Phys*. **2000**, *113*, 2841.
(206) Hashimoto, S.; Miyashita, T.; Hagiri, M. *J. Phys. Chem. B* **1999**, *103*, 9149.
(207) Gedeon, I.; Fraissand, J. *Zeolites* **1988**, *8*, 376.
(208) Johnson, L. J.; Scaiano, J. C.; Shi, J.-L.; Siebrand, W.; Zerbetto, F. *J. Phys. Chem*. **1991**, *95*, 10018.
(209) Cozens, F.; Oritz, W.; Schepp, N. P. *J. Am. Chem. Soc*. **1998**, *120*, 13543.
(210) Ramamurthy, V.; Caspar, J. V.; Corbin, D. R.; Eaton, D. F.; Kaufmann, J. S.; Dybowski, C. J. *J. Photochem. Photobiol. A Chem*. **1990**, *51*, 259.
(211) Ellison, E. H.; Thomas J. K. *J. Phys. Chem. B* **2001**, *105*, 2757.
(212) Hashimoto, S.; Ikuta, S.; Ashai, T.; Masuhara, H. *Langmuir* **1998**, *14*, 4284.
(213) Ramamurthy, V.; Caspar, J. V.; Corbin, D. R. *J. Phys. Chem*. **1990**, *94*, 3391.
(214) Ramamurthy, V. *Photochemistry in Organised and Constrained Media*; Ramamurthy, V., Ed.; VCH Publishers: New York, 1991.
(215) Liu, X.; Iu, K.-K.; Thomas, J. K. *J. Phys. Chem*. **1989**, *93*, 4120.
(216) Thomas, J. K. Unpublished data.
(217) Zhang, G.; Thomas, J. K. *J. Phys. Chem. B* **2003**, *107*, 7254.
(218) Ellison, E. H.; Thomas, J. K. *Micropor. Mesopor. Mater*. **2001**, *49*, 15.
(219) Scaiano, J. C.; deLucas, N.; Andraos, J.; Garcia, H. *Chem. Phys. Lett*. **1995**, *223*, 5.
(220) Ellison, E. H.; Thomas, J. K. *Langmuir* **2001**, *17*, 2446.
(221) O'Neill, M. A.; Cozens, F. L.; Schepp, N. P. *J. Phys. Chem. B* **2001**, *105*, 12746.
(222) Kasai, P. H. *J. Chem. Phys*. **1965**, *43*, 3223.
(223) Kasai, P. H.; Bishop, R. J. *J. Phys. Chem*. **1973**, *77*, 2308.
(224) Barrer, R. M.; Cole, J. F. *J. Phys. Chem. Solids* **1968**, *23*, 1755.
(225) Edwards, P. P.; Harrison, M. R.; Klinowski, J.; Ramolas, S.; Thomas, J. M.; Johnson, D. C.; Page, C. *J. Chem. Soc., Chem. Commun*. **1984**, 982.
(226) (a) Liu, X.; Iu, K.-K.; Thomas, J. K.; He, H.; Klinowski, J. *J. Am. Chem. Soc*. **1994**, *116*, 11811. (b) Liu, X.; Thomas, J. K. *Langmuir* **1992**, *8*, 1750.
(227) Liu, X.; Iu, K.-K.; Thomas, J. K. *J. Phys. Chem*. **1994**, *98*, 13720.
(228) Liu, X.; Thomas, J. K. *J. Chem. Soc., Faraday Trans*. **1995**, *91*, 759.
(229) Liu, X.; Zhang, G.; Thomas, J. K. *J. Phys. Chem*. **1995**, *99*, 10024.
(230) Liu, X.; Zhang, G.; Thomas, J. K. *J. Phys. Chem. B* **1997**, *101*, 2182.
(231) Zhang, G.; Liu, X.; Thomas, J. K. *Radiat. Phys. Chem*. **1998**, *51*, 135.
(232) Houg, K.; Irdanov, V. I.; Stucky, G.; Metiu, H. *J. Chem. Phys.* **1992**, *96*, 3495.
(233) Blake, N. P.; Metiu, H. *J. Chem. Phys*. **1994**, *101*, 223.
(234) Blake, N. P.; Irdanov, V. I.; Stucky, G. D.; Metiu, H. *J. Phys. Chem*. **1995**, *99*, 2127.
(235) Iu, K.-K.; Thomas, J. K. *J. Phys. Chem*. **1991**, *95*, 506.
(236) Iu, K.-K.; Liu, X.; Thomas, J. K. *J. Phys. Chem*. **1993**, *97*, 8165.
(237) Iu, K.-K.; Liu, X.; Thomas, J. K. *J. Photochem. Photobiol*. **1994**, *79*, 103.
(238) Lednev, J. K.; Mathivanan, N.; Johnston, L. J. *J. Phys. Chem*. **1994**, *98*, 11444.
(239) Camagnola, P. J.; Levrich, D. J.; DiLuca, M. J.; Johnson, M. A. *J. Chem. Phys*. **1991**, *94*, 5240.
(240) Loc, J. V.; Lee, G. H.; Eaton, J. G.; Arnold, S. T.; Sarkas, H. W.; Bowen, K. H.; Ludewegt, C.; Haberland, H.; Worsnop, D. R. *J. Chem. Phys*. **1990**, *92*, 3980.
(241) Thomas, J. K. *Int. J. Photoenergy* **2002**, *4*, 27.
(242) Glassner, F.; Scaiano, J. C. *J. Photochem. Photobiol. A. Chem.* **1992**, *67*, 91.
(243) Iu, K.-K.; Thomas, J. K. *Colloids Surfaces* **1992**, *63*, 39.
(244) Werst, D. W.; Han, P.; Trifunac, A. D. *Radiat. Phys. Chem*. **1998**, *51*, 255.
(245) Liu, X.; Iu, K.-K.; Thomas, J. K. *Chem. Phys. Lett*. **1993**, *204*, 163.
(246) Alvaro, M.; Garcia, H.; Garcia, S.; Marquez, F.; Scaiano, J. C. *J. Phys. Chem. B* **1997**, *101*, 3043.
(247) Yoon, K. B. *Chem. Rev*. **1993**, *93*, 321.
(248) Yoon, K. B.; Hubig, S. M.; Kochi, J. K. *J. Phys. Chem*. **1994**, *98*, 3865.
(249) Dutta, P. K.; Incavo, J. A. *J. Phys. Chem*. **1987**, *91*, 4443. Dutta, P. K.; Incavo, J. A. *J. Phys. Chem*. **1990**, *94*, 3075.
(250) Lainé, P.; Lanz, M.; Calzaferri, G. *Inorg. Chem*. **1996**, *35*, 3514.
(251) Turro, N.; Cheng, C. C.; Abrams, L.; Corbin, D. R. *J. Am. Chem. Soc*. **1987**, *109*, 2449.
(252) Turro, N.; Lui, X.; Li, W.; McDermott, A.; Abrams, L.; Ottawiani, M. F.; Beard, H. S. *Chem. Commun*. **1998**, 695. Turro, N.; Lui, X.; Li, W.; McDermott, A.; Abrams, L.; Ottawiani, M. F.; Beard, H. S. *Chem. Commun*. **1998**, 697.
(253) Hirano, T.; Li, W.; Abrams, L.; Krusic, P.; Ottaviani, M. F.; Turro, N. *J. Am. Chem. Soc*. **1999**, *121*, 7170.
(254) Jochusch, S.; Hirano, T.; Liu, Z.; Turro, N. *J. Phys. Chem. B* **2000**, *104*, 1212.
(255) Turro, N. *Pure Appl. Chem*. **1986**, *58*, 1219.
(256) Turro, N.; Buchachenko, A. L.; Tarasov, V. F. *Acc. Chem. Res*. **1995**, *28*, 69.
(257) Turro, N. *Acc. Chem. Res*. **2000**, *33*, 637.
(258) Turro, N. *Modem Molecular Photochemistry*; Benjamin: Menlo Park, CA, 1978.
(259) Nishiguchi, H.; Okamoto, S.; Nishimura, H.; Yamashita, H.; Anpo, M. *Res. Chem. Intermed*. **1998**, *24*, 849.

(260) Shailaja, J.; Lakshimarasimhan, P. H.; Pradhan, A. R.; Sunoj, R. B.; Jockusch, S.; Karthikeyan, S.; Uppili, S.; Chandrasekhar, J.; Turro, N. J.; Ramamurthy, V. *J. Phys. Chem. A* **2003**, *107*, 3187.
(261) Corrent, S.; Martinez, L. J.; Scaiano, J.; Garcia, H.; Fornes, V. J. *J. Phys. Chem*. **1999**, *103*, 8097.
(262) Cizmeceyan, D.; Sonrichsen, L. R.; Garcia-Garibay, M. A. *J. Am. Chem. Soc*. **1997**, *119*, 184.
(263) Frederick, B.; Johnston, L. J.; deMayo, P.; Wong, S. K. *Can. J. Chem*. **1984**, *62*, 403.
(264) Scaiano, J. C.; Garcia, H. *Acc. Chem. Res*. **1999**, *32*, 783.
(265) Thomas, J. K. *Photochem. Photobiol. Sci*. **2004**, *3*, 483.
(266) Blatter, F.; Frei, H. *J. Am. Chem. Soc*. **1993**, *115*, 7501.
(267) Blatter, F.; Frei, H. *J. Am. Chem. Soc*. **1994**, *116*, 1812.
(268) Blatter, F.; Moreau, F.; Frei, H. *J. Phys. Chem*. **1994**, *98*, 13404.
(269) Vasenkov, S.; Frei, H. *J. Phys. Chem. B* **1997**, *101*, 4539.
(270) Sun, H.; Blatter, F.; Frei, H. *J. Am. Chem. Soc*. **1994**, *116*, 7951.
(271) Sun, H.; Blatter, F.; Frei, H. *J. Am. Chem. Soc*. **1996**, *118*, 6873.
(272) Blatter, F.; Sun, H.; Frei, H. *Angew. Chem., Int. Ed*. **1996**, 35.
(273) Sun, H.; Frei, H. *J. Phys. Chem. B* **1997**, *101*, 205.
(274) Sivaguru, J.; Nararajan, A.; Kaaumaue, L. S.; Uppili, S. S.; Joy, A.; Ramamurthy, V. *Acc. Chem. Res*. **2003**, *36*, 509.
(275) Calzaferri, G.; Maas, H.; Pauchard, M.; Pfenniger, M.; Migelski, S.; Devaux, A. *Adv. Photochem*. **2002**, *27*, 1.
(276) Yatskou, M.; Meyer, M.; Huber, S.; Pfenniger, M.; Calzaferri, G. *Chem. Phys*. **2003**, *4*, 567.
(277) Calzaferri, G.; Huber, S.; Maas, H.; Minkowski, C. *Angew. Chem., Int. Ed.* **2003**, *42*, 3732.
(278) Ozin, G. A.; Hugues, F.; Mattar, S. M. *J. Phys. Chem*. **1985**, *89*, 300.
(279) Strome, D. H.; Klier, K. *Adsorption and Ion Exchange with Synthetic Zeolites*; Flash, W. H., Ed.; ACS Symposium Series 185; American Chemical Society: Washington, DC, 1980; p 155.
(280) Suib, S. L.; Carrado, K. A. *Inorg. Chem*. **1985**, *24*, 200.
(281) Azenha, M. E. D. G.; Miguel, M. da G.; Formosinho, S. J.; Burrows, H. D. *J. Mol. Struct.* **2001**, *564*, 439.
(282) Yang, C. L.; El Sayed, M. A.; Suib, S. L. *J. Phys. Chem*. **1987**, *91*, 4440.
(283) Suib, S. L. *Photochem. Photophys*. **1990**, *3*, 1.
(284) Baker, M. D.; Olken, M. M.; Ozin, G. A. *J. Am. Chem. Soc*. **1988**, *110*, 5709.
(285) Leiggener, C.; Brühwiler, D.; Calzaferri, G. *J. Mater. Chem*. **2003**, *13*, 1969.
(286) Seifert, R.; Rytz, R.; Calzaferri, G. *J. Phys. Chem. A* **2000**, *104*, 7473.
(287) Calzaferri, G.; Leiggener, C.; Glaus, S.; Schürch. D.; Kuge, K. *Chem. Soc. Rev*. **2003**, *32*, 29.
(288) Calzaferri, G.; Hug, S.; Hugentobler, T.; Sulzberger, B. *J. Photochem*. **1984**, *26*, 109.
(289) Leutwyler, S.; Schumaker, E. *Chimia* **1977**, *31*, 475.
(290) Chandrasekaran, K.; Thomas, J. K. *Chem. Phys. Lett*. **1983**, *97*, 357.
(291) Schürch, D.; Currao, A.; Sarkar, S.; Hodes, G.; Calzaferri, G. *J. Phys. Chem. B* **2002**, *106*, 12764.
(292) Van Olphen, H. *An Introduction to Clay Colloid Chemistry*, 2nd ed.; Wiley: New York, 1963.
(293) Dellaguardia, R.; Thomas, J. K. *J. Phys. Chem*. **1983**, *87*, 990.
(294) Dellaguardia, R.; Thomas, J. K. *J. Phys. Chem*. **1983**, *87*, 3550.
(295) Dellaguardia, R.; Thomas, J. K. *J. Phys. Chem*. **1983**, *88*, 964.
(296) Kuykendall, V. G.; Thomas, J. K. *J. Phys. Chem*. **1990**, *94*, 4224.
(297) Kovar, L.; Dellaguardia, R.; Thomas, J. K. *J. Phys. Chem*. **1984**, *88*, 3595.
(298) Nakamura, T.; Thomas, J. K. *Langmuir* **1985**, *1*, 568.
(299) Nakamura, T.; Thomas, J. K. *J. Phys. Chem*. **1986**, *90*, 641.
(300) Kuykendall, V. G.; Thomas, J. K. *Langmuir* **1990**, *6*, 1350.
(301) Bottero, J. Y.; Cases, J. M.; Flessenger, F.; Poirer, J. E. *J. Phys. Chem*. **1980**, *84*, 2933.
(302) Liu, X.; Thomas, J. K. *Langmuir* **1991**, *7*, 2808.
(303) Iu, K.-K.; Liu, X.; Thomas, J. K. *Chem. Phys. Lett*. **1991**, *186*, 198.
(304) Liu, X.; Iu, K.-K.; Thomas, J. K. *Langmuir* **1992**, *8*, 539.
(305) Mao, Y.; Zhang, G.; Thomas, J. K. *Langmuir* **1993**, *9*, 1299.
(306) Mao, Y.; Thomas, J. K. *J. Org. Chem*. **1993**, *58*, 6641.

CR020378A